IN-VIVO CHARACTERIZATION OF S-CONE TOPOGRAPHY ACROSS THE HUMAN MACULA

Sierra Ashley Schleufer

A dissertation

submitted in partial fulfillment of

Doctor of Philosophy

University of Washington

Reading Committee:

Ramkumar Sabesan, Chair

Fred Rieke

Table of Contents

Figures

TABLES

EQUATIONS

1: Introduction

1.1 The importance of spectral topography to visual neuroscience

The retina is tiled with millions of photoreceptors that are the input sensory neurons to the visual system. The layer of photoreceptors is followed postreceptorally by a dense neural jungle of interconnected parallel and serial circuits that shape the information about light in the world to be relayed to the brain via the optic nerve. In most people have 4 types of photoreceptor, rods and the 3 cone types called L-, M-, and S-type that are distinguished by their sensitivity to Long, Medium, and Short wavelengths. Cones are concentrated densely in the retina, a primary feature of the foveal region of the central retina that is responsible for the high acuity vision and color vision we enjoy.

Spectral topography, the quantitative description of the spatial distribution of cones in the photoreceptor mosaic, is critical to understanding spatial-spectral limitations at the input-level of visual circuits. Mature topography of the cone types across the retina governs trade-offs between achromatic vision and color vision in photopic conditions. Their arrangement sets fundamental spatial limits to spectral sampling at the level of photoreceptors. The spatial resolution of the visual field at the level of cones is increased by the drift components of fixational eye-movements[1–5], while simultaneously limited by postreceptoral circuitry[6–15]. These features combined with optical properties of the outer eye and retina determine the spectral information that can be decoded across space and time by visual circuits in the brain. While the factors linking cone topography and perception are many, there is no doubt that understanding cellular-scale spatial patterns is a critical bookend to comprehending the system.

Spectral topography has been linked directly to visual performance in a number of studies. Since the advent of methods to classify cones in-vivo (described in the next section), spectral topography has been connected directly to psychophysics.[16–19,19–23] At the non-cellular scale, there has also been considerable work relating L:M ratio measured with ERG to visual performance.[24,25]

The study of spectral topography has also benefited developmental research, though we have not yet been able to see migration of cone types throughout development in individuals. Snapshots of the retina are taken from various developmental stages and the distribution of the cone types in each. These studies paired with those that study spatiotemporal expression of relevant factors influencing cell differentiation, maturation, migration, and pruning provide the basis for our understanding of how mature topography comes to be.

1.2 Studying spectral topography in-vivo

Spectral classification in-vivo is a powerful approach to study spectral topography and its influence on human vision. This non-invasive branch of imaging utilizes adaptive-optics to acquire cellular resolution images of retinal photoreceptors. Adaptive optics was invented by astronomers to overcome temporally variable optical aberrations in the atmosphere that prevented clear visualization [Peebles 1980]. Simply put, adaptive optics is accomplished by a closed loop system with a component that measures optical aberrations continuously (the wavefront sensor) and a component that performs the optical correction (the deformable mirror). The optics of the eye help to focus light onto the retina, but abberrates light reflected from it which precludes clear optical access to cells in the retina. AO can be used to overcome this optical obstacle as well as it can for earth's atmosphere. In the late 90's to present, we have seen such systems leveraged to create clearer views of the retina in-vivo and to even capture functional-signals (optoretinograms, or ORG) from retinal cells to study their physiology.

In retinal physiology, densitometry is the use of light reflected back from the retina to discern functional properties. Images capture reflections with intensity of light corresponding to brightness of pixels. When photoreceptors respond to alight stimulus, photons are absorbed by photopigment in the cells, meaning there is less light to be reflected back. The amount of light incident to a photoreceptor that is absorbed versus reflected is influenced by the variety of photopigment it contains. A long-wavelength light, e.g. 660nm, shown on the retina will be absorbed most by L-cones, less by M-cones, and least by S-cones. This difference in reflectivity was taken advantage to produce the first trichromatically classified images of the human retina In 1999, en-face AO fundus camera based densitometry was used to was used to spectrally class the three cone types for the first time

This technology was an enormous advance to study of the retina and spectral topography. S-cones had been isolated with immunohistochemistry techniques in the decade prior, but L and M cones could not, and still cannot, be differentiated this way because they are so genetically similar.[26,27] To differentiate L and M cones, one must compare their responses to narrow-band light stimuli that one or the other is more sensitive to. So, the initial spectral topography experiments using densitometry were a first view into trichromatic spectral topography. These reports assessed human and macaque spectral topography within about 1-2°eccentricity from the fovea, between 1-2 ROIs in about a dozen individuals.

With the recent advent of AO-OCT, we have demonstrated the ability to image and measure cone activity at higher resolution over larger spans of the [28–31] retina than ever before. Spectral classification

with AO-OCT operates on the same principles as with AO-SLO densitometry; optics of the eye are overcome, and an optical signal is measured as a proxy of cone activity during a light stimulus that the three cone types are differently sensitive to. AO-OCT is fundamentally different in the optical signal it utilizes that has proven to be better suited for cone-classification than densitometry. The AO-OCT system and its myriad benefits to spectral classification are described at length in Chapter 2.

My thesis describes spectral topography in an unprecedentedly rich dataset, thanks to these advances. The Sabesan Lab pioneers optical engineering to push the limits of structural and functional retinal microscopy. Vimal Pandiyan has devoted his post-doctoral work to the creation and use of an AO-OCT system that affords us higher resolution and higher throughput spectral classification than any other lab. In two subjects who were able to be imaged in numerous multi-hour sessions, he performed AO-OCT experiments and spectral classification spanning the ~1-12°radius of the central retina. The dataset contains novel information about how L and M cones are arranged with respect to one another and to S cones as a function of eccentricity and retinal meridian. Furthermore, these subjects are ideal candidates for psychophysical experiments exploring the influence of spectral topography on chromatic and achromatic vision.

This puts us in an incredible position to shed light on how L & M cone topography varies across the retina and among individuals, and how the 3 cone types are arranged with respect to one another. We are also able to perform psychophysical tests of color and spatial vision in the subjects whose cones have been classified, allowing us to answer long-standing questions about the direct relationship between spectral topography and perceptual limits. Thorough characterization of the trichromatic cone mosaic is a critical step toward better understanding the diversity of spectral topography, developmental mechanisms supporting spectral topography, and spectral-spatial limits of cone-mediated vision.

By classifying regions spanning the central retina in-vivo, we have unprecedented ability to examine how the topography of S-cones varies with respect to other features of the retina and eye as well as visual perception. We provide a description of the S-cone topography with respect to foveal eccentricity, S-cone proportion, and local cone spacing as a basis from which we can better understand the development of its arrangement and the influences of that arrangement for vision in future experiments. Using previously described advances in spectral classification of cones with Adaptive Optics Optical Coherence Tomography Optoretinography (AO-OCT ORG) to trichromatically classify

retinal regions of two subjects across the central ~1-12° radius, with three regions classified along each meridian; 12 ROIs for each subject. This dataset far exceeds prior reports of cone-sampling across the retina per ROI of any report.

1.3 Motivation to pursue S-cone topography in particular

So, given the phenomenal novelty and value of the classified data at hand, why did I focus on S-cone topography in my thesis research, which has already been described in myriad papers since the late 80s?

When I embarked on a PhD mission to characterize spectral topography in humans, it made sense to first see how people had gone about studying S-cone topography. An analysis called the Density Recovery Profile (DRP) developed to studying the spatial distribution of retinal cell mosaics was used throughout the literature to determine whether there was “order” to the S-cone mosaic. This line of questioning came about due to observation that the S-cones in histological data appeared to be spaced apart with non-S cones between them, particularly in macaque retina. DRP applied to the spatial coordinates of S-cone locations in a classified region of interest (ROI) provides a measure of the density of S-cones as a function of distance from one another. If S-cones are spaced from one another, this should be reflected by low density of S-cones within some radius of each other in the DRP. To determine whether the density was significantly low within any radius of S-cones, the DRP was also collected for randomly selected subsets of cones from the same total cone mosaic. Many of these random arrangements, called Monte Carlo simulations, were synthesized to produce a range of DRP results against which statistical significance could be measured. This analysis had been used to determine whether the S-mosaic was significantly different from a random arrangement from S-cones in the literature for humans, non-human primates, and non-primate mammals.

DRP paired with Monte Carlo simulations can also be used to determine whether there is a significantly high density of cones at distances from each other. A point of interest in spectral topography is whether the L and M cones are arranged randomly with respect to each other. Some theorize that the sole distinction between L and M cones is their slight difference in peak wavelength sensitivity, determined by an unknown stochastic gene expression process that results in expressing the L or M type opsin. In this view, the L and M cones have no difference in their developmental progression to mature topography or their connectivity to postreceptoral circuits. In this view, the system is essentially agnostic to the distinction of L and M type cones until their different sensitivities are revealed by decoding

processes later in the visual system, and their spatial distribution relative to one another is thus random as the developmental mechanisms underlying mature topography regard them equally. However, there is some indication of non-random arrangement and connectivity of L vs M cones that may reflect trichromatic adaptations since the ancient addition of the third cone type.

Two of 9 ROIs shown in Hofer 2005 were found to have slight clumping of M-cones, and no ROIs in Roorda et al 2001 were differentiable from random. L and M cones were found to have a slight tendency toward clumping in macaque retina [Field 2011]. We wanted to evaluate whether there was clumping of L and M cones in our dataset where L and M cones can be distinguished more reliably, and whether the tendency to clump was higher in the peripheral retina.

Austin Roorda kindly shared with me the MatLab code he'd used to run DRP analysis on the S-cones assessed in his 2001 paper comparing human and macaque topography at ~1°, so that I could become familiar with it using the published data. My first goal was to reproduce the DRP analysis of that paper, then to move on to our trichromatic data. In Figure 4B the original S-cone DRP figure of Roorda 2001 depicting the S-cone topography from one macaque monkey ROI and 3 ROIs from two human subjects are depicted in the first column, with my recreations in the center column. In the monkey ROI (M5), the first bin of the DRP spanning 0-3 arc-min was significantly lower than that of 100 Monte Carlo simulations, indicating a nonrandom tendency of the S-cones to segregate themselves. The three human ROIs, binned at the same 3 arc-min intervals, had no such significantly low result. S-mosaics from these three ROIs had been deemed indistinguishable from random.

I began varying bin widths used in the analysis, and the results became more complicated. When I binned at smaller intervals, I had a result suggesting the human S-cones also had a significantly low-density ring surrounding them. In the far-right column of Figure 4, you can see the DRP result when I ran it with smaller bin widths. In this case, JWT and JWN S-cones were more distant from each other than random. AN was still not significantly spaced, but appeared more-so. wondered if this result was valid, or an artifact from choosing too small of bins. Cone density was lower for the macaque ROI than the human ROIs, and I wondered whether the effect of S-cone spacing scaled with cone diameter, which could explain the difference in results between species using common bin widths. While the cone density in the macaque ROI was lower, there were more cones sampled within it (because the monkey was anesthetized, lack of eye movements allowed for a larger classifiable area than in the awake humans) and substantially more S cones sampled than in human ROIs between the larger classified field

and higher S cone proportion in macaques. Bin widths for the DRP analysis had been determined by a technique meant to allow researchers to use the finest binning interval possible while retaining adequate sampling per bin. I wondered if it were truly statistically unsound to assess the human DRP at finer intervals, and wasn't sure what the choice of significance level really meant - it seemed arbitrary. I met with Austin Roorda to share the results with lower bin widths and ask for wisdom regarding the binning choices. He affirmed that the bin width choices were somewhat arbitrary, and thought the S-exclusion radius of the human S-mosaics I'd noticed could be real.

This was enough validation to set me on course to figure out the "right way" to measure the area surrounding S-cones where other S-cones are significantly unlikely to be located, which from here on will be referred to as the S-exclusion zone. This turned out to be more complicated than deciding on a binning interval, though that problem remained present throughout my thesis work. Ultimately, I uncovered many challenges to measuring the S-exclusion radius that hadn't been documented previously, and developed new approaches to evaluate the S-exclusion zone that facilitated novel insights about S-cone topography.

The remainder of this chapter serves to describe the state of S-cone topography research as I arrived at it and to summarize the approaches we used to add to this body of work. Chapter 2 is a paper published in 2022 championed by Vimal Pandiyan that describes spectral topography with AO-OCT, which I contributed to validation experiments of. Chapter 3 describes S-cone topography in two human subjects. Chapter 4 reports meta-analysis of classic and novel topography metrics with regard to their ability to capture properties of S-cone topography. Chapter 5 concerns independence of the S-mosaic. The concluding Chapter 6 summarizes the lessons learned, lingering hypotheses, future analytic approaches, and promising directions to explore how the information that can be encoded from a population of cones is influenced by cone topography.

1.4 S-cone topography

1.4.1 Overview

The S-cone sub-mosaic samples the short-wavelength end of the visual spectrum[32] and contributes to color perception across the visual spectrum[9]. S-cones evolved prior to L and M cones[12,33,34], which we will refer to as LM-cones in this report as we do not discriminate between the two. The elder S-cones are distinct from LM-cones in terms of morphology, physiology, connectivity, and distribution across the retina – the latter of which is the topic of this dissertation.

There is a low proportion of S-cones in the retina relative to L and M cones in most mammals, ~6 to 10% in humans[28,29,31,35–37] In many mammalian species the sparse S-cones have a tendency to be spaced significantly far apart from one another compared to randomly arranged simulations.

This non-random arrangement led to interest in the developmental processes responsible for the mature arrangement of S-cones and the effects of the non-random, semi-regular S-cone spacing for vision. It has been speculated that highly regular S-cone sub-mosaics would benefit visual acuity for short-wavelengths at the expense of detection-sensitivity, and that the semi-regular arrangement of S-cones may strike a balance between these features or even promote anti-aliasing.[28,38,39] Others have speculated that the regularity of the S-cones has little-to-no bearing on natural vision due to any combination of spatial summation during fixational eye movements, chromatic aberration of short-wavelength light, and/or pooling of S-cone inputs to retinal ganglion cell types thought to drive S-cone-mediated color perception.[40] Finally, findings that the S-cone mosaic is "independent" from the LM-mosaic suggest the S-cones disrupt the high regularity of non-S-cones, and that the semi-regular arrangement of the S-cones induces a patchwork of highly regular "iso-orientation areas" containing non-S cones.[41] In this view, the semi-regular S-cone topography is hypothesized to provide an anti-aliasing benefit to the high-acuity non-S-cone system.[38,42–44]

Differentiation and migration of retinal cell types and mature organization of the photoreceptor mosaic is a topic of thorough study, but physiological mechanism(s) underlying development of the S-cone exclusion zone, the area surrounding S-cones where other S-cones are significantly absent, are not yet understood.[45–49] There are two prominent hypotheses about the mechanisms responsible for its development: The first is that the exclusion zone could be purely the consequence of retinal expansion. In humans S-cones begin to differentiate and migrate across the retina weeks before L and M cones.[49] It has been observed that the spacing of the S-cones is random shortly after their initial migration to the plexiform layer. Therefore it could be that the exclusion zone emerges from this originally random distribution as the retina expands, and distance between the S-cones increases as a result. The second hypothesis suggests that local interactions between S-cones produce the zone - that due to secreted factors or dendritic interactions, either proximal S-cones are "pushed" away from each other or become apoptotic as the retina matures. It has been shown in macaque retina that S-cones in migration are already spaced from each other, which suggests such a spacing mechanism.[45] Human S-cones lack this spacing during migration, and it is yet unclear whether the mechanism underlying their exclusion zone is different from the macaque or whether it activates later in development. These hypotheses are not

mutually exclusive; any combination of these developmental processes could influence S-cone topography in tandem.

1.4.2 A brief history of S-cone classification

S-mosaic topography has been described in primates since the early '90s thanks to the unique morphology of S-cones, S-cone specific stains, immunohistochemistry, in situ hybridization, and in-vivo optoretinography. Early on, S-cones were differentiated from the other photoreceptor types morphologically, based their broad and long inner-segments relative to non-S-cones.[4144] The S-mosaic was first visually isolated using Procion yellow[50] and black[51] that stained S-cones in macaque retina. Positions of S-cones in and near the fovea were identified psychometrically by Williams et al 1981, leading to discovery of their absence in the human foveola, called the tritanopic zone.[2223] S-cones were identified by their lack of carbonic anhydrase expression in humans in a 1990 study[42], prior to the landmark report by Curcio et al 1991[35], which still informs much of our understanding of human S-cone topography today, that described S-cone density and proportion across the adult human retina with the first anti-S-opsin antibody labels. Bumsted et al 1999 verified co-labeling of an anti-S opsin and an in-situ hybridization probe specific for S-opsin mRNA, and compared the development of S-cone topography in human and macaque fetal retina. Martin et al 2000 re-evaluated regions assessed for S-mosaic regularity in Curcio et al 1991, comparing the regularity to S-cone labeled retinae from a variety of other primates. Cornish et al 2004[48] compared S-cone topography development in pre- and post-natal human macaque with S-cone labeled retinae, including the regions assessed by Martin et al 2000 and Curcio

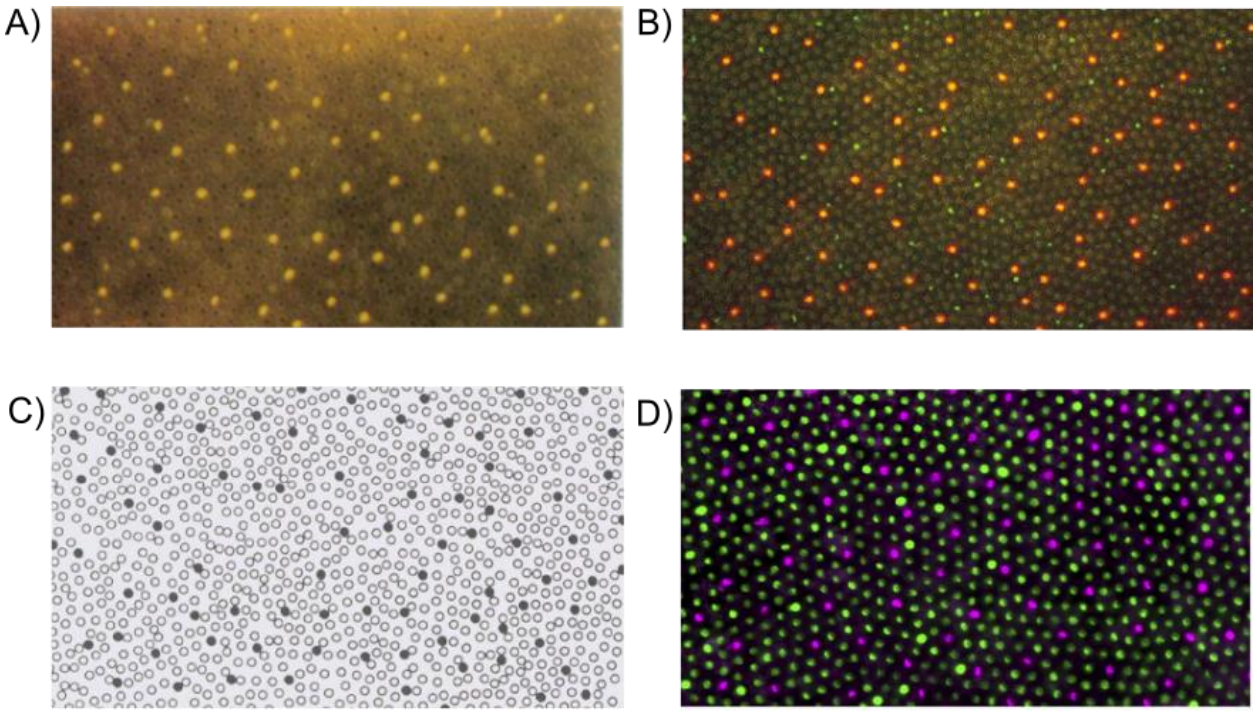

Fig 1.1 Examples of semi-regular S-cone mosaics across species. Retinae across mammalian species with labeled S-cones via various selective staining techniques. A) Macaque, S-cones (yellow), non-S-cones and rods (unstained). From De Monasterio et al 1981. B) Ground Squirrel, S-cones (orange), rods (green), and non-S cones (not stained). From Galli-Resta et al 1999. C) Human, data reconstruction of S-cones labeled with anti-S-opsin (black), non-S-cones (unstained). From Curcio et al 1991. D) Tree shrew, S-cones (purple), non-S-cones (green). From Hunt & Peichl 2014.

1991. Adaptive optics (AO) densitometry led to in-vivo classification of cones[3029283117] followed twenty years later by the higher- dimension and resolution AO Optical Coherence Tomography (OCT).[36,37,52]

1.4.3 The S-exclusion zone (which is *not* the tritanopic zone)

A critical feature of S-cone topography in some species is a tendency for S-cones to appear semi-regular, such that they don't tend to occur within some distance of each other in the cone mosaic. This was described qualitatively in the first Procion-stained retina as "an approximately regular array interspersed among unstained cones." The phenomenon has since been described consistently in macaques and found in other species including other non-human primates, tree shrews, and humans. Specialization of S-cone topography varies dramatically across mammals.[33,34,53,54] Those with a semi-regular arrangement have especially high visual acuity. The pattern is all the more interesting because high acuity vision is mediated by canonically non-S-cone-driven retinal output pathways. It has therefore been of interest to

characterize semi-regular S-cone topography across species, to eventually understand its developmental underpinnings and influence on vision.

The first attempts to characterize and simulate the pattern of semi-regular topography solidified the concept (if not the nomenclature used here) of the S-exclusion zone, the region surrounding S-cones where other S-cones are significantly unlikely to be found. Characterization of the S-exclusion zone is a major focus of this dissertation research, an effort that began with Shapiro et al 1985[51]. This report analyzed the S and non-S mosaics of macaque with cumulative distributions of inter-cone distances (Shapiro's "L-function" and metrics drawn from Voronoi Tessellations of cone mosaics (Shapiro's "A-function"). They determined that the diameter of the blue cone was roughly 20% the average blue-cone separation. They noted that the point pattern of blue cones has "considerable long range disorder" as well as "short range structure." This short-range structure is the S-exclusion zone, and beyond the short-range pattern of S-exclusion surrounding S-cone, they are found to be randomly distributed.

To approximate S-cone topography, Shapiro et al simulated an S-exclusion zone. The "elastic" version of the model was found to well represent the S-cones, which contained a "hard" and "soft" shell - the hard shell described the distance within which no S-cone would be of another, while the soft shell was a region extending from the hard shell where there was a lower-than-random but non-zero chance of an S-cone being located. These models were generated from random and grid point distributions with equivalent density to S-mosaics. Order was iteratively added to random distributions with a stochastic process restricted by ball-and-string restrictions, while disorder was likewise added to grid distributions. Both approaches could have elastic-ball parameters fit to reproduce the results of the L- and A-functions.

An improvement to the ball-and-string model was developed by Galli-Resta et al many years later to approximate the semi-regular S-mosaics of ground squirrels. This model simulates the S-mosaic within the observed cone positions of a mosaic region. Cones are iteratively selected at random from the mosaic to be included in the S-mosaic and are only added if their distance from cones already added to the S-mosaic satisfies a probabilistic minimum-distance rule – making it the "d-min" model. They found they could fit this model to well approximate S-mosaics, validated by Voronoi Tessellation metrics.

The human S-exclusion zone was first measured in three ROIs from one human in Curcio et al 1991, at eccentricities 1.2°and 10°(two ROIs were at ~1.2°, 0.35 and 0.36mm, labeled as "rod free zone" and

"foveal slope" respectively. It's not clear if these were adjacent.). They did not attempt to measure an exclusion zone, instead measuring the regularity of the S-mosaic using Voronoi cell area analysis compared to random arrangements of cones (referred to interchangeably in the literature as Monte Carlo simulations). They found that the two more peripheral ROIs outside the rod-free zone were non-random.

Following Curcio's work, the anti-S opsin method was validated with in-situ hybridization in Bumsted et al, which compared the prenatal development of foveal S-cone topography in humans and macaques. This work focused on the manifestation of the tritanopic zone in humans, which is not addressed in this dissertation because our classification methods cannot yet resolve the fovea with single-cell resolution.

Martin et al re-analyzed the two more peripheral ROIs with Density Recovery Profile (DRP), along with S-mosaics from a variety of non-human primates. Density Recovery Profile (DRP) is a method published in 1990 specifically to characterize regularity of retinal cell mosaics, of which there are many. This method is described in detail in Chapter 4. In brief, it measures the radius of the S-exclusion zone with a metric called Effective Radius. The maximum radius possible for a given density of cells is estimated, and the regularity of the cell mosaic is calculated as the squared ratio of the Effective Radius to that maximum radius, termed the packing factor. DRP has since become the state of the art for describing the S-exclusion zone.

Reanalyzed with DRP, the Curcio et al ROI along the foveal slope was deemed indistinguishable from random, while the peripheral one had a measurable Exclusion Radius. Human S-mosaic regularity fell somewhere in the middle of the primates tested, which displayed a gradient of S-mosaic regularity. A pattern to the spectrum of regularity was not obvious; for instance, they did not find that exclusion radii were present in all old-world monkeys, nor absent in all new world monkeys.

An additional two ROIs from an adult human retina were assessed with DRP in Cornish et al 2004, and once again, the ROI near the fovea (1.6°) was random, the more eccentric one (5.4°) was not. Cornish et al also looked at the S-cone topography of pre and post-natal human retina, finding that peripheral mosaics appeared regular by 20 weeks gestation, (10 weeks after S-opsin is first expressed in immature photoreceptors), but not so between 17 and 20 weeks. This indicated that the visual experience was not necessary to induce S-mosaic regularity, but it is not clear when the S-exclusion zone and the composition of the S-mosaic fully matures. As the fovea continues to develop postnatally, and it is

known that peak S-cone density increases postnatally, the temporal extent and potential visual-dependence of mature topography is unknown.

Roorda et al 2001 used densitometry to assess trichromatic spectral topography in 1 macaque and 2 human retinae at 1°ecc (and S-cone topography exclusively in 3 additional monkeys. All monkey, and no human, S-mosaics had an exclusion zone. In Hofer et al 2005, 9 ROIs mosaics were analyzed from 8 individuals at ~2°. Cumulative distributions of distances between real S-cones and Monte Carlo simulations were used to assess the regularity of S-cones. A significantly regular S-cone mosaic was identified in one ROI, and 4 additional ROIs were noted to have nonsignificant deviations from random "in the direction of regularity," but exclusion radii were not reported.

In total, these results suggested that the mature human retina has a semi-regular S-mosaic that is less regular than that of macaque and becomes irregular at about ~1-2 degrees eccentricity along the foveal slope. Unfortunately, there is no information about how the S-exclusion zone might vary with eccentricity (besides that it seems to be defunct most centrally) because there is a maximum of 3 ROIs per species in any of the primate S-cone topography literature. These studies were far more thorough in describing the proportion of S-cones and their density across the retina, which were simpler to compute over large areas. Regularity analyses rely on more complicated calculations and numerous simulated S-mosaics, meaning that the paucity of S-cone regularity analysis examples could be due to computational constraints.

1.4.4 Independence of the S-mosaic

Another curiosity about the S-mosaic addressed in previous work is whether it is "independent" from the LM-cone mosaic. Originally, this question was getting at whether the S-cones are "assigned" to the continuous topography of the total cone mosaic after its formation, or whether the formation of S and non-S-cone mosaics are independent processes.

Early curiosity on this topic arose from an observation in macaque retina that in the rod-free zone, the cones were still not arranged in a perfect triangular grid, where each cone would have 6 equally spaced neighbors. Rather, the cone mosaic was a patchwork of regions 20-40 micrometers in diameter where cones were hexagonally packed in rows that vary in orientation between patches (dubbed "iso-orientation areas"). This arrangement makes the photoreceptor mosaic far more disordered than a perfect grid like arrays of photosensors common to cameras. Pum et al noted cones at the junctions of

iso-orientation areas that had more or fewer than 6 cones. Early putative classification of cones as S-type using carbonic anhydrase and morphological differences indicated that these cones at the discontinuities tended to be S-cones.

In human tissue, Ahnelt et al 1987 noted that in addition to being more likely to have 5 or 7 neighbors than LM-cones, morphologically identified S-cones were found disproportionately to be one of the five or seven neighbors surrounding non-S cones in those instances. They also observed that outside the rod-free zone, S-cones were occasionally directly next to non-S-cones with no interleaving rods, and that such abutting did not occur between non-S-cones. Curcio et al corroborated the finding of S-cones occasionally abutting non-S-cones, but did not observe the S-cones to have more or fewer neighbors than randomly selected cones. The proximal-cones finding is ironically referred to as a "heterotypic interaction" between the S and LM mosaics in some texts, given the finding is thought to suggest a lack of interaction between the two. Hofer 2005 found that the standard deviation of number-of-neighbors was significantly large for S-cones in 3 of 4 subjects at ~1°, but did not elaborate further.

It has since been discovered that the S-cones are not "selected" from the established cone mosaic, as their opsin expresses before their centripetal migration across the retina, which initiates prior to the migration of non-S-cones and rods in humans. Still, it is unclear to what extent the migration of the other photoreceptor types influences the final position of S-cones. Some hypotheses have suggested that the S-cones are nudged about as the space between cones becomes tight, but evidence of S-mosaic "independence" suggests that the LM-cones are moving *around* the S-cones. It is of interest how the migration program varies between the cone types, and how they dynamically interact to produce mature spectral topography.

1.4.5 Hypotheses for developmental underpinnings of S-mosaic regularity

The retina becomes awash with the many retinal cell types in overlapping developmental waves that occur pre- and postnatally. In humans, cones begin differentiating in the incipient central retina after RGCs and horizontal cells, followed by amacrine cells, rods, bipolar cells, and Muller glia.[49] S-opsin is first expressed around 10WG in humans, when cell differentiation into cone progenitors is occurring rapidly in the ventricular zone of what will eventually become the fovea. Synapses are formed after differentiation. By 14WG, cell division has ceased in the fovea and a wave of cones has reached the optic disc. The spatial density of S-cone opsin increases threefold by 16WG. By 20 WG, cones cover the retina and are significantly regularly arranged. The S-cone density at this time is highest at the front of L/M

opsin expression that is just beginning. At this time and region there are many cells co-expressing S- and LM-opsins. In the mature retina, such cells are sparsely found throughout the periphery (0.01-0.02% of cones) and peak S-cone density approaches the foveola. [xiao & hendrickson 2000, Hendrickson 1992, Cornish 2004, Provis1985]. Postnatally, peak S-cone density continues to increase for an unknown period of time; S-cone density increases between the 6weeks postnatal and adult timepoints of Cornish et al 2004.

The factors at play that determine opsin expression and cell migration are obvious targets to understand the S-exclusion zone and independence of the S-mosaic. Much progress has been made in understanding the spatiotemporal dynamics of the photoreceptor mosaic's development, but it is still far from clear how the S-exclusion zone arises or the steering wheels driving peripheral migration that populate the retina followed by centripetal migration to develop the fovea. Factors related to thyroid hormone expression have been implicated as critical in establishing S-cone patterning in mice and human organoids.[49,55–57]. Enhanced S-cone syndrome, a condition where rods do not develop and instead would-be rod progenitors mature as S-cones, occurs with mutations to the NR2RE3 protein that suppresses cone fate and activates rod-associated genes.

Some hypotheses of the S-exclusion zone are not based on any trait of the S-cones excluding each other. These suppose that the S-cones populate the retina in a random arrangement during their migration. Then, either the expanding retinal surface draws the landed S-cones apart from each other, or infiltrating LM cones drive space between them, or both.

If the S-exclusion zone is formed by retinal expansion alone, we assume it should be fairly uniform in radius across the retina. However, if non-S cone infiltration also plays a role, the prediction is less clear. Centripetal migration of the non-S cones forms an incredibly dense mature fovea of cones, where S-cone density is its highest but the proportion of S-cones lowest. It could be the case that the flux of LM density to the central retina is sufficient to displace the cones apart, and one might expect if this were the case that the S-exclusion zone would increase in size with the non-S cone density, which would be consistent with the low proportion of S-cones. However, if non-S cones are truly shoving the S-cones about the retina, it's not clear how this would square with observations suggesting that the two mosaics are independent.

In the developing macaque retina, peripherally immature S-cones are found to be spaced apart from each other during their peripheral migration, suggesting an S-exclusion mechanism occurring at the level of the S-cones themselves. It is not known whether this is the same mechanism supporting the S-exclusion zone in humans activating sooner in macaques, or if the mechanisms vary. Furthermore, the spatiotemporal timing of the S and non-S opsin expression and migration is quite overlapped in the macaque, complicating comparison of spatiotemporal development.

Local cell interactions, as are suggested by the spacing of migrating immature macaque S-cones, have been implicated in many regular retinal mosaics. Many of the known mechanisms driving retinal cell mosaic regularity are not well supported in the case of S-cones. For instance, cholinergic amacrine cells induce like-type cell death of near-cells that underpin their regularity, but reports did not find evidence of adequate cell death in the period where the prenatal S-mosaic becomes regular. Some developing retinal ganglion cells (RGCs) secrete factors that prevent neighboring immature RGCs from differentiating into like types, but this does not seem to be the case for S-cones because they differentiate prior to their migration. Dendritic field interactions are known to be critical to development of many regular mosaics, allowing single cell types to evenly and completely sample the visual field. These interactions include coordination between cell-types that can drive ON and OFF type RGC mosaics to have receptive field centers shifted apart from one another. Dendritic interactions could induce cell death, or lateral migration of the cells apart from each other. Curcio et al 1991 speculated that this was not likely the case for S-cones because their short telodendritic processes are restricted to short radii about them and contact only subsets of non-S neighbors. Although, the larger processes of postreceptoral cells could also be implicated – for instance, S-cone bipolar cells outputting to the small bistratified RGC pathway have been found to be nonrandomly arranged such that they tend to be near S-cones [58], and the order of these events is unclear.

Ultimately, characterizing the S-exclusion zone across species, its variability across the retina, and spatiotemporal dynamics of its development will be crucial to solving these mysteries.

1.5 Dissertation Goals & Summary of Findings

A central goal of the thesis, that I'd meant to be a speed bump on the way to understanding all of color vision, was to characterize the S-exclusion zone. Our dataset had an unprecedented amount of coverage across the retina, an opportunity to learn about whether and how the S-exclusion zone varied across the retina. First I needed to make sure that I could faithfully measure them, else extant patterns could be

obscured or missed altogether. I'd learned from the Roorda 2001 data that the bin width choice could make or break the detectability of an S-exclusion zone. Looking through the literature, I found myself struggling to relate the results from different papers that varied in the sampling, density, and proportion of S-cones, and the particulars of the analysis applied.

I also struggled to interpret *how* different the S-mosaics in the literature were from random ones. Monte Carlo simulations supplied a lower bound, but the upper bound had been defined more vaguely by a "maximum radius" described by Rodieck and used to calculate the Packing Factor, the go-to metric for assessing the regularity of a retinal mosaic. It was calculated from S-cone density alone. Not only is this estimate vulnerable to assumptions of a square ROI, I found the maximum radius insufficient to consider as an upper bound of S-mosaic regularity. I was curious what the upper limit of regularity was for an actual sparse subset of cones drawn from the cone mosaic. The regularity of the cones becomes less regular with eccentricity as they become larger in diameter, the S-cones become larger in diameter relative to non-S cones, and the cones become interleaved with rods. How does this underlying geometry effect the regularity of a simulated S-mosaic given the simple rule that they be as regular as possible?

If the only characteristic differentiating an S-mosaic from a random one is the S-exclusion radius, how does the regularity of that mosaic change depending on the proportion of S-cones? Previous work assessed S-cone density with respect to S-mosaic regularity and found no association, but did not report the proportion of S-cones. In most cases, the proportion cannot be calculated because only the quantity and density of S-cones are reported.

1.5.1 Development of methods better suited to characterizing the S-exclusion zone

A major development of this research was Concentric Ring Analysis (CRA) to characterize the S-exclusion zone. It was devised in response to the complications we uncovered when assessing the efficacy of classic methods to detect and describe the S-exclusion zone. Preliminary work that eventually motivated CRA is described in Chapter 4. Computational experiments described there suggested reliable results could not be obtained using the classic approach (Density Recovery Profile (DRP)), nor a similar approach we applied in attempt an attempt to improve upon DRP's limitations (Two-Point Correlation (2PC)).

In both cases, the unresolvable weakness of the DRP and 2PC procedures was that they rely on a histogram of the distances between all S-cones in an ROI. While systematic approaches to setting bin widths for these histograms have been applied in the past, we found they were inadequate to reliably detect, let alone accurately describe, the S-exclusion zone. Our effort to identify a reliable binning strategy was not successful. We found we could only do so with a-priori knowledge of S-exclusion zone properties that are only possible in simulation experiments. Even then, we noted a concerning level of variability in the results ExR results, which of course cast uncertainty on regularity metrics calculated from the ExR.

Preliminary 2PC results suggested most of our observed mosaics were roughly twice µINDa across the retina, but we determined that uncertainty in the 2PC ExR metric was too high to be confident in the pattern. For an S-exclusion zone that scales with µINDa, we reasoned that neighboring cone relationships could be more important to describing the pattern than explicit distances, even when those distances were skewed by µINDa. µINDa is only an estimate, after all.

The actual distance between neighboring cones can vary greatly across a single ROI, for several reasons: 1) The regularity of the overall cone mosaic decreases as the cones mosaic becomes increasingly interspersed with rods, meaning variability in distances between cones increases. 2) Cone density can vary across a single ROI, leading to a gradient from µINDa overestimating the distance between cones where density is highest, and underestimating it where density is lowest. The problem is exacerbated near the foveal slope, where cone density varies most rapidly with respect to eccentricity. 3) Previous reports have shown that S-cones have more variable inter-neighbor distances than non-S cones, and our results robustly confirm this (see Chapter 5). In this dataset, S-cones tend to have neighbors that are further away than non-S cones at eccentricities < ~2°, and conversely, they have nearer neighbors at higher eccentricities. Both cases make µINDa relatively less representative of S-cone neighbor distances.

All signs showed that if the pattern of the S-exclusion zone was dependent on neighboring cone relationships, it would be difficult to represent with any spatial point process. Condensing the spatial characteristics of the S-mosaic into a binned histogram of inter S-cone distances blurs information about those relationships. So, we returned to the Voronoi tessellation of the cone mosaic (AVT), containing the information about neighboring cone relationships, as an alternative. Concentric Ring Analysis (CRA) was developed, in which the prevalence of S-cones is assessed in terms of concentric rings of cones surrounding S-cones. The concentric rings are determined from the neighbor relationships contained in

the AVT. One may think of this as binning by distance in terms of number-of-cones away. In Chapter 4, we demonstrate that this analysis was more sensitive to detecting the S-cone exclusion zone than the spatial point process approaches, and even tends to pick up a peak in S-cone prevalence following the S-exclusion. Both are strong evidence that this paradigm is better suited to describing the human S-exclusion zone.

1.5.2 Summarized Characterization of Human S-cone topography

Novel findings about the patterning of the S-exclusion zone across the retina, and the influence of that pattern on S-mosaic regularity, were facilitated by the advent of CRA. These are described in Chapter 3. CRA revealed exclusion zones for 23 of 24 ROIs spanning the central retina. Twenty of these had an exclusion zone that spanned the first two concentric rings of cones surrounding S-cones. This is a novelly identified pattern of the S-exclusion zone that persists at 1-2degrees eccentricity. It suggests that local cone interactions that scale with the distance between neighboring cones underlie the S-exclusion zone. Applying CRA to the largest macaque and human ROIs of Roorda et al 2001, we found the same pattern. The methods meta-analysis of Chapter 4 and the re-analysis of data from Roorda et al 2001 in Chapter 3 suggest that previous findings of random S-mosaics near the fovea could be explained by methodological weaknesses, though it is unclear without a direct re-assessment.

A surprisingly stark finding was made with regard to the Independence of the S-mosaic, described in Chapter 5. We found that the S-cones had significantly different distances from their cone neighbors than did non-S cones, such that they had significantly near neighbors centrally (< 3 °), and conversely had significantly far neighbors at higher eccentricities. While significantly near neighbors have been noted several times in the periphery, and significantly far neighbors have been noted once centrally, this is the first time both have been noted in a single subject. These findings support independence of the S-mosaic manifesting differently with eccentricity, and we hypothesize this may hinge on the presence of rods.

Together, these findings advance our understanding of S-cone topography in humans and the approaches we use to assess the S-exclusion zone. Our findings better prepare the field to understand the comparative anatomy, development, and functional consequence of semi-regular S-mosaics.

2: Characterizing cone spectral classification by optoretinography

I was the second author on the following peer-reviewed publication, which details the use of reflective mirror-based AO line-scan optical coherence tomography for spectral cone classification. My contributions were analysis related to validation of the method - I did not contribute to creation of the system or data collection. The sections I contributed to and my role in them are as follows:

2.1 Contributions

2.1.1 “2.8 Cone-by-cone alignment for comparing densitometry and ORG”

Two regions of the perifoveal retina that had been classified ~6-7 years previously with AOSLO were re-classified using AO-OCT. To compare the classification between the two, cones had to be matched between the two images. This was not a trivial task, as the paper notes “the two datasets obtained from these different instruments feature significantly different scales, orientations, cone appearances, and motion-induced distortions.” I first performed this task completely manually and with inadequate confidence, using semitransparent overlays and my best attempt to align small areas of the mosaic then extrapolate. The process was then greatly improved with the Retina Map Alignment software tool developed by co-authors James Fong and Rishi Upadhyay. The tool performed an initial automated coarse scaling, rotation, and position alignment. From there, it provided an interface for making manual alignments that iteratively applied affine transforms to one of the two images, gradually stretching components until the corresponding cones overlapped between the images. I performed the cone alignment on the two ROIs using this procedure, then James Fong did as well for validation. Our cone alignments were nearly identical (842/854 and 565/567 aligned cones in common, 98.6% and 99.6% agreement), except for a few cones primarily at the edges of the ROI (where there is less information from the position of neighboring cones to make a confident judgment) which were excluded.

2.1.2 “3.3 Dysflective cones”

In the process of cone-by-cone alignment, we discovered in the two datasets for each subject that there were a few cones visible in the images created by each modality that were not visible in the other. In the image where the cone was absent, there was a dark spot that looked like a hole in the mosaic. We were able to align all the cones surrounding the hole with cones in the other image, which would have a clearly visible cone where the hole was. Because there were holes in images from both modalities, it

clearly was not just the case that the holes were due to cone loss between the imaging sections or due to one technique versus the other. Instead, we had reason to believe that the appearance of the hole where a cone should be was a phenomenon of temporary abnormal waveguiding from the cone outer segment. We thus referred to the non-visible, but-extant, cone as “dysflective.” The cause of the dysflectivity is unknown, but we hypothesize it is a consequence of the natural disc shedding and renewal process of the cone outer-segment. For cones that were visible in the AOSLO image but not the AO-OCT image (2 cones in one ROI, 3 in the other), we used the cone transfer tool to derive the coordinate where the cone *should* have been in the AO-OCT image. We then found that despite not being able to visually see the cones in the intensity image, there was a normal cone ORG response from that location that allowed them to be spectrally classed as L and M type. Assessment of this phenomenon was an unexpected boon of using the Retina Map Alignment tool, and made it possible for us to classify every cone that was classified in the AOSLO images.

2.1.3 “3.5. Densitometry vs. ORG classification comparison”

Following the cone-by-cone alignment, I compared classification between the AOSLO and AO-OCT modalities. I reported the overall agreement and confusion matrices detailing the prevalence mismatch between cone types (Figures 9 and 10, and Table 2). The agreement was 91.6% and 90.4% when cones that were not classified with densitometry were included, or 92.9% and 91.4% when they were excluded. Unsurprisingly, mismatches were most likely to occur near the edges of the classified ROI (where effects of image torsion are greater and ORG responses are noisier) or under the shadow of blood vessels (which are more severe in the densitometry images). I found that the classification was most consistent between modalities for L-cones (92%, 97%), less for M-cones (90%, 88%), and quite low for S-cones in one subject (93%, 59%). In the first subject, mismatches were dominated by cases where the cone was classed L in one modality and M in the other. In the other, nearly half of mismatches were classed S with ORG and L with densitometry.

2.1.4 “Test-retest reliability in ORG cone classification”

I did not perform this test myself, but I did advocate insistently for it. Without testing the reliability of the classification in ORG, we could not say to what degree discrepancies between densitometry and ORG classification were due to the modality differences versus intra-modality variability. At the time, uncertainty in our classification was only quantified in terms of overlap between clusters of peak change in optical path length (OPL). Given the unknown role of the disc-shedding cycle in adding noise to the data, I argued that performing classification on data from separate days would be more beneficial than

comparing classification from two halves of data collected from one day's session. I was particularly interested in the classification reliability of S-cones, as my work had become centered on characterizing S-cone topography in ROIs classified with ORG. Because we use a 660nm stimulus in our classification paradigm, S-cones are classified as those lacking a stimulus response. I wanted an idea of whether this negative-identification of S-cones was especially prone to error. A second classification experiment was performed in an ROI at 1.5° in one subject with 4.2% mismatch, and at 4° in another subject with 2.6% mismatch. S-cones were involved in ~19% of mismatches at 1.5° and 62.5% at 4°. S-L mismatch was not prevalent, and we speculate that misidentification of S-cones as L-type in densitometry could be an artifact of the model-fitting process used to cluster the cone types in that paradigm.

2.2 Published Manuscript

Characterizing Cone Spectral Classification by Optoretinography

VIMAL PRABHU PANDIYAN,[1,5] SIERRA SCHLEUFER,[1,2] EMILY SLEZAK,[1] JAMES FONG[3], RISHI UPADHYAY[3], AUSTIN ROORDA[4], REN NG[3], RAMKUMAR SABESAN[1,2*]

[1]Department of Ophthalmology, University of Washington School of Medicine, Seattle, WA

[2]Graduate Program in Neuroscience, University of Washington, Seattle, WA

[3]Electrical Engineering and Computer Sciences, University of California, Berkeley, Berkeley, CA

[4]Herbert Wertheim School of Optometry and Vision Science, University of California, Berkeley, Berkeley, CA

[5]vimalbme@uw.edu,

**rsabesan@uw.edu*

Abstract: Light propagation in photoreceptor outer segments is affected by photopigment absorption and the phototransduction amplification cascade. Photopigment absorption has been studied using retinal densitometry, while recently, optoretinography (ORG) has provided an avenue to probe changes in outer segment optical path length due to phototransduction. With adaptive optics (AO), both densitometry and ORG have been used for cone spectral classification, based on the differential bleaching signatures of the three cone types. Here, we characterize cone classification by ORG, implemented in an AO line-scan OCT and compare it against densitometry. The cone mosaics of five color normal subjects were classified using ORG showing high probability (~0.99), low error (<0.22%), high test-retest reliability (~97%) and short imaging durations (< 1 hour). Of these, the cone spectral assignments in two subjects were compared against AOSLO densitometry. High agreement (mean: 91%) was observed between the two modalities in these 2 subjects, with measurements conducted 6-7 years apart. Overall, ORG benefits from higher sensitivity and dynamic range to probe cone photopigments compared to densitometry, and thus provides greater fidelity for cone spectral classification.

1. Introduction

Signals from the three cone spectral classes in the retina form the basis for color perception [1]. Their relative proportion and arrangement shapes and constrains how wavelength information from the external world is coded in the visual system to create the rich palette of hues that most humans perceive. Short-wavelength cones (S-cones) can be differentiated in histology [2], but the remarkably similar morphology and protein structure of long and middle-wavelength cones (LM-cones) has long precluded the creation of imaging techniques and antibodies to segregate them in a cellular-scale assay *ex vivo*. Until the advent of adaptive optics (AO) to overcome the optical aberrations of the eye [3] and resolve cone photoreceptors in living humans, there was virtually no information about the arrangement of individual LM-cones in primate retina. In fact, AO retinal densitometry to delineate the spectral types of cones by Roorda and Williams [4] was one of the very first scientific applications of AO upon its introduction to the eye in 1997.

Densitometry has long been used to study various biophysical properties in cone photoreceptors, including waveguiding efficiency of the inner & outer segments, optical density, and photosensitivity of chromophores housed in their outer segments [5-8]. Its principle rests on using the absorption of light by photopigments as a gauge to measure the aforementioned biophysical properties. For cone spectral typing, differential absorption by the three photopigments in LMS-cones is used to separate them by their spectral type. An AO fundus camera was first used for this task, enabling the visualization of cone spectral types in humans and non-human primates [4, 9, 10]. In 2015, the feasibility of using an AO scanning laser ophthalmoscope (AOSLO) to classify cone spectral types was tested [11]. In addition to the advantages of increased axial and lateral resolution, contrast and signal-to-noise ratio, AOSLO densitometry allowed imaging the dynamic changes in photoreceptors upon light capture. Together, this enabled cone spectral classification with high efficiency with the time taken per subject ranging between 3 to 9 hours, and requiring an average of 8 – 15 repeat measurements per bleaching condition to boost the signal-to-noise ratio. In contrast, the AO fundus camera needed averages of up to 50 repeat measurements across 5 days in each bleach condition[4].

Recently, Zhang et al. 2019, 2021 [12, 13] showed improved precision and efficiency for mapping cone spectral types using an AO point scanning spectral-domain optical coherence tomography (OCT) instrument in phase-resolved configuration. The principle of the measurements rests on imaging light-evoked changes in the backscattered optical phase arising in the cone outer segment in response to a bleaching stimulus, also referred to as optoretinography or ORG [14, 15]. These changes in phase were converted to optical path length (ΔOPL) to serve as a quantifiable gauge for measuring light propagation after bleaching in the outer segment and the magnitude of ΔOPL scaled with increasing bleach strength. By adopting a bleaching light that differentially activated L, M and S-cones, it was demonstrated that the ΔOPL response arising from individual cones could be readily segregated into three cone sub-types. In 2020, Pandiyan et al. demonstrated a line-scan AO-OCT instrument for volumetric imaging

of the retina that could record retinal cross-sections up to the maximum rate of 16000 B-scans/sec [14,16]. The increased speed is the result of parallel acquisition of a linear spatial imaging field in a 2D camera after diffraction through a transmissive grating, such that after a Fourier transform, a cross-sectional B-scan is obtained in a single acquisition. This comes at the cost of loss of confocality in one dimension compared to a traditional point scan configuration. Despite this, it was demonstrated that the instrument could image different scattering structures within the retina at cellular resolution, including retinal ganglion cells, macrophages, rod cells, foveal cones & retinal pigment epithelial cells [17]. Using this line-scan OCT instrument, Pandiyan. et. al [16, 17] demonstrated the feasibility of cone spectral classification, following the general protocol established by Zhang et al. 2019. Notably, cone spectral types were classified at an eccentricity of ~0.3° from the foveola, enabling the first in vivo demonstration of decreasing S-cone proportion in the fovea [17].

It is instructive to compare the ORG and densitometry in terms of their mechanism of action and dynamic range. As explained below, ORG has greater than 20x greater dynamic range for comparing photopigments across cone spectral types as compared to densitometry. This provides a fundamental benefit to the signal-to-noise ratio in ORG for classification; signal corresponds to a surrogate measure of photopigment concentration while noise is contributed by various common factors for both including low retinal reflectivity, the limit to light collection set by the numerical aperture of the eye, eye movements, reflections from retinal layers besides the cones, blood flow and more. The higher dynamic range is expected to reach similar or better accuracy in ORG with lower numbers of repeat measures, thus improving speed and efficiency.

Densitometry uses the same light source for imaging photoreceptors and bleaching photopigment, typically centered at 550 nm where the spectral sensitivity of LM-cones is high, *and* similar to each other. After dark-adaptation and regeneration of cone photopigment, the retina is exposed to the imaging and bleaching light. The backscattered light encodes the cone locations in the retinal image, and simultaneously carries information about absorption by the photopigment. For instance, the S-cones are relatively insensitive to a 550 nm imaging light and therefore maintain their backscattered intensity after exposure to it. LM-cone photopigments on the other hand absorb this light and appear darker than the S-cones immediately after light onset. With increasing bleach of LM-cone photopigments, their concentration, and hence absorption decreases, consequently leading to an increase in the backscattered image intensity. This relationship between image intensity and photopigment concentration for LM-cones is depicted in Fig. 1(a) (brown and black dashed curves respectively). The relative change in image intensity immediately after stimulus onset and after a full bleach is referred to as the optical density and signifies the maximum photopigment-dependent signal available for probing its characteristics. Optical density is computed as the base 10 logarithm of the ratio of image intensity, post to pre-bleach. Neitz et al. 2020 [18] measured individual cone optical density using AOSLO densitometry for a range of visible wavelengths from 496 nm to 598 nm. A maximum optical density of 0.41 log10 units (2.6 times) was observed at 543 nm, i.e., a 2.6x change in image intensity is available as the dynamic range to probe LMS-cone photopigments.

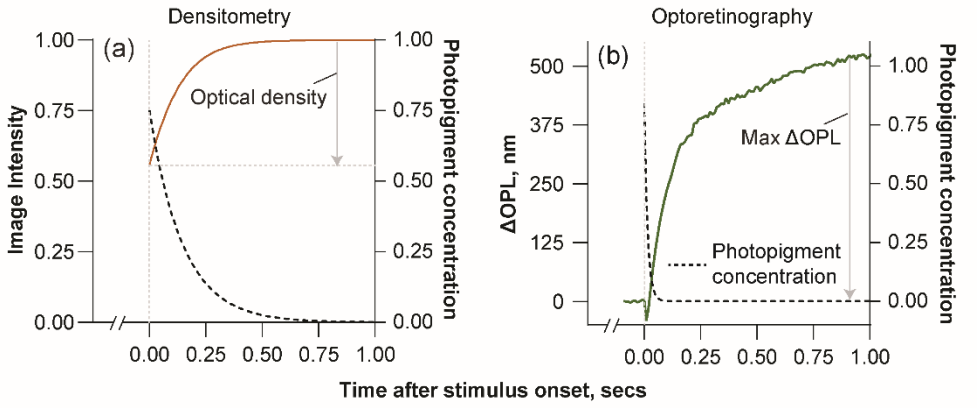

Figure 1: The dynamic range of ORG is ~20x improved over densitometry. Densitometry (Fig. 1(a)) measures the time varying change in the backscattered image intensity (brown curve, left y-axis, Fig. 1(a) from the retina as the photopigment concentration (black dashed curve, right y-axis, Fig. 1(a) is reduced in the cone outer segment with a bleaching stimulus. ORG (Fig. 1(b)) measures the time varying change in ΔOPL in the cone outer segment (green curve, left y-axis, Fig. 1(b) as the photopigment concentration (black dashed curve, right y-axis, Fig. 1(b)) is reduced with a bleaching stimulus. The dynamic range is the maximum obtainable change in the photopigment dependent signal attributed to a bleach (represented on the left y-axis for both), equal to ~2 – 2.6x for densitometry and up to at least 50x for ORG.

In contrast, the stimulus-evoked ΔOPL shows a significantly greater pigment-dependent change, scaling in magnitude from 10 – 500 nm with increasing bleach from 0.3 - 50% [14]. Fig. 1(b) shows ΔOPL vs. time for a 50% bleach using a 520 nm stimulus. Considering 10 nm as the noise floor of the measurement, the ratio of post to pre-bleach ΔOPL can be as high as 50x, indicating the dynamic range available to probe LMS-cone photopigments in ORG. The mechanism of action of ORG is currently unknown, though its bleach dependence suggests an involvement of the phototransduction amplification cascade [14, 19] that ultimately benefits its dynamic range.

In this article, we sought to investigate the correspondence between densitometry and ORG for cone classification in the same subjects and compare their fidelity for the task. First, we establish our ORG protocol for this task and ascertain its test-retest reliability by measuring the same subjects and eccentricities across different days. Variations in reflectance of cones caused due to interference, disc shedding and renewal, and shadows of blood vessels negatively affect both paradigms for classification [20-22]. Next, we ascertain whether cones with abnormal reflectivity exhibit normal function in ORG sufficient to identify their type. Finally, we compare the spectral assignments between the two paradigms with respect to the specific cone types and their spatial arrangement.

2. Methods

2.1 Reflective mirror based line-scan AO-OCT

A line-scan spectral domain OCT system equipped with AO, described previously [17], was used for ORG with cellular resolution. Briefly, a wavelength band at 820 ± 40 nm was selected from a supercontinuum light source (SuperK EXR-9OCT, NKT Photonics, A/S, Birkerød, Denmark) for imaging the retina. A 980±10 nm superluminescent diode (SLD) (IPSDD0906, Inphenix, USA) was used for wavefront sensing and AO correction. A 660±5 nm light-emitting diode (LED) was used as the bleaching stimulus to differentiate the cone types because L-cones have 13 times higher sensitivity than M-cones, and S-cones have negligible sensitivity at this wavelength [23]. The wavefront sensing and the imaging beams were combined with a short pass filter and these two beams were combined with the bleaching stimulus using a long pass filter. Light backscattered from the retina was split into two beams using the same short pass filter in the detection arm. The 820 nm light scattered from retina was captured either with a line-scan camera to optimize photoreceptor image focus in an *en face* image stream, or with a custom-built spectrometer for OCT. The spectrometer consisted of a diffraction grating (WP-600/840-35X45, Wasatch Photonics, USA) and a fast 2D camera (FASTCAM NOVA S16, Photron, USA). The fast 2D camera was used to capture the spatial and spectral dimensions along its 2 axes simultaneously to yield a cross-sectional OCT B-scan in a single frame. An anamorphic configuration was used to optimize the spatial and spectral dimension independently [16]. The sensitivity of the system is 92 dB.

2.2 Subjects

Five color normal subjects were recruited for the study after an informed consent explaining the nature and possible consequences of the study. The research was approved by the University of Washington institutional review board and experiments were performed in accordance with the tenets of the Declaration of Helsinki. Of the 5 subjects, one was Caucasian male, two were female Caucasians and two were Asian males. Two of the color normal retinae were cone-typed earlier using densitometry, published in Sabesan et al. [11]. Subjects S3 and S4 in Sabesan et. Al. are S4 and S5 respectively in this paper. In this study, cone classification for S4 and S5 with ORG, at 1.5° and 2° eccentricity, respectively, was compared against data from densitometry in Sabesan et al., separated in time by 6-7 years. In all other subjects, cone classification was performed at 1.5°. temporal eccentricity. For comparison of cone classification across two days, subjects S2 and S4 were imaged at 4°. and 1.5°. eccentricity, respectively.

2.3 Imaging protocol

Subjects were dilated and cyclopleged using 1% tropicamide and/or 2% phenylephrine. They were placed in a dental impression to stabilize head movement. Their pupil was aligned to the optical axis of the instrument using a three-axis translation stage assisted with a pupil camera. The aberrations were measured and corrected in real time using the wavefront sensor and deformable mirror. The retinal image captured in the line-scan camera was optimized to focus the cone photoreceptors. The system was then switched to line-scan OCT mode for further experiments. For ORGs, AO-OCT volumes were recorded after subjects were dark-adapted for 1-3 minutes to allow for sufficient regeneration of cone photopigments. The 660 nm, 20 ms LED flash was delivered after the 10^{th} volume.

We chose 660 nm because at this wavelength L-cones have greater sensitivity than M-cones by ~11 times, and S-cones have negligible sensitivity. The estimated photon density for 660 nm stimulus was 25.1 x 10^6 photons/μm^2. We prefer to report the bleach strength in units of photon density "at the retinal surface" and not in units of percent or fraction bleach per se. This is because converting the photon density to bleach strength requires accounting for factors related to the cone photoreceptor that vary between subjects and eccentricity, for example, the outer segment length, inner & outer segment diameter and Stiles-Crawford effect [24]. We optimized the stimulus duration to maximize the ΔOPL difference to separate LMS-cones. The B-scan rate was 12000 scans/sec. Each volume contained 600 B-scans, and each video contained 50 volumes. The overall recording time was 2.9 secs, wherein each volume is acquired in 58 ms (including 8 ms dead time for galvo scanner return where recording is paused).

Typically, unless otherwise stated, 10 recordings were taken for averaging and improving signal-to-noise ratio. Accounting for any rejections of acquired volumes due to motion artifacts, between 7 to 10 recordings were analyzed in each subject. The schematic for cone classification using ORG is shown in Fig. 2. The OCT volume was segmented to access the cone outer segment (Fig. 2(a)). After dark adaptation, photopigments regenerate in LMS-cones, indicated with red, green and blue shades respectively on the cone outer segment discs in Fig 2(b). Following the bleaching stimulus, L, M, and S-cone photopigments are depleted with decreasing magnitude in turn, proportional to their sensitivity to the 660 nm wavelength (Fig. 2(c)) [23]. The timing diagram of a representative ORG cone classification experiment is shown in Fig. 2(d).

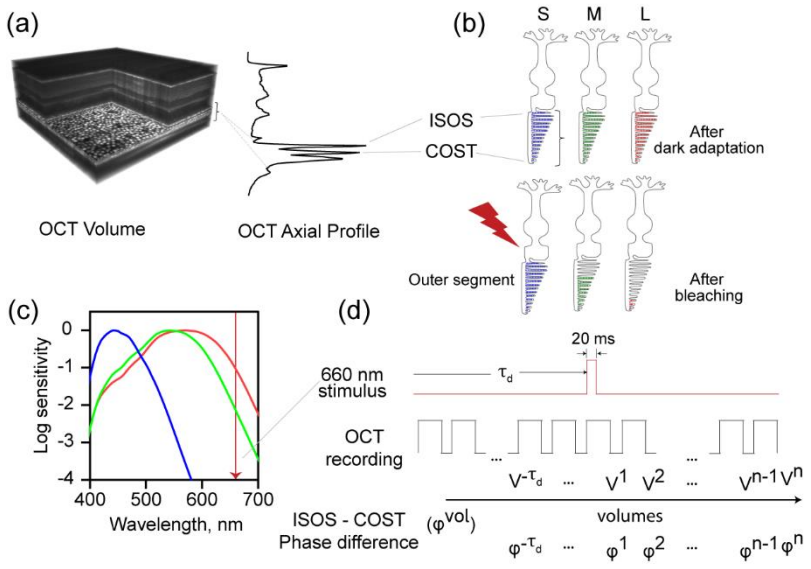

Figure 2: Schematic for cone classification using ORG. (a) The registered AO line-scan OCT volume was segmented at the cone inner-outer segment junction (ISOS) and the cone outer segment tips (COST) to access the outer segment. (b) After dark adaptation, photopigments regenerate in all cones. After a 660 nm stimulus, L-cones have highest bleach and activity, followed by M-cones and then S-cones, as dictated by their decreasing spectral sensitivity to 660 nm wavelength in (c) [23].

(d) The onset of the 20 ms stimulus flash occurs at τ_d = 0.58 sec or after the 10th volume. OCT volumes (n= 50) were recorded, reconstructed and registered. The phase difference between the ISOS and COST in each volume was calculated and treated to the steps in Section 2.4 to obtain a measure of OPL change in each cone, evoked by the stimulus.

2.4 OCT image processing

Typical steps were followed for OCT image processing. The details of the processing and ORG extraction are detailed in reference [16]. Each recorded 2D spectrum $\big(I(x,y,\lambda)\big)$ was treated to background subtraction, k-space resampling $\big(I(x,y,k)\big)$, and a Fourier transform $I(x,y,z)$ to yield an OCT volume. All volumes were registered using segmentation-based 3D registration [25]. Once the volumes were registered, each OCT volume was referenced to the mean of all the volumes that were recorded before the start of the stimulus to cancel the arbitrary phase at each pixel. Then, the mean of 3 axial pixel complex values, centered at the boundaries of the ISOS, $I_{ISOS}(x,y)$ and the cone outer segment tips (COST), $I_{COST}(x,y)$ was calculated. The phase difference $I_{ISOS/COST}(x,y)$ between these two layers was obtained by multiplying the complex conjugate of COST with the ISOS layer. The complex numbers $I_{ISOS/COST}(x,y)$ were averaged over the collection aperture (5 x 5 pixels, ~3.7 x 3.7 µm) of a cone photoreceptor to yield one complex number per cone in a volume. The same was repeated for the 50 volumes in the 17.2 Hz time series to give $I_{ISOS/COST}(t)$.

2.5 Complex average vs Angle average

We evaluated two approaches for averaging across repeat measurements to improve signal-to-noise. The first approach involved taking the *complex average* of individual ΔOPL vs. time series as below:

$$\overline{\boldsymbol{I_{ISOS/COST}(t)}} = \frac{\boldsymbol{1}}{\boldsymbol{N}}\sum_{\boldsymbol{i=1}}^{\boldsymbol{N}} \boldsymbol{I_{ISOS/COST}(t)^{i}} \tag{1}$$

where N is the number of recordings, and $I_{ISOS/COST}(t)^{\,i}$ is a complex valued time series for one measurement. The phase ($\Delta\phi\overline{I_{ISOS/COST}(t)}$) was computed by calculating the argument of the averaged complex time series. For phase responses that exceeded $\pm\pi$ radians, phase was unwrapped along the time dimension. The mean change in OPL ($\overline{\Delta OPL(t)}$) was calculated as

$$\overline{\Delta OPL(t)} = \lambda_o \times \frac{\overline{\Delta\phi_{ISOS/COST}(t)}}{4\pi} \tag{2}$$

where $\lambda_o$is the central wavelength equal to 820 nm.

In the second approach, the argument of each individual complex valued time series was obtained to yield the phase, unwrapped if needed and converted to ΔOPL using equation 2. This approach represents the *angle average*. The mean $\overline{\Delta OPL(t)}$ of all recordings was calculated as

$$\overline{\Delta OPL(t)} = \frac{1}{N}\sum_{i=1}^{N} \Delta OPL(t)^i \qquad (3)$$

where N is the number of recordings $\Delta OPL(t)^i$ is the time series of ΔOPL for one measurement. An alternate strategy to the angle and complex average is performing the circular mean, a strategy used in cases where the data are inherently circular and/or periodic [26].

2.6 Clustering analysis

The ΔOPL vs. time trace for each cone was obtained by averaging the individual repeat trials. For segregating L, M and S cones, the ΔOPL averaged over the time after stimulus onset between 0.7 – 1 sec was calculated for every cone that was visible in AO-OCT structural images. A histogram of the time averaged ΔOPL (maximum ΔOPL elsewhere in this article) was fit with a sum of three 1-dimensional Gaussians. The clustering method followed here is analogous to a 3-component, 1-dimensional Gaussian mixture model [27]. The intersection of the component Gaussians separated the clusters into the three cone types. Each classified cone within a cluster is associated with an error percent or uncertainty, and a probability or likelihood of its assignment. Error is a group measure for S vs. M, and M vs. L-cones, defined as the area of overlap between their respective component Gaussians. Probability is a measure specific to each cone within a cluster, defined as the ratio of its component Gaussian value to the sum of all Gaussians at a given x-axis location (ΔOPL). High or low probability is observed when a given cone's ΔOPL lies near or distant from the fitted Gaussian respectively.

2.7 Comparison of cone spectral classification across different days to assess test-retest reliability

To assess test-retest reliability, cone classification was conducted on two different days for two subjects, at one eccentricity each. Subjects S2 and S4 were classified at 1.5°. and 4°. eccentricity respectively. The recorded OCT volumes on both days were registered together to select the same cones for classification. Cones so-classified were compared for cone-type specific mismatches between days. Bland-Altman analysis [28] was performed to compare the maximum ΔOPL across both days to evaluate their repeatability.

2.8 Cone-by-cone alignment for comparing densitometry and ORG

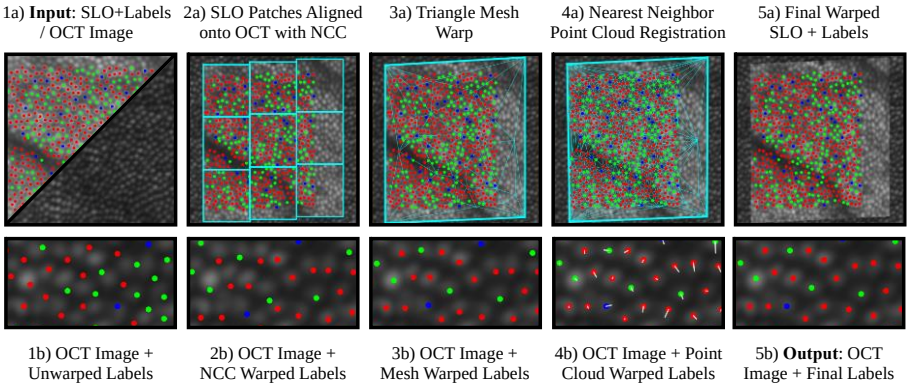

Figure 3: Description of the Retina Map Alignment Tool to find matching cones between an SLO image and the OCT en face image at the COST. In this example, we refer to a cone's coordinate and LMS classification as its 'label,' and show each label as a false-color red, green or blue spot. We use the tool to warp the labeled SLO image such that the cones' coordinates align with the OCT image. This warping then provides the desired cone pairing between the two datasets. The steps involved are shown left-to-right going from inputs to outputs. The bottom row shows a zoom-in of the SLO labels as they are gradually warped to align with the cones visible in the OCT image. From left to right: 1a) The inputs are the cone-labeled SLO image and the destination OCT image. 1b) Naively copying the SLO label positions directly onto the OCT image fails to pair the labels with the visible cones, due to their relative image distortion. 2a) We first rigidly match labeled patches of the SLO image to get a rough alignment with the OCT image. 2b) Notice how many SLO labels fall in the gaps between the cones, making pairings unclear. 3a) The center of each patch is converted into a vertex in a flexible triangle mesh. This mesh defines a piecewise linear continuous warping of the labeled SLO image. The user adjusts this mesh interactively by adding, deleting, or moving vertexes of the mesh. Shown in cyan are the vertexes and triangle mesh after user adjustment. 3b) Each label now overlaps with its paired cone in the OCT image. However, notice how many of the labels are still not centered on the cone cells. This makes visual verification of the pairing unnecessarily difficult. 4a) To fix this, we automatically move each label to the center of its paired cone cell in the OCT image. This is done by attaching a new mesh vertex to each label and moving this vertex to the nearest cone center in the OCT image. Shown in cyan are the resulting vertexes and triangle mesh. 4b) Notice that every label is now centered with each cone. 5a+b) The tool outputs the final SLO labels aligned to the OCT image, along with the warped SLO image. The user can now visually verify the pairing by checking cone-alignment between the warped SLO labels and the destination OCT image.

To compare outcomes of the two classification methods, we were first required to identify matching cones between the datasets obtained in AOSLO densitometry and AO-OCT based ORG. However, the two datasets obtained from these different instruments feature significantly different scales, orientations, cone appearances and motion-induced distortions. To address this problem, we used a specially designed Retina Map Alignment Tool. This tool aligns two cone-labeled retina images ('retina maps') via two-stages: automatic coarse image registration followed by human-assisted refinement and verification. This tool allows us to match hundreds to thousands of cones per subject with confidence in a fraction of the time it would take manually. See Figure 3 for a detailed step-by-step overview of this pipeline with accompanying visualizations. The remainder of this subsection provides additional technical detail of the tool's implementation.

The automatic stage of the Retina Map Alignment Tool finds a piecewise linear warping between the SLO image and the OCT *en face* image at the COST [29]. First, we find a rough translation, rotation, and scale between the

images via the method by Reddy and Chatterji [30]. Then, the SLO image is split into 0.1° wide patches and separately matched against the OCT image via normalized cross-correlation[31] . Finally, Random sample consensus (RANSAC) is used to filter outlier matches [32]. The center of each patch gives a rough correspondence point between the two images. To obtain a continuous warping, a triangle mesh is constructed with a vertex at each correspondence point. The tool then computes per-triangle transforms and applies texture mapping techniques to warp the SLO image onto the OCT image.

The human-assisted stage enables the user to adjust the image warp interactively, and visually verify the accuracy of the final cone matches. The user inspects the initial image warp alignment by flipping between the two registered images and checking that each cone visually aligns with its match. If further adjustment is needed, the tool allows the user to add, delete, or move correspondence points and see the updated warp in real time through the tool's graphical user interface. Once the user verifies SLO image warp, cone matches are identified by pairing each cone with its nearest neighbor across the images. Individual matches can also be manually adjusted. Finally, the tool outputs a file with the cone coordinates and identities relative to the new image.

The human assisted stage was conducted by two graders. Cone matches that agreed between the graders were included in analysis. Disagreement primarily occurred at the edges of the regions-of-interest, where there is less information to ascertain the match. Some cones matched were clearly visualized in one image but aligned to a dark or abnormally reflective cone in the corresponding image and surrounded by clearly matched cones. These cones were dubbed "dysflective cones" (see section 3.3 below), and likewise agreed upon between the graders. Overall, the disagreement between the graders led to the exclusion of 12 of 854 cones for subject 4 and 2 of 567 cones for subject 5 from the analysis.

3. Results

3.1 Complex average vs Angle average

In this section, we compare the two methods of averaging – complex and angle average – across repeat measurements. Fig. 4(a) shows an example of a cone where the individual trial ORG traces have low inter-trial variability, low noise and no unwrapping artifacts. In this case, the angle average and the complex average traces align well with each other. Fig. 4(b) shows an example of a cone where repeat measurements are noisy and have unwrapping artifacts. These factors corrupt the angle average trace, and in this specific case, lead to a lower overall ΔOPL change compared to the complex average. This comparison was repeated for the same population of cones (n = 512) in Figs. 4(c) and 4(d), where there is expected to be a mixture of cones with high and low inter-trial variability. The complex average of the constituent trials shows a clear separation between the three cone types in Fig. 4(c). In comparison, the angle average contains more noise in the individual cone ΔOPL versus time traces leading to an ambiguity in the cone assignments. We follow the complex average for all data presented in this article. Phase variance is directly related to the inverse of signal-to-noise – higher the SNR, lower the phase noise and vice versa.

The complex average effectively weights the phase information with the signal amplitude and is more robust to noise artifacts including phase wrapping.

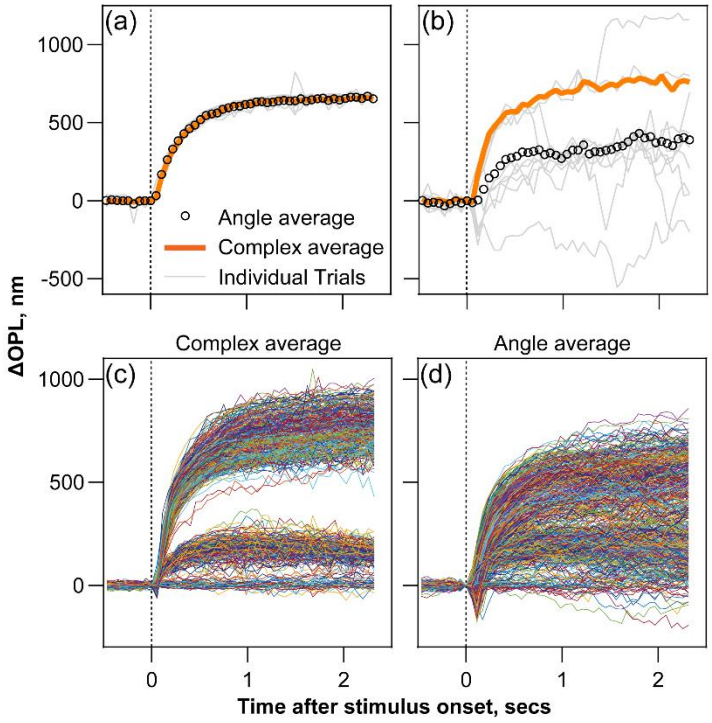

Figure 4: Comparison between complex and angle average for calculating the mean ΔOPL vs. time. Fig. 4(a) and 4(b) show examples for 10 repeat trials for 2 different cones in cases where the individual trials have low (a) and high (b) inter-trial variability respectively. When the two approaches are applied to a population of the same 512 cones, the complex average (Fig. 4(c)) readily segregates the cones into its respective spectral types. Angle average (Fig. 4(d)), on the other hand, is more susceptible to inter-trial variability and leads to ambiguity in the cone assignments.

3.2 Separating LMS cones

Figure 5 shows a representative example of the procedure for cone classification under a 660 nm stimulus bleach at 1.5°. temporal eccentricity in subject S4. The three cone types are well segregated owing to the variable bleach in each type. The absolute values of the registered AO-OCT complex volume segmented at the ISOS and COST ($I_{ISOS}(x,y)$ and $I_{COST}(x,y)$) provides *en face* images revealing cone photoreceptors at the two layers (Figs. 5(a) and 5(b)). The mean ΔOPL between the ISOS and COST at time t = 0.58 sec after stimulus onset is shown in Fig. 5(c) for each cone (see Video 1 for time evolution of ΔOPL in individual cones). The magnitude of ΔOPL for each cone in the image is color coded according to the color bar, and shows the variability and distribution between cones. Three colors – red, yellow and blue on the color bar are dominant while the intervening colors are sparse, suggesting the correspondence to the three cone types. The time series of ΔOPL for individual cones is shown in Fig. 5(d). The maximum ΔOPL for every cone is plotted as a histogram in Fig. 5(e). The maximum ΔOPL for each cone was obtained after complex averaging the repeat trials. The histogram is separated into the corresponding clusters of L, M and S cones by the intersection of the three component Gaussians. The individual cone ΔOPL traces are shaded red, green

and blue in Fig. 5(f) according to their cluster assignment in Fig. 5(e). The mean of the maximum ΔOPL for LMS-cones was 585±5, 157±20, 9±18 nm respectively. After clustering assignment, cones that have noisy ΔOPL traces and wrapping artifacts are filtered manually by comparing their mean ΔOPL trace across all repeats, to the mean of all cones within that cluster. Within the filtered cones, individual repeat trials with excess eye movements or noise are removed, and the complex average is re-computed with the remaining trials. After these steps, the cones that exhibit normal ORG characteristics, as defined by the mean of the three clusters, are included in the final analysis. The remaining are flagged as having insufficient fidelity to unambiguously assign their type. These cones are excluded from the classification and labeled as 'not classified (NC)'. The number of NC cones is marked in Table 1.

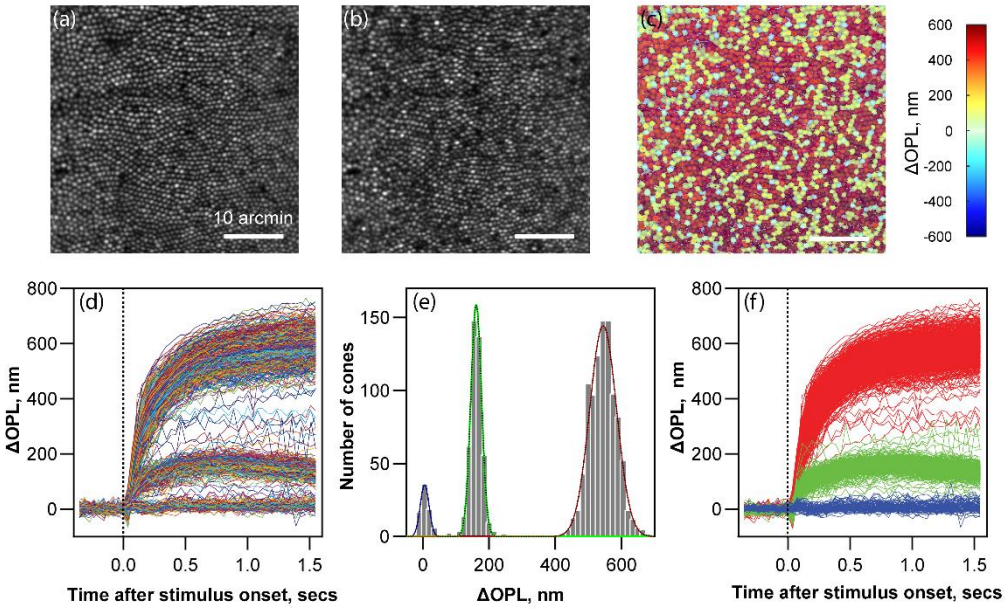

Figure 5: Representative example for cone classification for Subject S4. Registered AO-OCT volumes segmented at ISOS and COST yields the *en face* cone photoreceptor images at these layers in (a) and (b) respectively. The mean ΔOPL of seven recordings in cone outer segments at time t=0.5 is color coded according to the color bar in (c) and overlaid on the cone mosaic in the COST image. Individual cone time series of ΔOPL for all the cones identified in the AO-OCT structural image is plotted in Fig. 5(d). A histogram of the maximum ΔOPL averaged over the time after stimulus onset between 0.7 – 1 sec is shown in Fig. 5e. Gaussian mixture model clustering analysis is used to segregate the cone types based on the maximum ΔOPL in the histogram. Fig. 5(f) shows the same traces from Fig. 5(d), now color coded as red, green and blue to represent LMS-cones respectively. Scale bar: 10 arcmin

Figure 6 shows the cone classification for three subjects (S1, S2, and S3, from left to right columns) following the procedure in Fig. 5. The x,y cone locations in arc-min, and spectral types are provided in Data File 1[33]. Figs. 6 (a,b,c) shows the gray scale image and (d,e,f) shows the histogram of ΔOPL and cluster separations into the three cone types. Figs. 6 (g,h,i) shows the corresponding LMS-cone mosaics labeled in false-color according to their segregation obtained from Gaussian mixture model clustering analysis. Table 1 shows the total number of cones classified, percentage of S-cones, L:M ratio, the variation of saturated ΔOPL in each cone subtype, the probability and error of

assignment for the 3 subjects. The remaining two subjects appear below in section 3.5. The average maximum ΔOPL between all 5 subjects (3 subjects from Table 1 and 2 subjects form table 2) for L, M, S-cones was 648±67, 170±28, 15±15 nm respectively. In the 5 color normal subjects, the L:M cone ratio ranged between 1.5 - 2.4, and S-cone percent between 4.8 – 8.4 %, and both are comparable to the literature [9, 34].

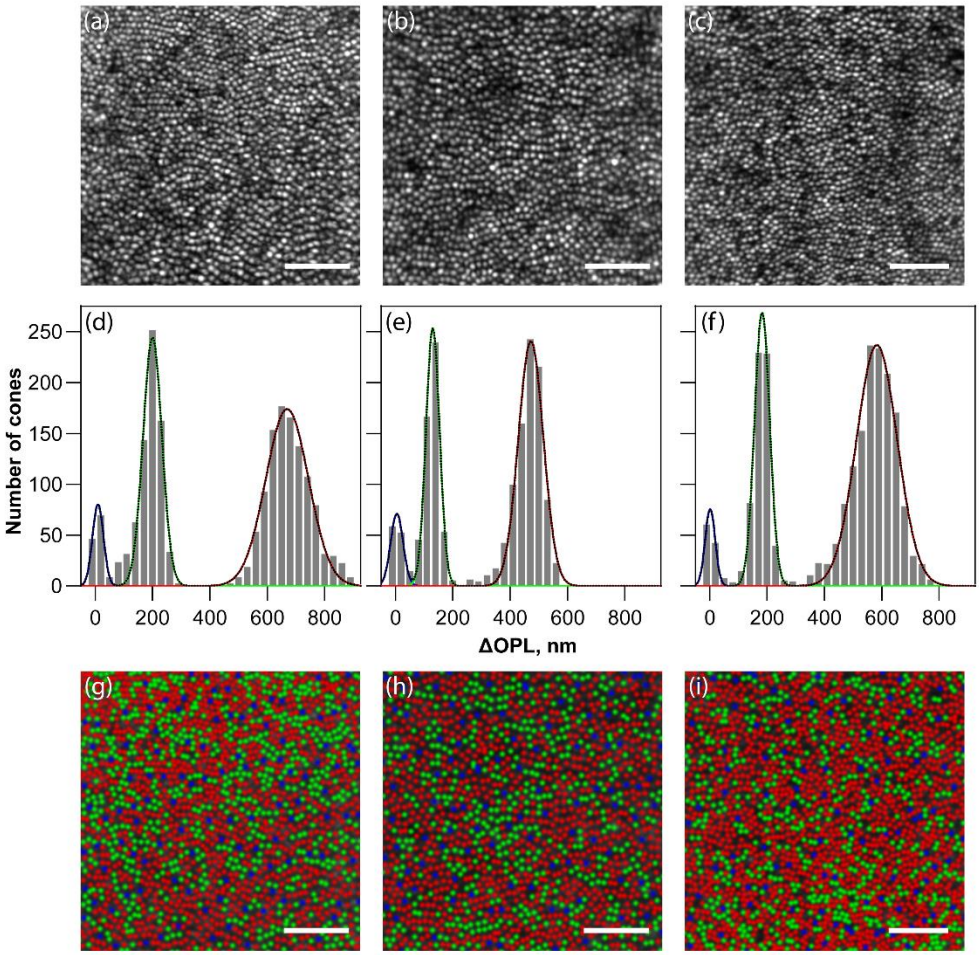

Figure 6: Cone spectral classification in three color normal subjects using ORG. Subjects S1, S2 and S3 are shown from left to right columns. (a-c) Gray scale *en face* images obtained by segmenting the registered and averaged AO-OCT volume at the COST (d-f) Histograms of maximum ΔOPL calculated in the time window 0.7 – 1 sec after stimulus onset overlaid with the component Gaussian fits obtained from Gaussian mixture model clustering analysis. (g-i) LMS-cone mosaics false-colored as red, green and blue to represent the three cone types. Scale bar: 10 arcmin

Table 1. Cone Classification Summary for 3 color normal subjects at 1.5°. eccentricity

Subject /Age /Ethnicity	# Cones	# Cones (NC)	L:M ratio	%S	Average Max ΔOPL (nm) (Mean ± Std)			Probability (Mean ± Std)	%SM error	%ML error
					L-cones	M-cones	S-cones			

S1/30/C	1945	4	1.5	6.6%	746 ± 92	187 ± 41	19 ± 21	0.99±0.04	0.01	5e-4
S2/44/A	1556	1	1.7	7.3%	559 ± 55	130 ± 28	18 ± 11	0.99±0.02	0.22	2e-5
S3/25/C	2173	3	2.4	5.3%	620 ± 79	177 ± 30	11 ± 15	0.99±0.03	2e-3	2e-3
NC - Not Classified										

3.3 Dysflective cones

Cone photoreceptor reflections are variable, potentially due to a combination of interference of multiple reflections from the outer segment, disc shedding and renewal, abnormal waveguiding and perhaps other unknown factors [7, 8, 20, 21, 35, 36]. In addition, it is also known that a visible stimulus causes reflectivity variations that can be analyzed to infer their function, also termed intensity ORG, or iORG [37-39]. Support that these variations are caused due to interference from multiple reflections from the outer segment comes from Cooper et al.2020 [38]. They used a long coherence light source greater than the length of the outer segment that reduced the variability in cone reflectivity considerably. In the extreme case, some cones have abnormally low reflectivity, dubbed 'dysflective' [40, 41]. It has been noted that normal eyes with no known disease have patches of dysflective cones that sometimes regain their reflectivity over time [42]. Also, using retinal tracking and targeted stimulus delivery, it has been shown cones with low reflectivity exhibit normal perceptual sensitivity [43]. In this section, we sought to investigate whether any potential functional deficit in ORG can be observed in dysflective cones.

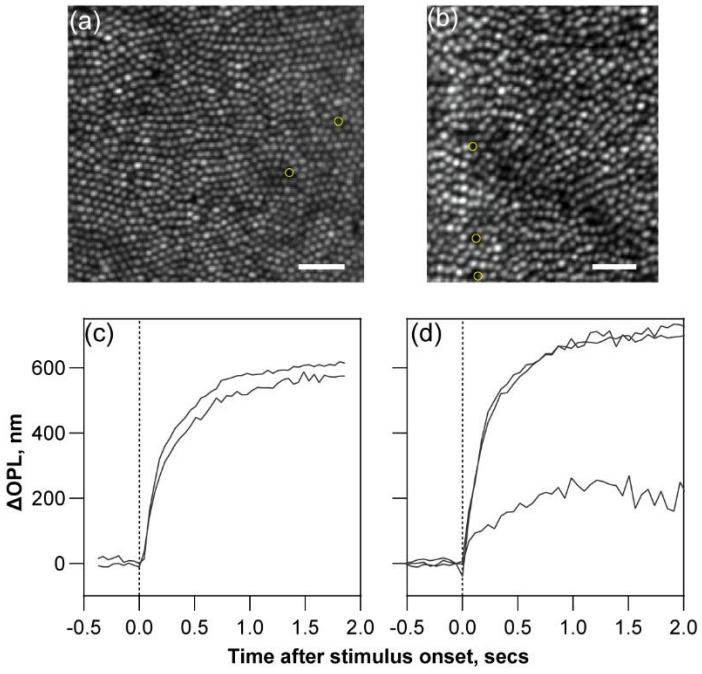

Figure 7: Optoretinography in dysflective cones. Fig. 7(a) and (b) show AO-OCT grayscale images for subject S4 (a) and S5 (b) at the COST layer where yellow circles indicate cones whose reflections were very low or absent. That cones were present in these 'dark' spaces was confirmed by finding their locations in the corresponding AOSLO image in the same subjects using the 'Retinal Map Alignment Tool' (see section 2.8). Dark shadow in 7b represents blood vessels overlying the cones. Fig. 7(c) and d show the corresponding ΔOPL vs. time traces showing normal characteristics consistent with their classification into L-cones (Fig. 7(c)) and LM-cones (Fig. 7(d)). Scale bar: 5 arc-min.

Image formation in OCT relies on optical interference, and it may be plausible that reflections from some cones undergo destructive interference to exhibit abnormally low reflections. In the AOSLO, cones lying under the shadows of blood vessels have lower apparent reflectivity, especially when imaged with a visible wavelength as in retinal densitometry. Examples of dysflective cones are shown in Fig. 7 in subject S4 (a) and S5 (b) in their respective AO-OCT *en face* images of the COST. With AO-OCT alone, it was not possible to ascertain whether cones were indeed present in these dark areas indicated by the yellow circles. However, with the 'Retina Map Alignment Tool' described in section 2.8, we observed cone reflections present in the corresponding AOSLO image from the same subjects at these locations (S4: n=2 cones, S5: n=3). Fig. 7(c) and 7(d) show the ΔOPL versus time for the dysflective cones indicated in Fig. 7(a) and 7(b) after a 660 nm stimulus bleach. For these dysflective cones, the phase difference was calculated at the same axial locations as where ISOS or COST would have been had there been a reflection from them. This axial location was determined based on the neighboring cones' reflections. This approach assumes that the axial reflection locations don't change substantially in a local area. These traces indicate normal ORG characteristics consistent with their classification into either L-cones or M-cones, based on their high and low maximum ΔOPL respectively. This indicates that, in addition to having normal perceptual sensitivity, dysflective cones exhibit normal functional responses in the ORG and transduce light with similar efficacy as cones with normal reflectivity.

3.4 Test-retest reliability in ORG cone classification

Figure 8 evaluates the test-retest reliability of classification across two different days. Figs. 8(a) and (c) show the maximum ΔOPL across the two days, labeled 'day 1' and 'day 2', at 1.5°. and 4°. eccentricity in Subjects S4 and S2 respectively. The cones were unambiguously selected on the images at 4 deg. eccentricity without intrusion from rods (thanks to the OCT axial resolution) for the ORG measurements. The maximum ΔOPLs obtained in each cone for the two days are plotted against one another; each data point represents an individual cone. Three distinct clusters with increasing maximum ΔOPL are observable corresponding to the LMS-cones. Cones were classified with high fidelity using Gaussian mixture model analysis based on each day's measurements alone, with errors less than 0.02% and mean probability of 0.99. The distribution of data points in both x and y dimensions represents the variability in ΔOPL for each day, increasing in magnitude with the maximum ΔOPL. A few data points in each case lie outside the clusters and beyond the equality line. These correspond to the cones that did not match across days in their magnitude of maximum ΔOPL. Phase wrapping errors that lead to 2π phase ambiguities can partly explain these mismatches where a few cones exhibit high maximum ΔOPL on one day and low on the other. The mean Euclidean distance from the origin for the mismatched cones was 340 nm; in comparison, for the OCT center wavelength of 820 nm, a 2π ambiguity would result in a 410 nm error in ΔOPL.

To analyze the agreement in maximum ΔOPL as a whole between days, Figs. 8(b) and (d) show a Bland-Altman plot for 1.5°. and 4°. eccentricity respectively. Each data point is the measurement from the same cone across days. The

three clusters corresponding to the cone types and the greater magnitudes of variability with increasing maximum ΔOPL are also observed in these plots (also see the standard deviation for S, M and L-cones in Tables 1 and 2). Typically, Bland-Altman plots represent the relationship between the difference (y-axis) versus the mean (x-axis) of two measurements to gauge their agreement. At 1.5° and 4°. eccentricity, 65 out of a total of 1397 cones and 13 out of a total of 305 cones lie beyond the ±95% confidence interval (orange line) respectively. The bias (black line), equal to the mean difference across all cones for both days, is meant to indicate any potential systematic difference between the days. The values of bias were 8.06 and 2.45 nm for 1.5° and 4°. respectively, and is close to the noise floor of the measurement for the ORG paradigm in the line-scan OCT [16]. At 1.5°. eccentricity, of the 1397 cones classified across both days based on Gaussian mixture model analysis on maximum ΔOPL, 4.2 % (59 cones – 48 L/M, 9 L/S, 2 M/S) were inconsistent in their assignment between the days. At 4°. eccentricity, 305 cones were classified across both days, of which 2.6% (8 cones – 3 L/M, 0 L/S, 5 M/S) were inconsistent in their assignment between days. Overall, a high agreement was noted between assignments across different days. The slightly larger inconsistency at 1.5°. could be related to phase wrapping errors. It is likely these were not sufficiently eliminated due to inadequate repeat measurements - 6 repeats on day 1 and 5 repeats on day 2 at 1.5°. - compared to the 10 repeats on each day at 4°. Subject S4 has good fixation and typically has a lower probability of individual trial rejection due to large eye movements; hence we recorded 6 and 5 repeats on day 1 and day 2. No repeat trials were removed from analysis. Another potential reason could be the higher cone density and smaller cone sizes at the closer eccentricity that may pose greater noise in the measurements across days.

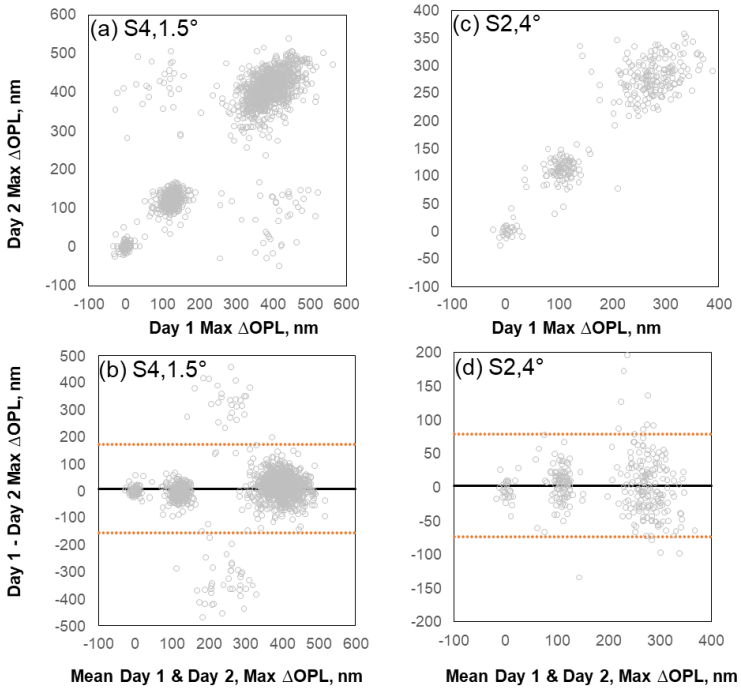

Figure 8: Comparison of maximum ΔOPL across two days, labeled day 1 and day 2, in the same cones. Fig. 8(a,b) and (c,d) show data at 1.5° and 4°. eccentricity for S4 and S2 respectively. Note the different y-axis scale at the two eccentricities.

In a) and c), the magnitude of maximum ΔOPL for days 1 and 2 is plotted against each other, b) and d) show Bland-Altman plots for difference vs. mean of the maximum ΔOPL across the days. Horizontal orange line indicates ±95% confidence intervals in the difference between days, and the horizontal black line indicates the mean difference or bias.

3.5 Densitometry vs ORG classification comparison

We observed high classification agreement using densitometry and ORG ~6-7 years apart in Subjects S4 and S5 in Figs. 9 and 10 (S4: 771/842 cones, 91.6%; S5: 511/565 cones, 90.4%). Fig. 9 shows the false-color LMS-cone mosaics from S4 and S5, classified at the same retinal eccentricity in densitometry and ORG. The x,y cone locations in arc-min, and spectral types obtained via ORG an densitometry are provided in Data File 1[33] for both subjects. After cone matching and visual inspection by 2 separate graders, a few cones (S4: 12; S5: 4) present in Fig. 9 were misaligned to a degree not amenable for comparison, and these were removed from further comparative analysis. Regions classified with ORG fully encapsulated regions classified with densitometry, and all cones classified with densitometry (S4: n=830, S5: n=559) were classified with ORG. If the comparison were restricted only to cones that were successfully classified in densitometry, the proportion agreement in S4 and S5 was 92.9% (771/830 cones) and 91.4 % (511/559).

A small number of cones were not visible in the AO-OCT image (dubbed dysflective cones as section 3.3 above), but were nonetheless classified thanks to their transferred location from the densitometry image (see 'Retina Map Alignment Tool' in section 2.8 and Fig. 7) (S4: n=2, S5: n=3). Finally, several cones which were not classified (NC) with densitometry owing to low reflections, in part caused by their lying under shadows of blood vessels, were classified with ORG (S4: n=12, S5: n=6).

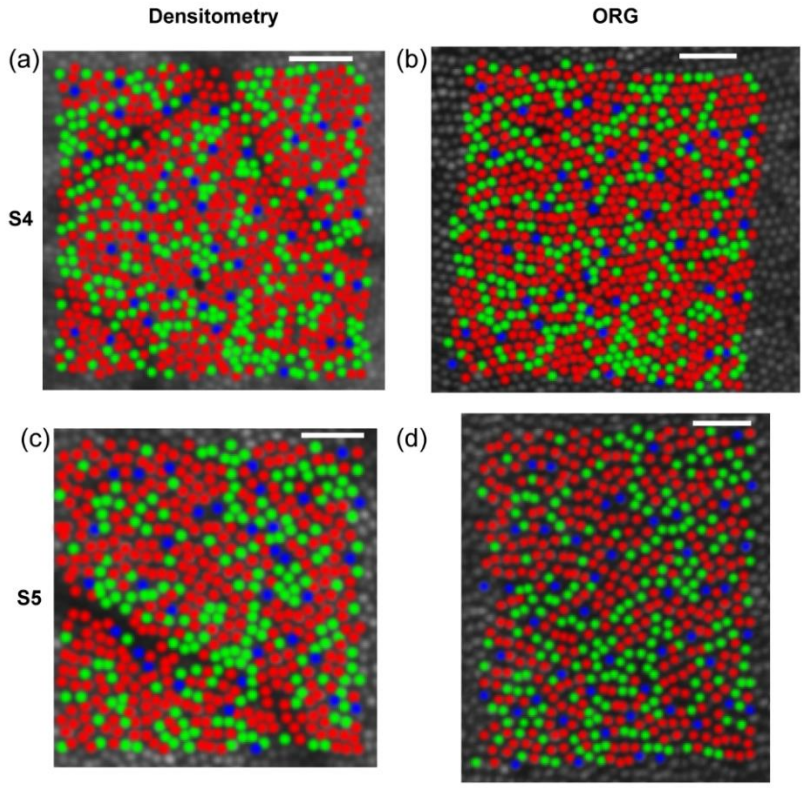

Figure 9: Cone spectral classification with densitometry and ORG. Fig. 9(a) and b show the cone spectral assignments in false color in S4 for densitometry and ORG, respectively overlaid on a grayscale image. Fig. 9(c) and d show the same for S5. Scale bar: 5 arc-min.

A cone-by-cone summary of classification agreement across the two paradigms is summarized in Figs. 10 (a-d). Figs. 10(a) and (b) shows the distribution of cones across the regions of interest and how their cone assignment is consistent or different between the two modalities in S4 and S5. The background cone assignments are obtained from the ORG. Comparing the assignments as a whole in this manner helps appreciate potential factors related to the spatial arrangement or specific cone-types that may lead to inconsistencies. For example, it has been suggested that optical blur in densitometry might lead to an error in classification where cones of like-type are clumped together [4, 9]. Visual inspection shows few examples in both subjects where patches of 3-6 contiguous cones are mismatched. Two additional features are worth noting. Cones lying near the edge of the region-of-interest have a higher likelihood for mismatch than the center. One potential reason for this is eye motion that reduces the number of samples averaged at the borders compared to the center. Second, the bottom left quadrant of the region-of-interest in subject S5 has higher degree of mismatch, a location that has blood vessels overlying the cones casting a shadow, as shown in the gray scale image in Fig. 7(b). This causes decreased back reflectivity of cones lying in the shadow, increased absorption by the blood vessels for the bleaching light and increased forward and backward scatter of the imaging light in both modalities.

Confusion matrices in Figs. 10(c) and 10(d) summarize the mismatch by cone type in both modalities. In both subjects, classification agreement (relative to ORG assignment) was highest for L-cones (S4: 92%, S5: 97%), decreasing for M-cones (S4: 90%, S5: 88%) and S-cones (S4: 93%, S5=59%). Table 2 summarizes the classification agreement, L:M ratio and % S-cones measured from each method. Mismatches had a slight effect on the L:M ratio measured for both

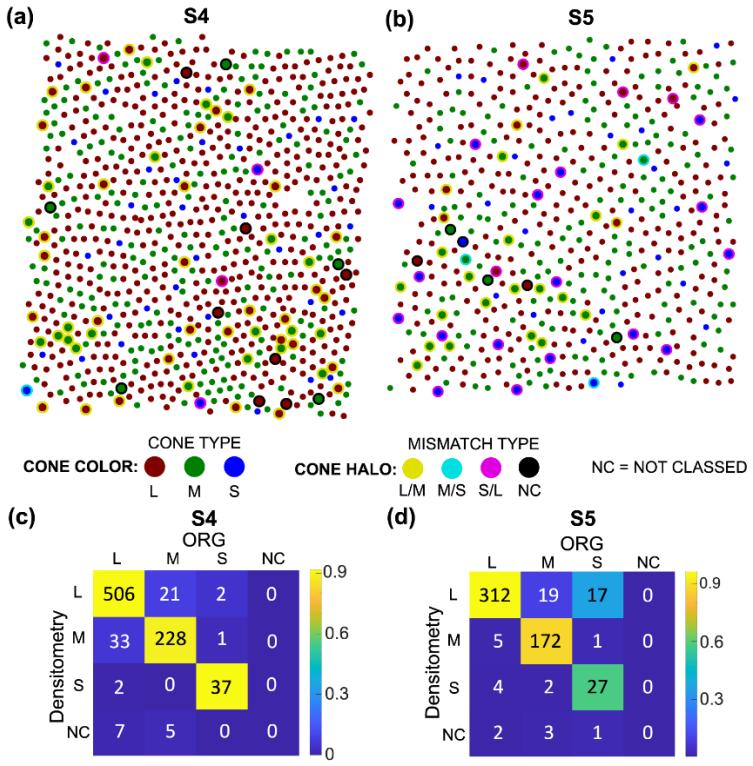

Figure 10: Classification mismatch between densitometry and ORG. Fig. 10(a) and (b) show ORG-classified mosaics highlighting densitometry-mismatches. Cone color indicates ORG LMS-classification. Cones with mismatched classification are plotted larger with a halo that indicates their densitometry classification. Fig. 10(c) and (d) show classification confusion matrices which quantify the number of cone-type specific matches in ORG and densitometry. Colors of each square and the corresponding color bars indicate the proportion matched between both modalities. Figs. 10(a,c) are S4 classification mismatch and confusion matrix. Figs 10(b,d) are S5 classification mismatch and confusion matrix.

Table 2: Summary of comparison between densitometry and ORG for cone classification

Subject /Age /Ethnicity	# Cones compared	# Mismatch class	% Agreement	Method	L:M ratio	%S	Average Max ΔOPL (nm)		
							L-cones	M-cones	S-cones
S4/38/A	842	71	91.6	Densitometry	2	4.6	585±52	157±20	9±18
				ORG	2.2	4.8			
S5/38/C	565	54	90.4	Densitometry	2	5.8	728±57	198±23	20±11

				ORG	1.6	8.1			

subjects (S4: 2.0 vs 2.2, S5: 2.0 vs 1.6), negligible effect on the percent S-cones measured for Subject S4 (4.6 v 4.8%), and a more substantial effect on percent S-cones measured for Subject S5 (5.8 vs. 8.1%). For Subject S4, classification mismatches were dominated by L/M mismatches (of 71 mismatches, L/M = 76.1%, S/(LM) = 7.0%, NC = 16.9%), whereas a higher proportion of mismatches for subject S5 involve S-cones (of 54 mismatches, L/M = 44.4%, S/(LM) = 44.4%, NC = 11.1%). In particular, for Subject S5, a disproportionate number of cones assigned S in ORG were assigned L with densitometry (17/54 mismatches). Of these 17 L vs. S-cone mismatches, 5 occur at the borders of the region-of-interest, and 7 occur in the area overshadowed by the blood vessel (bottom left quadrant of Fig. 10(b), corresponding AO-OCT structural image at COST layer with blood vessel shadow is shown in Fig. 7(d)).

4. Discussion

This article presents the optimization and characterization of cone spectral classification using ORG and its comparison against densitometry. The cone mosaic of five color normal subjects were classified with ORG, showing high probability (~0.99), low error (<0.22%), high test-retest reliability (~97%) and short imaging durations (< 1 hour). The values for error are comparable to those reported previously for cone classification with point-scan AO-OCT[13]. The L:M cone ratio, and percent S-cones measured in this cohort are consistent with literature [9, 34]. In comparison, slightly lower probability (~0.95) and higher error (~ 5%) was observed in densitometry for classifying cones [11].

Some caution is suggested in interpreting error rates and probability of cone assignments obtained from clustering analysis shown here and in previous reports. An approximate analogy could be made to the concepts of 'precision' and 'accuracy' in this regard. The error rates and probabilities as derived from the clustering analyses are very useful in indicating the precision by which the segregation of cone types can be obtained by a particular technique, when the task is faced with variability related to biological and methodological factors. However, accuracy, loosely defined in the current perspective, relates to how closely the cone types so-obtained relate to the "ground truth". When the ground truth is unknown as is the case here, repeat measurements are carried out to assess the degree to which the results remain resilient amidst the myriad sources of variability. To this end, the test-retest analysis shown here evaluates the degree to which cone assignments remain uniform across days and can be considered the upper bound error estimate of the accuracy of classification. Such an analysis has not been reported for densitometry.

The laboratory time taken for ORG data collection ranges from 30-50 min per one region-of-interest. This includes the optimization of image focus in line-scan ophthalmoscope & OCT *en face* images (15-20 min) and 10 repeat measurements (15-30 min). This is significantly more efficient compared to densitometry that could take 3-9 hours of laboratory time per region-of-interest [11]. Further, it was suggested that the imaging sessions be distributed across a few days to account for reflectivity variations in cones, independent of photopigment absorption, leading generally to a greater time needed per subject [9]. Averaging is essential for both modalities given how ORG cone assignments can also be affected by phase wrapping errors when there are inadequate repeat

measurements. The data processing in MATLAB for ORG takes about 4-5 hours per subject where ~50% of this time is consumed for reading and writing the data between the solid-state hard drive and MATLAB workspace. This data processing time is not optimized, and it can be reduced drastically by using C++ with CUDA.

The overall higher fidelity of ORG is the result of greater than 20-fold higher dynamic range available in ORG compared to densitometry for capturing the perturbations caused by bleaching in the backscattered reflection from cones. Since the OCT layer reflections encasing the outer segment are used for computing the light-evoked ΔOPL, the optical signal is largely confined to the cone outer segment and not corrupted by reflections from other layers. Optical phase difference used to compute the ΔOPL has high sensitivity of about a few nanometers when phase is referenced between the ISOS and COST to remove common-mode noise. The bleach dependence of the ΔOPL is non-linear, scaling in magnitude with a gain greater than 1 suggesting a relationship to the amplification cascade of phototransduction [14]. The mechanism of the change in outer segment OPL has been attributed to the influx of water to maintain osmotic balance during phototransduction [19]. This is suggested to be in response to the disturbance of osmotic balance caused by the intermediary osmolytic products of the cascade that are amplified in their concentration compared to photopigments. While this multiplicative effect provides a gauge for photopigment concentration sufficient to classify cones with high fidelity in healthy eyes, the intermediary osmolytes are currently unknown. This unknown is critical to recognize when using ΔOPL as a biomarker for retinal diseases where mutations in specific proteins of phototransduction are implicated. In such cases, ΔOPL will not directly provide a gauge for photopigment concentration. On the other hand, the ORG early response, that manifests as a reduction in ΔOPL immediately after stimulus onset and occurs prior to the onset of the amplification cascade, can provide a direct measure of photopigment activation [14, 44]. A few examples of early response maximum amplitude have been observed (unpublished data) that vary in a manner consistent with their classification into the 3-cone types. But, the dynamic range from ~5 - 50 nm and the associated noise at these low OPL values are not sufficient to reliably differentiate the three cone types based on the early response alone. Furthermore, the early response peak amplitude occurs between 3 ms to 10 ms depending on bleach strength. To resolve this temporally, volume rates of at least 333 Hz would be required, corresponding to approximately 133k -200k B-scans/sec, in order to achieve the 400-600 B-scans per volume acquired here. Currently, this speed and SNR is beyond the reach of the instrument.

These aforementioned benefits of ORG do not apply to densitometry. Since absorption imaging is not depth-resolved to cone outer segments, it is confounded by the contribution of stray light due to scattering from other retinal layers, blood flow and anterior optics. With the confocality provided by AOSLO, the contribution of stray light can be reduced substantially. Still, maximum measurable change in absorption is limited to 0.41 log units (2.6-fold) at 550 nm [18]. Changes in optical intensity due to absorption cannot capitalize on the benefits of phototransduction amplification. The variations in cone reflectivity following a stimulus, as observable in iORG, have been used to separate S-cones [38] and can in principle be used to infer all three types.

Given that the mechanism of densitometry is well established and attributed directly to photopigment concentration, it was essential to compare the cone assignments obtained by the ORG method against it. A high

agreement (mean: 91%) was observed between the two modalities in 2 subjects, with measurements conducted 6-7 years apart. Cones lying in the shadows of blood vessels in AOSLO were likely to be inconsistent in their assignments. Contiguous clusters of 3-6 mismatched cones were observed, attributable to optical blur and scatter. A greater degree of mismatch in S-cones was observed, likely in part due to the fact that S-cones are identified by a lack of their response to the 660 nm stimulus in both modalities. Instead, a bleach that activates S-cones could be used in the future. Dysflective cones were found in both modalities. Cones dysflective in ORG were located in their counterpart image, and analyzed for their spectral type using ORG. Further work is needed to ascertain how the reflectivity in these cones changes with time across shorter timespans, i.e. repeat trials within a day, and longer timespans, i.e. different days. Also, it is of interest to gauge if or whether the ORG characteristics follow the changes in backscattered intensity. Such cones with abnormal reflections have been observed in healthy and diseased eyes [41, 42, 45]. They have previously been shown to have normal function also [43, 45]. That they exhibit normal functional responses in the ORG has important clinical implications. A preponderance of 'dark' or dysflective cones in pathological eyes may not provide the complete picture of the dysfunctional state, and a functional measure of phototransduction such as ORG may be a more sensitive biomarker.

In summary, the protocol for cone classification was characterized using ORG and compared against densitometry. The benefits obtained in ORG from its higher sensitivity and dynamic range led to high efficiency and fidelity for cone spectral classification.

Acknowledgement

Burroughs Wellcome Fund (Careers at the Scientific Interfaces Award); Research to Prevent Blindness (Career Development Award, Unrestriced grant to UW Ophthalmology); National Eye Institute R01EY029710, P30EY001730, U01EY032055); Weill NeuroHub Next Great Ideas Program; Air Force Office of Scientific Research (FA9550-20-1-0195 and FA9550-21-1-0230).

Disclosures

VPP and RS have a commercial interest in a US patent describing the technology for the line-scan OCT for optoretinography.

AR: USPTO #7,118,216, "Method and apparatus for using AO in a scanning laser ophthalmoscope" and USPTO #6,890,076, "Method and apparatus for using AO in a scanning laser ophthalmoscope". These patents are assigned to both the University of Rochester and the University of Houston and are currently licensed to Boston Micromachines Corporation in Cambridge, Massachusetts. Both AR and the company may benefit financially from the publication of this research.

Data Availability

Data underlying the results presented in this paper are available in Data File 1[33].

References

3: Characterization of the human S-exclusion Zone

3.1 Introduction

Prior work has shown S-mosaics (the subset of the cone mosaic that are S-type) to be significantly regular in mature human retinae at eccentricities greater than ~2° from the fovea, while slightly more central regions approaching 1° have been reported as randomly arranged [28,29,35,40,45,48,59]. The characteristic semi-regularity of S-mosaics strongly suggests the presence of an S-exclusion zone, a region surrounding S-cones where others are significantly unlikely to be found. Spatial point processes, primarily Density Recovery Profile (DRP)[60] have been used to characterize the radius of the S-cone exclusion zone. Regularity has then been measured as the squared ratio of that radius to the estimated maximum radius a grid of points of equal density to the S-mosaic. This is the paradigm by which a gradient from random to semi-regular and highly regular S-mosaics have been measured since the early 1990s, and the basis for our understanding of how the phenomenon varies across the retina and between species.

While density and proportion of S-cones have been documented at a fine grain across the central retina in humans, the S-exclusion zone and S-mosaic independence has been described for 1-3 regions of the central retina (usually 1) per individual, limiting our ability to understand how the feature varies across the retina. See Table 1.1 for detail on instances where the human S-exclusion zone has been described, as well as that of selected macaque reports. Human and macaque S-cone topography are studied in tandem and compared in numerous reports. Macaques are frequently relied upon as a model for human vision because of their similarity to us among the mammalian species frequently studied. Attention to differences between humans and macaques (and other species, for that matter) is critical for understanding limitations of the model system and to connect anatomical and physiological differences with visual function.

Not only is information about the S-exclusion zone too sparse in the human literature to say how it may or may not vary across the retina (besides the central irregularity), but all instances where these properties have been measured have been in ex-vivo immunohistochemical experiments. From these data, researchers were not able to relate S-cone topography to visual perception with in-vivo psychophysics.

In this report we describe the robust presence of an S-exclusion radius spanning the central ~1-12°radius in the macula of two human subjects across the four meridians, even between 1 and 2° where S sub-mosaics have been previously reported to be randomly arranged. We did so using a novel approach that relies on Voronoi Tessellations that we term Concentric Ring Analysis (CRA). The merits of CRA over previous methods are demonstrated in Chapter 4. This includes a detailed assessment of DRP's weaknesses when applied to the task of characterizing the S-exclusion zone, and how its presence may have been obscured in previous reports. Note that the foveola has eluded investigation due to the extremely high-resolution demand of imaging the

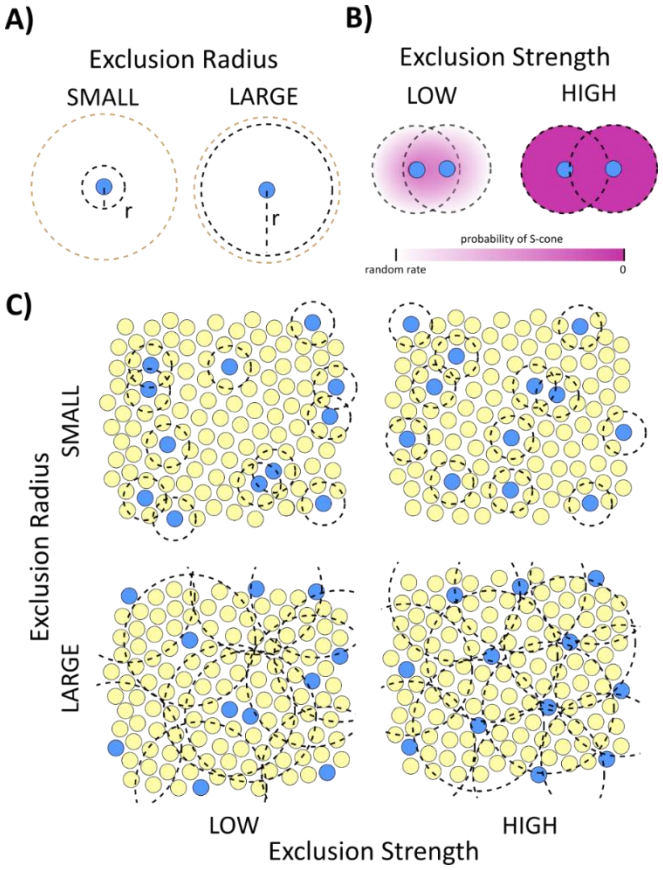

Figure 3.1 Characteristics of the S-exclusion zone that influence S-mosaic regularity. All graphics are cartoon examples, they do not represent our data. A) The Exclusion Radius (ExR) is defined as the radius surrounding S-cones where significantly few S-cones are found compared to simulated mosaics with random S-cone topography. The size of the exclusion radius influences S-mosaic regularity depending on its size relative to 1) the distance between cones and 2) the maximum radius possible given the density of S-cones. B) Exclusion Strength (ExS) is defined as the probability that S-cones are excluded within the Exclusion Radius. C) Cartoon examples of S-mosaics with S-exclusion zones varying in Exclusion Radius and Strength. With a small Exclusion Radius (top row), the regularity may not be visibly evident at all. The bottom row shows that with a high Exclusion Factor (a larger ExR), the S-mosaic is only driven to be highly regular if exclusion strength is also high.

tight packing of cones in this region of highest density.

The regularity of the S-mosaic is described with two metrics: its S-exclusion radius relative to the maximum radius possible, and the strength of the exclusion radius. These features of the S-exclusion co-influence the regularity of the final mosaic, but exclusion strength has not previously been reported. Figure 3.1 demonstrates the concept of the S-exclusion zone with cartoons. These examples show how the S-exclusion zone and S-mosaic regularity are shaped by properties of Exclusion Radius (ExR), Exclusion Factor (ExF, ratio of ExR to the maximum radius estimate), and Exclusion Strength (ExS). Cartoon mosaics with varying ExF and ExS are drawn to make an important point: An S-mosaic is only driven to be highly regular if both the ExF and ExS are high. Either property being low leads to a less regular S-mosaic.

Our analysis includes the observed S-mosaics of classified ROIS, as well as simulated ones that were either randomly arranged or maximally spaced within the cone mosaic. While use of random arrangements of cones are commonplace in the S-cone topography literature, this is the first instance of a maximally regular mosaics constrained by observed cone locations obtained from the same retinal image ROI. The paradigm allowed us to assess how regular S-mosaics are within the full range possible given the underlying geometry of the cone mosaic, which varies drastically across our ROIs.

S- cones were significantly few within the first two rings of cones surrounding S-cones in 20/24 ROIs from our two subjects, and within the first ring in 3/24 ROIs. This pattern of a 2-ring S-exclusion zone leads its radius to increase directly with the distance between neighboring cones. The latter varies across the retina depending the local density of rods and cones. We reanalyzed a subset of one macaque and one human ROI from Roorda et al 2001, and found the same pattern.

The S-exclusion radius for observed mosaics is ⅔ that of spaced mosaics for most ROIs, where the spaced S-mosaics have a 3-ring S-exclusion zone. Where S-cone proportion is lowest, the spaced ExR is highest and the observed radius is ½ its size. Where S-cone proportion is highest, the observed and spaced S-cone mosaic is the same. The strength of the S-exclusion zone is found to decrease slightly as the regularity in terms of its radius increases.

Finally, we found a characteristic anisotropy to the S-exclusion zone by visual inspection in autocorrelograms generated from S-mosaics with relatively high S-cones, including the central-most ROIs and the macaque ROI of Roorda et al 2001. This pattern is such that the S-exclusion zone is oblong

along the meridian of the ROI – that is, longer in the horizontal direction for ROIs nasal and temporal to the fovea, and vertical for superior and inferior ROIs. This cannot be characterized with current methods, which are all best suited to capturing radially symmetric patterns. Proposed augmentation to CRA measure this anisotropy is discussed.

These results reveal new patterns to our understanding of human S-cone topography and inspire compelling trajectories for topography analysis and comparative studies going forward.

3.2 Methods

3.2.1 Cone Classification

Cones were spectrally classified using optoretinography (ORG), described previously [Pandiyan et al 2021, Pandiyan et al 2022]. Briefly, the paradigm of ORG in cone photoreceptors entails measuring the optical path length change in the outer segment elicited by a light stimulus. Unlike absorption imaging via densitometry, the optical path length measure scales with the amount of pigment bleached in a non-linear manner with high gain. This is due to its relationship with the amplified products of phototransduction.

Here, we used a custom-built Adaptive Optics Optical Coherence Tomography (AO-OCT) instrument for ORG. This system provides high resolution and sensitivity for imaging cellular structures like foveal cones, rods and retinal ganglion cells [Pandiyan 2021]. By selecting a stimulus wavelength of 660 ± 5 nm where the cone types have sufficiently different spectral sensitivity, their spectral types can be readily segregated with high sensitivity and precision based on their differential bleaching signatures in ORG. The characterization of this method for cone spectral classification is described in Pandiyan et al 2022.

3.2.2 Subjects

Two color normal subjects (S1: Asian male, 38yo; S2: White female, age 27 yo) were recruited for the study after an informed consent explaining the nature and possible consequences of the study. The research was approved by the University of Washington institutional review board, and experiments were performed in accordance with the tenets of the Declaration of Helsinki. In each subject, cone spectral classification was performed for three regions-of-interest (ROI) along the four cardinal meridians - superior, temporal, inferior, and nasal. The ROIs were then aligned to a confocal scanning laser ophthalmoscope image to determine their precise retinal eccentricity. The S1 1.5° Temporal ROI

appeared as S3 in Sabesan et al 2015 and as S2 in Pandiyan et al 2022. The S2 1.5° Temporal ROI appeared as S3 in Pandiyan et al 2022.

We also re-analyzed data of two ROIs from Roorda et al 2001 that are publicly available, one human (JWT) and one macaque (M5), at 1° and 1.4° temporal. We cropped these ROIs to the largest rectangular area possible for compatibility with our analysis pipeline. Cropped, the JWT ROI contained 592 cones (27 S-type) and the M5 ROI contained 756 cones (65 S-type) (see Figure 3.10 A)

3.2.3 Simulated S-mosaics

In order to evaluate the observed S-cone topography in the context of random and maximally-regular extremes, random simulations of each were created for each ROI with simulations of each extreme. For every classified ROI, 1000 each of random and spaced sub-mosaics were generated. Each set of an observed S sub-mosaic and its simulated counterparts referred to as a mosaic-set (Fig 2A). All simulated mosaics of a mosaic-set were generated within the same rectangular area and cone positions as the observed ROI. Random sub-mosaics have the same number of S-cones as measured, while the number of cones in spaced sub-mosaics can vary slightly around this number (see Supplement). Separately, a population of fully random point distributions is also generated for each ROI that provides a basis for quantifying differences in test sub-mosaics from a uniform-random distribution in 2PC analysis.

3.2.3.1 Random S-mosaic

Random sub-mosaics were generated to represent the spatial statistics we would expect to measure if a sub-mosaic of cones were randomly arranged in the mosaic. This subset was generated according to the previously described Monte Carlo method.[61] S-cone identity was assigned at random iteratively, without replacement, to *x* cones among the total number of cones in the ROI, where *x* is the number of S-cones in the measured sub-mosaic. (Fig 2A, left)

3.2.3.2 Spaced S-mosaic

Spaced sub-mosaics were generated to represent the spatial characteristics of S-cones in the case when they are maximally spaced from one another. These mosaics were created by masking perfect hexagonal grids onto the native cone mosaic. The resultant mosaics represent the upper bound of S-cone sub-mosaic regularity for a given ROI. The mean spacing of the 1000 grids used provided an empirically derived estimate of the maximum possible S-cone spacing, referred to later as “empirical maximum radius”, or eMR. See the supplement for specifics on the algorithm to generate Spaced mosaics.

3.2.4 Assessment of S-cone Topography

3.2.4.1 All-cone Voronoi Tessellation (AVT)

Voronoi tessellations were constructed from the (x, y) coordinates of all cones identified in an ROI. For every Voronoi cell representing a cone, neighboring cells were identified as those sharing cell edges. Inter-cone-neighbor distances were calculated between every bound cone's center and that of its Voronoi-cell neighbors. Unbound cells are those near the ROI boundary that have one or more edges not shared with another cell. The mean inter-neighbor distance for all cones of an ROI provided the value μINDa. This value was critical to compare exclusion zone properties with eccentricity because cone density varies dramatically across the central retina. The "All-cone" of All-cone Voronoi Tessellation (AVT) distinguishes it from the S-cone Voronoi Tessellation (SVT), which is also relevant to S-cone topography analysis and discussed in Chapter 4.

3.2.4.2 Concentric Ring Analysis (CRA)

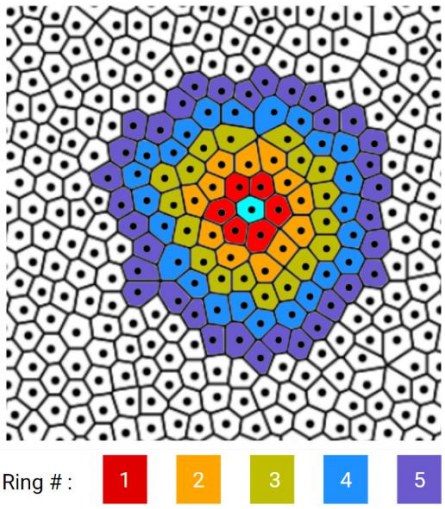

Figure 3.2. Example of concentric rings in a Voronoi Tessellation. A mosaic of Voronoi cells (black lines) is generated from the coordinates of observed cone locations (black dots). 5 rings of cones are identified surrounding a single cone, shown in aqua.

Concentric Ring Analysis (CRA) is computed from the AVT of the cone-mosaic, and the subsets of cones in that mosaic making up the test S-mosaic (observed or spaced in our case) and 1000 random S-mosaics. We computed the number of cones and number of S-cones per each of the first 5 rings surrounding S-cones in each test mosaic to be compared against that of 1000 random S-mosaics. Distributions of the number and proportion of S-cones were compared between test and random S-mosaics using left and right tailed Mann Whitney U-tests for each ring. This was the appropriate statistic due to it being

nonparametric, non-paired, and robust to large differences in observations per sample. A left tailed test where $p < 0.05$ indicates that the prevalence of S-cones is significantly lower in that ring than for random-mosaics, while a right-tailed $p < 0.05$ indicates significantly high S-cone prevalence. If the test mosaic is significantly low in the first ring, there is an S-exclusion zone that extends as many consecutively low-S-cone rings there are from the first. We call this an Exclusion Radius in rings (ExRr), as opposed to Exclusion Radius in arc-min (ExRa). From the ExRr, the ExRa is calculated as the distribution of cone distances making up the outermost ring of the S-exclusion zone.

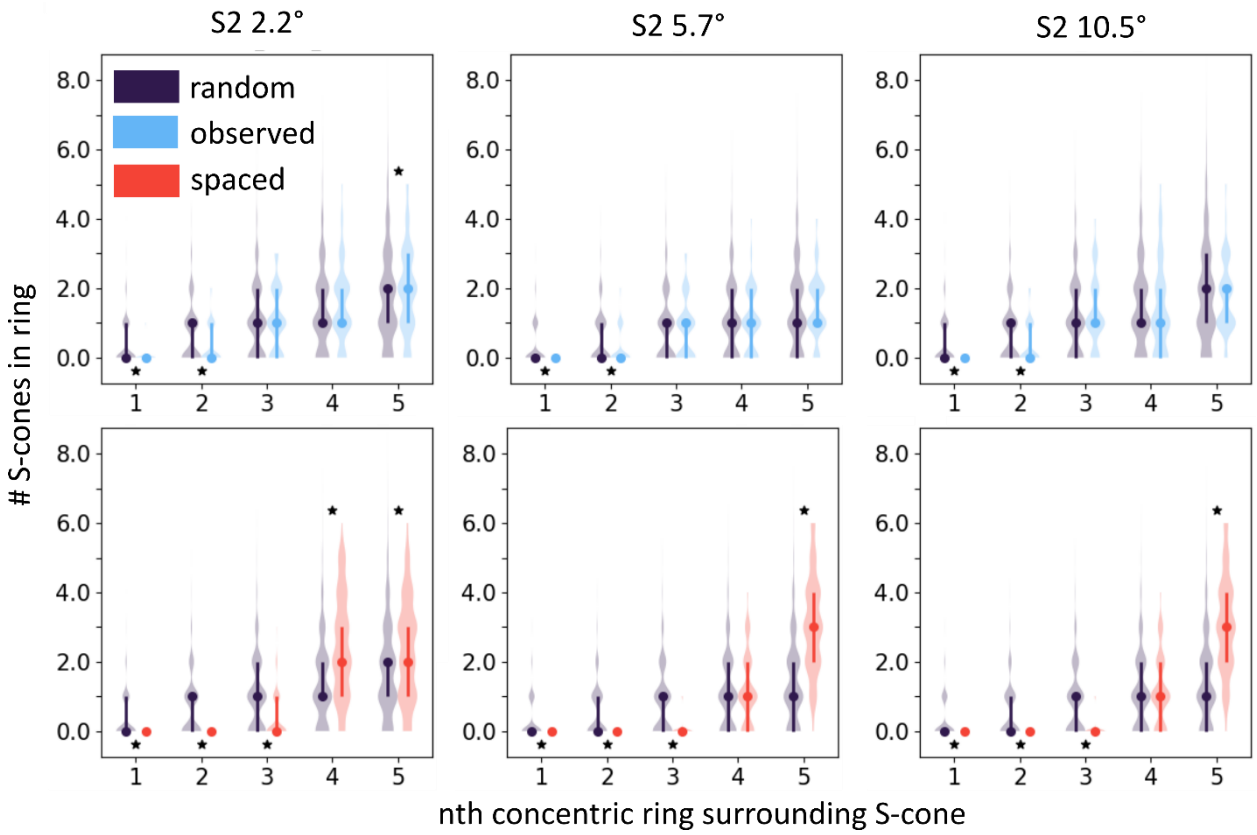

Figure 3.3 Concentric Ring Analysis (CRA) Example. CRA analysis of the observed S-mosaic and one spaced S-mosaic for the three ROIs spanning the nasal meridian of Subject 2. Observed results are shown in the top row, and spaced in the bottom, with columns of increasing eccentricity. The number of cones in the first 5 rings of S-cones in 1000 random distributions are shown in each plot in purple (random data are the same in top and bottom row). Violin plots are marked with circles at their medians and vertical lines spanning the 25th-75th percentiles. The test-mosaic (observed or spaced) distributions of S-cone quantity per ring are shown to the right of each random distribution. Stars indicate a p-value < 0.05 from a left- (star below) or right- (star above) Mann-Whitney U Test. The first two and three rings are significantly low for the observed and spaced S-mosaics, respectively. This indicates an ExRr of two and three rings. Significantly high S-cone prevalence is seen in rings subsequent to the S-exclusion zone in all spaced S-mosaics and the central-most observed.

We measure the regularity metric Exclusion Factor (analogous to the Packing Factor of DRP) as the squared ratio of the median ExRa to eMR. Exclusion Strength is added as the 1 – the proportion of cones within the exclusion radius of S-cones that are S-type, as a second measure of regularity.

3.3 Results

3.3.1 Basic cone topography across the retina

Several metrics critical to describing the classified regions were recorded, including total cone density, S-cone density, S-cone proportion, and µINDa. These will be referred to as "basic topography metrics" throughout. The basic topography metrics can be found in Appendix B Table 3.1, and a subset of basic metrics are shown in Fig 3.4.

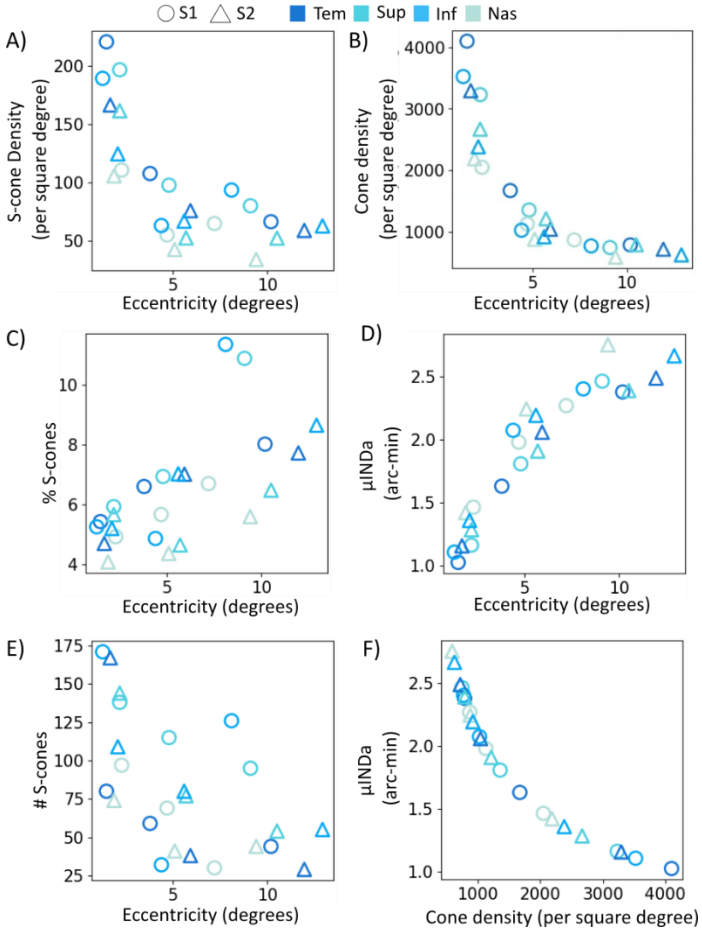

Fig 3.4. Basic topography metrics. Topography metrics shown for 24 ROIs, 12 each for subject S1 (circles) and S2 (triangles). S-cone density, S-cone proportion, and the number of S-cones sampled are shown in A, C, & E respectively against eccentricity. Overall cone density is shown in B. µINDa, the average distance between neighboring cones, is plotted against eccentricity and cone density in D and F.

Generally, basic topography metrics did not differ across the four meridians. We found that S-cone proportion increases and S-cone density decreases with eccentricity, consistent with previous reports. There is a tight, nonlinear relationship between µINDa, the average distance between neighboring cones, vs. total cone density and eccentricity, decreasing and increasing respectively. The slope of µINDa vs cone density is steepest and linear at the lowest cone densities measured between ~500-1000 cones per square degree. The rate then decreases and appears linear again from densities of ~2000-4000 cones per square degree.

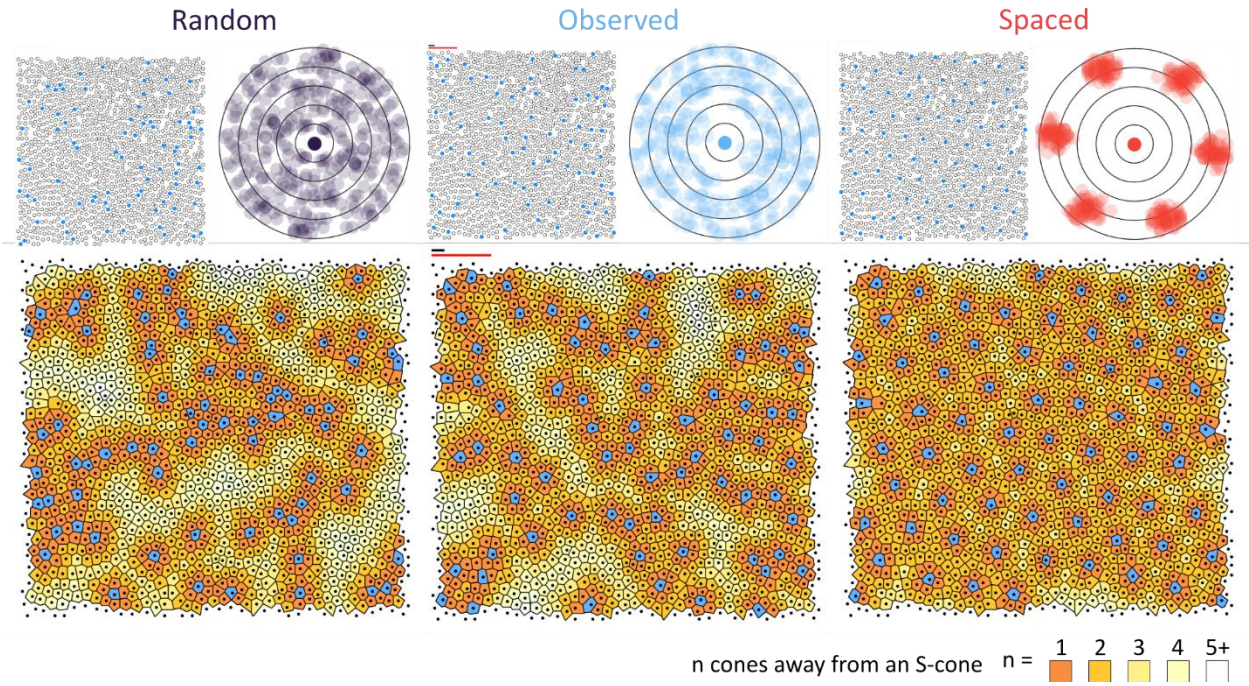

Figure 3.5 Random, Observed and Spaced S-mosaics. On the top row center, the observed S-mosaic of S1 1.5 ° temporal is shown with S-cones labeled in blue, and the autocorrelogram generated from the S-mosaic to its right. Below is the same S-mosaic represented as a Voronoi Tessellation where S-cone cells are labeled in blue, and non-S-cones are colored by their distance from the nearest S-cone in terms of neighboring cone relationships. The same is shown for 1 of 1000 random and spaced S-mosaics to the left and right of the observed. Note: the mosaics, tessellations, and autocorrelograms are rotated 90 degrees clockwise and flipped horizontally from the reference frame used in other figures.

3.3.2 The S-exclusion zone

3.3.2.1 Exclusion Radius

The presence of significantly low and high S-cone prevalence across the first 5 concentric rings surrounding S-cones are summarized in Figure 3.6. An S-exclusion zone was detected in 23 of 24 ROIs by identifying concentric rings surrounding S-cones with significantly few S-cones, compared to random S-mosaics. The exception was S2 5.93° temporal, an ROI which contained S- cones (38), but not the fewest (29, 32, and 30 S-cones in S2 11.94° temporal, S1 4.4° inferior and S1 7.2 superior respectively). Exclusion zones were identified in all spaced mosaics. For all S-mosaics with S-exclusion zones, the CRA metrics Exclusion Radius (ExR), Exclusion Factor (ExF), and (ExS) were calculated. The ExRr result was the same whether calculated from the number or percentage of S-cones per ring.

Twenty of 24 ROIs had significantly few S-cones in the first two concentric rings surrounding S-cones - an ExR of 2 rings. 3 of 24 had an ExR of 1 ring. Spaced mosaic ExRs spanned 2-4 rings, with medians of 2, 3,

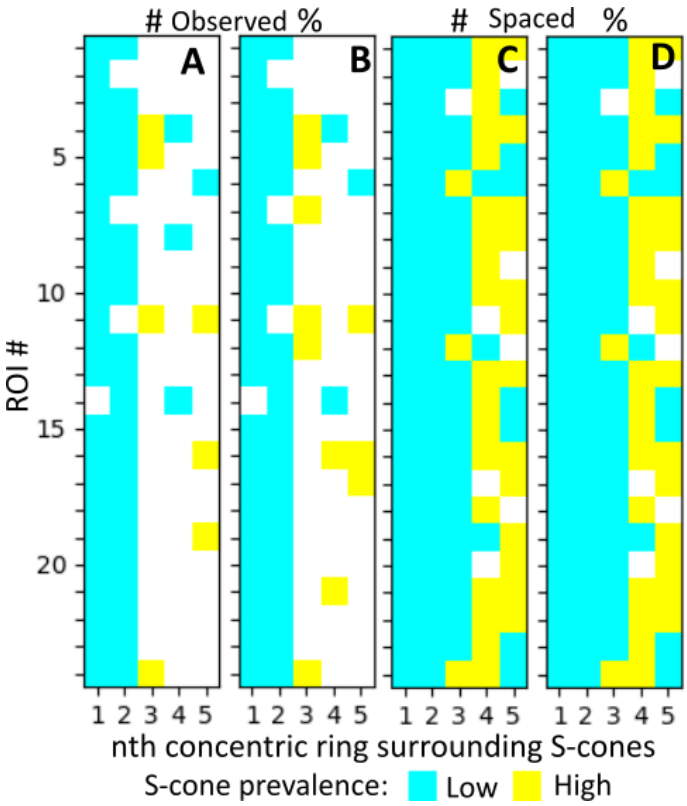

Figure 3.6 Significantly low and high S-cone prevalence in concentric rings of cone neighbors surrounding S-cones. The prevalence of S-cones per ring surrounding S-cones in observed and spaced S-mosaics (1 per ROI), compared to 1000 random S-mosaics per ROI, are indicated. Every ROI is represented by a row of 5 corresponding to the first 5 concentric rings surrounding S-cones in that ROI, with rows corresponding to the ROI IDs of Table 1. Color indicates whether S-cone prevalence for the nth ring is significantly high (cyan), low (yellow), or indistinguishable from random (white). S-cone prevalence was measured either by the number of S-cones per ring, or the proportion of S-cones per ring. **A,B)** Observed. **C,D)** Spaced. **A,C)** Calculated from number of S-cones per ring. **B,D)** Calculated from proportion of S-cones per ring.

and 4 rings in 4,19 and 1 ROIs, respectively. The four mosaics with lower (or lack of) ExRs were between ~2 and 5°. They didn't have particularly high or low S-cone proportion, nor did they sample the fewest S-cones. The non-2-ring ExR ROIs were not otherwise distinguished in any way by the metrics we assessed.

The size of these spaced-mosaic ExRs decrease with S-cone proportion (Fig 3.8 AB), with a maximum of 4 rings at the lowest proportion, then decreasing to 3 and finally two. At the highest S-cone proportions, the observed and spaced S-mosaics had the same ExR. A minority of the observed S-mosaics had significantly high S-cone prevalence in rings after the S-exclusion zone, and in fewer than that (only one overlapping) we see a significantly low 4^{th} or 5^{th} ring. There are slight differences between the post-S-exclusion zone rings when calculated with number of S-cones versus proportion of S-cones per ring for the observed S-mosaics.

In all spaced S-mosaics, we see at least one ring after the S-exclusion zone that has significantly high S-cone prevalence. In some, this is followed by a second significantly low ring, and it's unclear how the pattern would progress if rings beyond 5 were included.

The ExR is described in terms of arc-min as the distance of all cones in the outermost ring S-exclusion zones. The distance of rings increase linearly with µINDa (Fig 3.8 BC), meaning that with a constant ExR of 2 rings across the retina, we see the ExR in arc-min increase linearly with µINDa. The same is true of the spaced mosaics.

3.3.2.2 Appearance of the S-exclusion zone

Autocorrelograms of the S-cone mosaic allow visual inspection of the S-exclusion zone. In Figure 3.5, ROI S1 1.5° temporal is shown with examples from its random and spaced synthetic counterparts. The autocorrelograms alone demonstrate that the S-cones of the real mosaic have a dearth of S-cones surrounding them that is distinct from the uniform coverage of S-cones in the example random arrangement. Outside the zone of low-to-no S-cone occurrence surrounding S-cones, the autocorrelogram resembles the random mosaics. The spaced mosaic on the other hand has a larger S-cone free zone with the nearest S-cones falling at consistent distances and angles from the center, consistent with an arrangement close to a hexagonal grid.

We observed that in some ROIs, particularly at lower eccentricities and along the nasal-temporal axis, there was a clear asymmetry in the exclusion zone. These asymmetric exclusion zones appear longer along the temporal-nasal axis for temporal and nasal ROIs and along the superior-inferior axis for the inferior and superior mosaics. This effect was evident in both subjects. An autocorrelogram of M5 (a temporal ROI) of Roorda et al 2001 shows the same anisotropy. It is unclear if it is absent in our more peripheral ROIs and JWT (also temporal), or if it isn't visibly evident with due to fewer S-cones contained

in those ROIs. The same is true for ambiguity whether the nasal-temporal anisotropy is more robust than the superior-inferior.

3.3.3 S-mosaic regularity

ExF describes regularity in terms of the size of the ExR relative to the maximum distance of the same number of evenly spaced points, eMR (derived experimentally, 3.2.3.2). eMR increases with µINDa at a

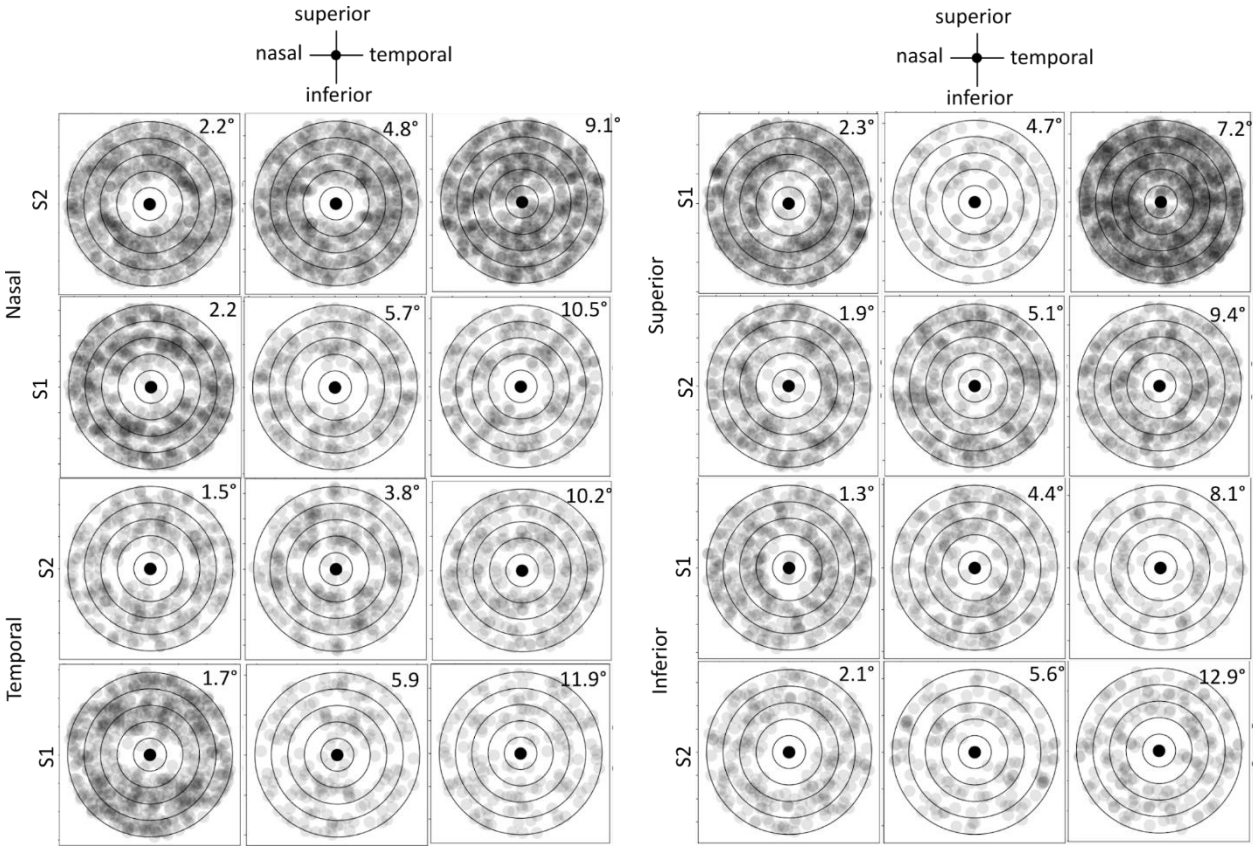

Fig 3.7. Autocorrelograms of S-mosaics. All ROIs from S1 and S2 are represented. The black circle at the center of each plot represents each cone in the S-mosaic, while the circles at 10% opacity represent the relative positions of other S-cones within 5 times µINDa arc-min of each S-cone. Each annulus surrounding the central circle is equal to µINDa for that ROI. **Nasal-Temporal Axis (Left):** The S-exclusion zone is qualitatively visible in 9 of 12 autocorrelograms, excluding S1 9.1°nasal, S1 10.2 °temporal, and S2 11.9°temporal. In 6 of the 9 with visible exclusion zones, including all at the lowest eccentricities as well as S1 4.8°nasal and S1 3.8°temporal, the exclusion zone appears larger along the nasal-temporal axis than the superior-inferior axis. **Superior-Inferior Axis (Right):** The S-exclusion zone is qualitatively visible in all but S1 4.7°superior, S1 7.2°superior. Asymmetry of the exclusion zone is less apparent along the superior-inferior axis than the nasal-temporal axis. For S1 1.3°inferior and S2 2.1°inferior and S1 8.1°inferior, S2 inferior 12.9°, the exclusion zone appears longer along the superior-inferior axis.

similar rate as the median spaced ExR (not shown). Observed S-mosaic ExF increases linearly with S-cone proportion.

ExS describes regularity in terms of the strength of the exclusion zone - that is, how reliably it excludes S-cones. The ExS of observed mosaics decreased with proportion, anti-correlating with their increasing ExF. We see a similar trend in spaced S-mosaics with increasing S-cone proportion; as S-cone proportion increases, the Exclusion Strength measured decreases, until the spaced S-exclusion zone is constrained

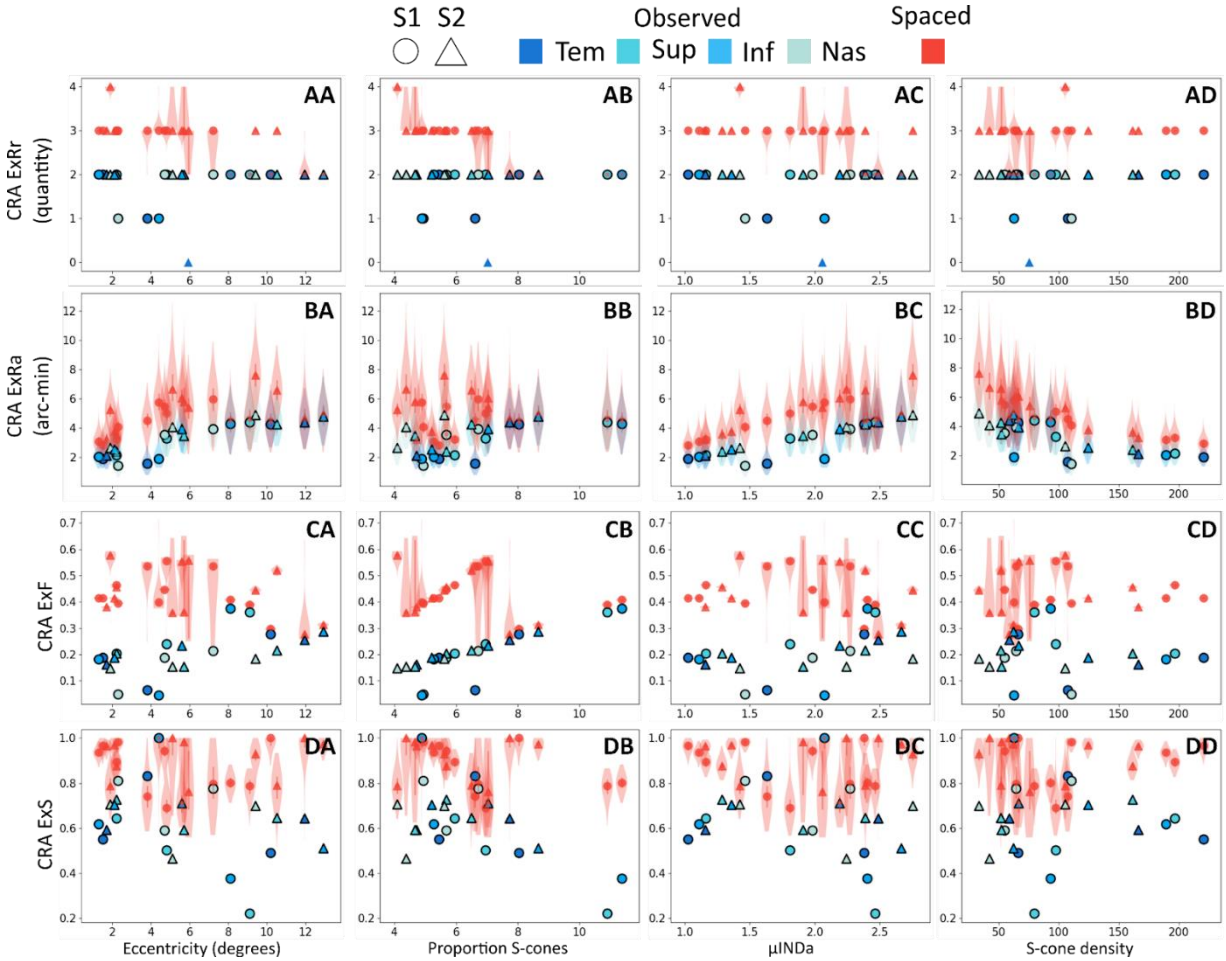

Figure 3.8. Concentric ring analysis (CRA) metrics across the central retina. CRA metrics (ExRr: Exclusion Radius (rings), ExRa: Exclusion Radius (arc-min), ExF: Exclusion Factor, ExS: Exclusion Strength) calculated for the 24 ROIs and their spaced counterparts are shown with Eccentricity, S-cone proportion, µINDa, and S-cone density. Rows A-D indicate CRA metric (y-axis), and columns A-D indicates the x-axis, yielding two-letter pairs to ID each subplot, AA-DD. Shape indicates subject, shades of blue indicate meridian for observed S-mosaics, and pink indicates spaced S-mosaics. Violin plots are used where there are multiple measures (all metrics for spaced and ExRa for observed S-mosaics), with the marker at the median and a line spanning the 50% confidence interval.

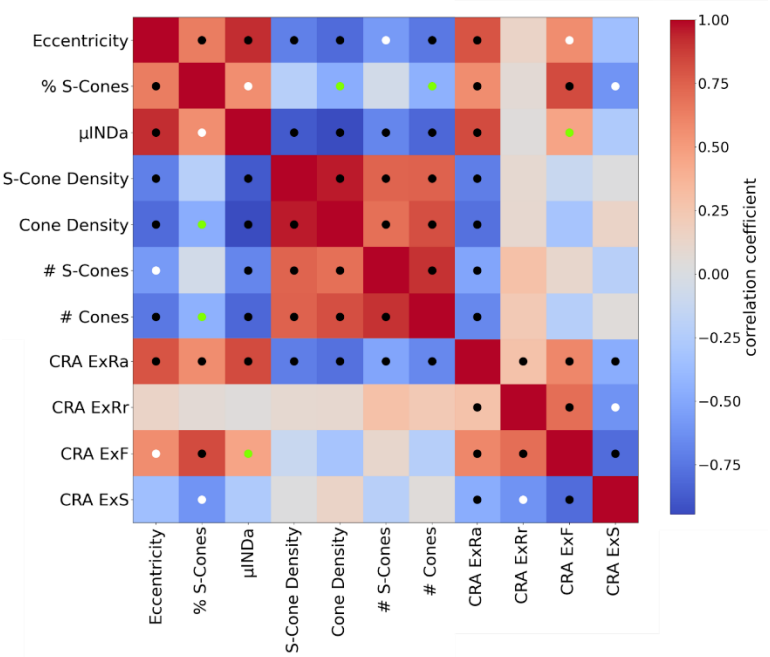

Figure 3.9. Cross correlation of topography metrics. Pearson cross correlation coefficients calculated for basic and S-cone CRA topography metrics are indicated by grid-square color, where redness increases with correlation and blueness increases with anti-correlation. Dotted squares indicate a significant p-value (green: < 0.05, white: < 0.01, black: <0.001)

one-ring smaller by the S-cone proportion. Given this result, we can't rule out the effect of S-cone proportion on ExS in the observed mosaics.

3.3.4 Re-analyzed Roorda 2001 data

M5 and JWT are the macaque and human subjects with the largest continuous classified cone mosaics of their species' in Roorda et al 2001. Using CRA analysis, these ROIs were both found to have ExRs of 2 rings, like the majority of ROIs in S1 and S2. Previously an S-exclusion zone was detected in M5, but not JWT. The reanalyzed ROIs are shown with their respective Voronoi Tessellations, CRA plots, and autocorrelograms in Figure 3.10.

3.4 Discussion

We identified a pattern of the human S-exclusion zone that has not been previously described - that it occupies a radius of 2 rings surrounding S-cones. This finding was supported by a novel Concentric Ring Analysis (CRA) that is more sensitive to such a pattern than the classic method. This pattern suggests that the S-exclusion zone comes from a mechanism that scales with distance between neighboring cones.

We also applied CRA to publicly available data of Roorda et al 2001, selecting the macaque and human ROIs with the highest cone number of cones found the same pattern. It is unclear whether the pattern is as persistent in macaque as it is in humans, but an exciting new direction to consider is that the macaque and human S-cone topography could be more similar than previously recognized. From our analysis, it appears that the higher regularity of the macaque mosaic, noted in Roorda et al consistent

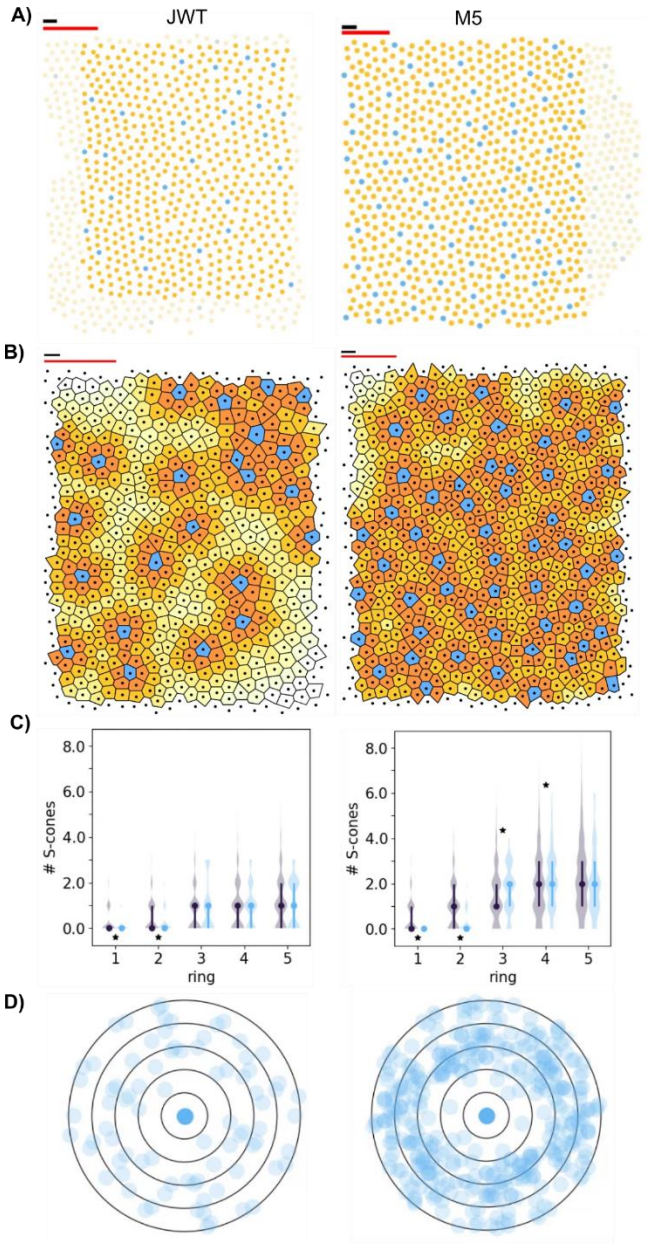

Figure 3.10. Re-analysis of monkey and human data from Roorda 2001. Left column: Human (JWT), Right: macaque (M5) **A)** Previously published ROIs. S-cones and non-S-cones are colored blue and yellow, respectively. The rectangular cropped area reanalyzed is shown in full opacity. Red line: 5 arc-min. Black line: µINDa. **B)** Voronoi tessellations as in Figure 4. S-cones cells are colored blue, and non-S cones are colored by how many neighboring-cones away the nearest S-cone is (yellower and less saturated = further). **C)** Plots of CRA analysis results. An ExRr of 2 is seen in both ROIs (stars below the first two rings' results). There is a significantly high peak in S-cone prevalence following the M5 S-exclusion zone. **D)** S-cone autocorrelograms, as in Figure 3.5. Horizontal elongation is qualitatively visible in M5. It not visibly clear whether this is the case in JWT also, due to relatively few S-cones.

with many previous studies, could be purely the result of the higher proportion of S-cones making up their cone mosaics.

ExRa measured from CRA tells us size of the S-exclusion zone in the ROI in terms of arc-min, as the distribution of S-cone distances from the cones of their zone's outer ring. In chapter 4, we show the S-exclusion radius measured with DRP tended be at the lower extreme of ExRa measured for the same ROI. This is consistent with the DRP ER of previous studies at comparable eccentricities to ROIs in this study. Curcio et al 1991 ROIs at 1.2° and 9.1° had an ER of 1.71 arc-min (non-significant) and 3.74 arc-min (significant), respectively, when measured by Martin et al 2000 with DRP. The Cornish et al adult ROIs at 1.6° and 5.4° had ExRs of 1.6 arc-min (not significant) and 2.2 arc-min (significant), respectively. We don't have the S-cone proportion or cone density for these ROIs, and so cannot compare their S-exclusion zones further. See Table 1.1 for metadata associated with these ROIs from the literature and Table 1.2 for more detail on previous DRP results.

CRA, as well as the classic DRP, are best suited for describing patterns that are radially symmetric. We observed the shape of the central gap of autocorrelograms for mosaics at lower eccentricities appear oblong, longer along the nasal-temporal axis for the horizontal meridian, and longer along the superior-inferior axis for the vertical meridian. It is unclear whether the oblong shape of the exclusion zone only being evident at lower eccentricities is due to true variability of the S-exclusion zone across the retina, or if the property persists at high eccentricities but is cloaked by relatively few S-cones per in these ROIs. Characterization of the S-exclusion zone can be improved with an approach that can account for non-circular S-exclusion zones, and analysis of how variability in cones per ROI influences topographic metrics.

We have not looked into the minimum sampling of S-cones needed to reliably detect the S-exclusion zone, which is a complicated problem due to myriad variables. Our dataset samples ~100-200 S-cones per ROI at lower eccentricities, ~1-2°, while the Hofer et al ROIs and the rod-free-zone ROI of Curcio 1991 sampled 24-66 S-cones per ROI. The adult human ROIs contributed by Cornish et al 2004a sampled substantially more S-cones at the perifovea and periphery than we have, 1057 at 1.6° and 428 at 5.4 °. The peripheral ROI of Curcio 1991 also surpassed our S-cone sampling, 184 cones at 10°, whereas in this vicinity we generally collected less than 100 cones. It is possible that the lower sampling of previous work at lower eccentricities played a role in not detecting an S-exclusion zone, in addition to other weaknesses of DRP alluded to in Chapter 4.

3.5 Supplement

3.5.1 Spaced S-mosaic Algorithm

First, a hexagonal grid of points is created. Points of the grid are separated by a distance equal to an estimate of the maximum radius possible given the cone mosaic density in the ROI, where this distance was calculated according to the method described by Rodieck 1990. Generating a hexagonal grid of points as such without preserving cone locations is trivial, but generating a maximally spaced S-cone mosaic over the native cone mosaic canvas requires additional steps. The hexagonal grid above is centered over the cone mosaic ROI in question, and jittered in (x,y) (bounded by the maximum radius) and rotational orientation (1 – 360°) by a random amount to create 1000 unique simulations of spaced mosaics. Cones in the native mosaic lying closest to the hexagonal grid points of the jittered variants are selected to be labeled as S-cones and constitute the spaced S-mosaic. One caveat for this approach, however, is that the maximum radius has limitations as defined, and its use alone to create the spaced mosaic leads to a different number and density of cones compared to the observed S-cone mosaic. Thus,

the maximum radius was used as a starting point to create the hexagonal grid, and then its value was iteratively increased or decreased to minimize the difference between the number of S-cones in the spaced and observed mosaics.

1. The maximum spacing for the number of cones in the observed S mosaic in the rectangular bounds is first estimated using Rodieck's "max-radius" estimate (Rodieck 1991). This metric takes density as a single parameter, and is most accurate for square rectangular bounds of points.

2. A large hexagonal grid of points is generated wherein points are all Rodieck's max-radius apart from one another, centered on the relatively small rectangular bounds of the reference. This grid is translated a random number of pixels horizontally and vertically, and rotated a random degree about its center.

3. The grid is cropped to the rectangular bounds of the classified image

4. The density of the remaining points is calculated

5. Unless the density calculated is equal to the observed S mosaic density, repeat steps 1-4 using a spacing of the max-radius estimate plus or minus one pixel (plus if the previous density generated was too high, minus if it was too low), and using the same translation & rotation was randomly selected in 2.

6. Repeat 5 until the generated density is equal to the target density, or until the difference between the generated and target density changes sign.

    a. If the former, keep the mosaic generated.

    b. If the latter, select from the current and previous mosaic generated, whichever produces a density closer to the target.

4: Methods to describe the S-exclusion Zone and regularity of the S-mosaic

4.1 Introduction

A semi-regular arrangement of S-cones has been described in humans and other mammals with visual systems specialized for high acuity color vision since the advent of S-cone selective stains (see 1.4). The functional consequences and developmental origins of this pattern are not known. Measuring the spatial characteristics of semi-regular S-cone topography is a critical step to understanding this phenomenon in the broader context of vision. Previous studies have endeavored to do so across the retina in many species and developmental stages by describing the area surrounding S-cones where other S-cones are significantly less likely to be found than if they were randomly distributed in the cone mosaic - here referred to as the S-exclusion zone.

All efforts to describe the semi-regular S-mosaics have hinged on measurement of the zone's radius, here referred to as the Exclusion Radius (ExR). Efforts to simulate pseudo-S-cone topography as seen in macaques, ground squirrels, and humans have found that imposing an S-exclusion radius with some degree of variability, while otherwise allowing the S-cones to be randomly distributed, can closely approximate observed semi-regularity. Thus, the understanding of S-mosaic semi-regularity is that it arises from a developmental scheme where S-cones are randomly arranged with respect to one another, besides an exclusion radius which surrounds each one and drives them apart. The crux of characterizing S-mosaic semi-regularity is to measure the characteristics of that S-exclusion zone.

The S-exclusion radius has classically been measured using the Density Recovery Profile (DRP), created specifically to characterize regularly distributed populations of retinal cell types.[60] While methods relying on Voronoi tessellations (see 3.2.4.1) have also been relied upon to test whether retinal cell arrangements are significantly more regular than random distributions, they have not facilitated estimation of the S-exclusion radius. DRP provides such a metric with the Effective Radius (ER).

DRP is a representation of the cells of interest's density as a function of distance from each other. ER estimates a radius from 0 where the cell density is lower than the overall cell-density. A metric called Packing Factor (PF) can then be calculated as an estimate of regularity between 0 and 1, as the squared ratio of ER to the maximum exclusion radius possible (MR, estimated from the cell density).

DRP has proven extremely useful in the study of retinal cell types' regularity. The ER has been shown to be relatively immune to random cone dropout, and the PF is touted for comparative studies because of its density-independence. A given cell type's density can vary widely across individual retinae, between individuals, and between species, making density-independent measures crucial to comparisons. For S-cone topography, PF has been measured across myriad species, particularly primates, to reveal a spectrum from random S-cone arrangements in marmosets to highly regular ones in macaques, with humans somewhere in between. PF has also been used to track the spatial-temporal pre- and post-natal development of regular S-cone mosaics in humans and macaques.

However, the topography of S-cones is unique among retinal mosaics (the term often used to describe regular arrangements of cells and/or visual receptive fields tiling the retina) in many ways. Other cell types exhibiting regularity in their arrangement tend to fully tile the retinal surface. The receptive fields of many bipolar, amacrine, and retinal ganglion cells have been shown to fully tile the visual space, with the receptive fields overlapping very slightly at their edges. Notably, semi-regular S-cone arrangements do not seem to share these properties. They tend to be relatively sparse in the photoreceptor layer, making up ~4-15% of cones, and do not evenly sample the visual space unless they are extremely regular (a PF near 1). Furthermore, the semi-regular S-mosaic's S-exclusion property is apparently less exclusive than other retinal mosaics. Although S-cones are significantly few within the S-exclusion zone, they may be found occasionally within each other's exclusion radii and even abutting.

Unique properties of S-cone topography present challenges for measuring the S-exclusion radius that have not been explored previously. We found these challenges to be an obstacle in our ability to confidently describe human S-cone topography with classic methods. In this report, we describe our particular concerns regarding classic approaches to study the semi-regularity of S-mosaics and means to overcome them.

Our first attempt to improve upon established methods was a Two-Point Correlation (2PC) analysis approach, which has many similarities to DRP. 2PC describes inter-S-cone distances in terms of its similarity to a random uniform distribution of points. For both DRP and 2PC, results are highly influenced by bin-widths used to represent the data. We analyzed simulated mosaics with known exclusion zone properties using a variety of binning strategies to inform our selection of bin-width based on detection sensitivity to, and accuracy of, the ExR. The 2PC approach proved to outperform DRP for detection of the S-exclusion zone, which was generally less likely to detect S-exclusion zones.

Despite improvements in detecting the S-exclusion radius, we found that the challenges of binning in these analyses were so detrimental to estimates that we could not reliably characterize whether and how the S-exclusion zone (and by extension, S-mosaic regularity) varies across the retina, individuals, and species. We overcame these challenges with a novel approach called Concentric Ring Analysis (CRA), which relies on analysis of the Voronoi tessellation constructed from the mosaic of all cone types (see 3.2.4.1-2). This approach describes S-cone topography with respect to how many cones apart they are, determined by neighboring-cone relationships in the tessellation. This approach is density independent and proves to be more sensitive to the presence of the S-exclusion radius than 2PC. It is also sensitive to the peaks of S-cone prevalence just outside the S-exclusion zone, which DRP and 2PC are generally insensitive to. This further suggests that this method is better suited to capturing the semi-regular pattern than previous approaches.

Ultimately, these findings led us to use CRA to describe the S-Exclusion, which allowed us to identify novel patterns to S-cone topography (see Chapter 3). We allude to how DRP's weaknesses may have influenced previous studies in 4.4, but this is unpacked in more detail in 3.4 where previous findings are compared to our study's results. In both the 2PC and CRA approaches, the Exclusion Strength (ExS) is quantified, which has not been directly quantified in previous studies and plays a fundamental role in S-mosaic regularity (see Figure 3.1).

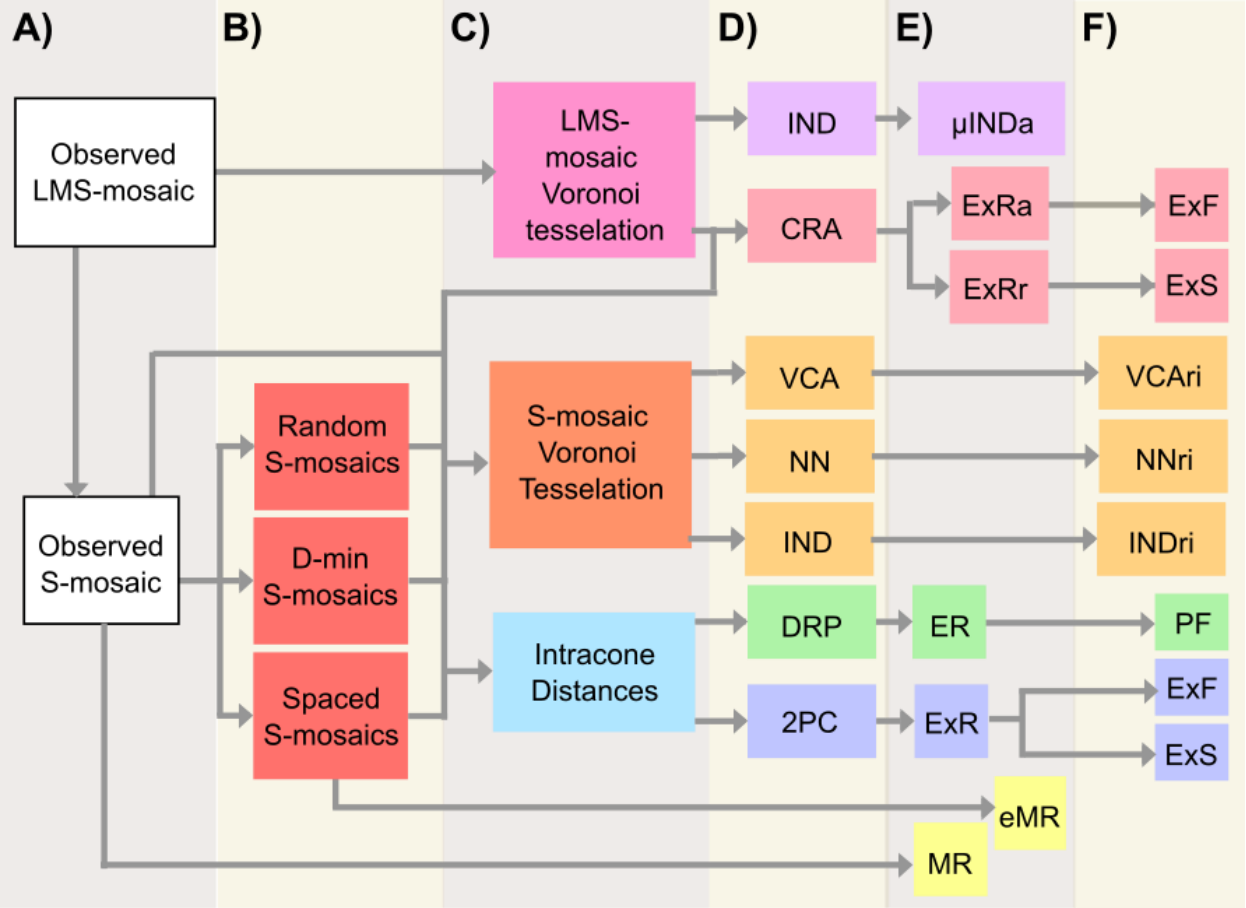

Figure 4.1. Topography Analysis Pipeline. Flowchart depicting the flow of model generation and analysis from the location of cones in each classified mosaic. **A)** One classified ROI. Each classified ROI begets coordinates of the observed LMS mosaic and its S-mosaic. **B)** Simulations. Simulated -mosaics are generated for each classified ROI with the same number of cones* as observed S-mosaic from observed cone positions in the LMS-mosaic. Random, D-min, and Spaced models are used to create distinct populations of mosaics with imposed spatial properties. **C)** Representations of cone mosaics. Cone coordinates are represented using Voronoi and Spatial Point processes. **D)** Topography analyses. Four types of topography analysis are applied. VCA: Voronoi cell area, NN: Number of neighbors, IND: Inter-neighbor distance, DRP: Density Recovery Profile, 2PC: Two-point correlation, CRA: Concentric ring analysis. **E)** Primary topography metrics. Metrics are collected from each type of analysis that all differently describe the S-cone topography. ER: Effective Radius, ExR: Exclusion Radius, µINDa: mean IND of the total cone mosaic, ExRr: ExR calculated from CRA in terms of number of rings, ExRa: ExR calculated from CRA in terms of arcmin, MR: maximum radius, and eMR: empirical maximum radius. Two metrics, MR and eMR, are calculated directly from the observed S-mosaic and Spaced S-mosaic generation process, respectively. **F)** Regularity metrics. From primary topography metrics, secondary metrics that specifically describe S-mosaic regularity are calculated. VCAri, NNri, and INDri are calculated directly from the topography analyses.

4.2 Methods

4.2.1 Cone Classification & Subjects

In these experiments we analyzed the same spectrally classified data described in Chapter 3, S1 and S2. Data re-analyzed from previous literature in Chapter 3 is not included here. The 24 ROIs spanning the

central ~1-12° of S1 and S2 are shown and detailed in Appendix A and Appendix B Table 3.1, respectively.

4.2.2 Simulations

4.2.2.1 Uniform random point distributions

Uniform-random point distributions were generated to represent the random spacing that is agnostic to where cones are actually located in an observed ROI (unlike random, spaced, and d-min S-mosaics). They contain the same number of cones as their reference observed mosaic, distributed randomly and independently within the rectangular ROI edges. For each mosaic-set, 100,000 such distributions were created. They serve to represent the lower bound against which regularity may be detected in a mosaic.

4.2.2.2 Random & Spaced S-mosaics

For every ROI, 1000 random and spaced mosaics were generated. These are the same as those described in Chapter 3 (see 3.2.3). These simulations allow us to examine how analyses differently capture minimally and maximally regular S-mosaics, and the place of observed S-mosaics within the spectrum.

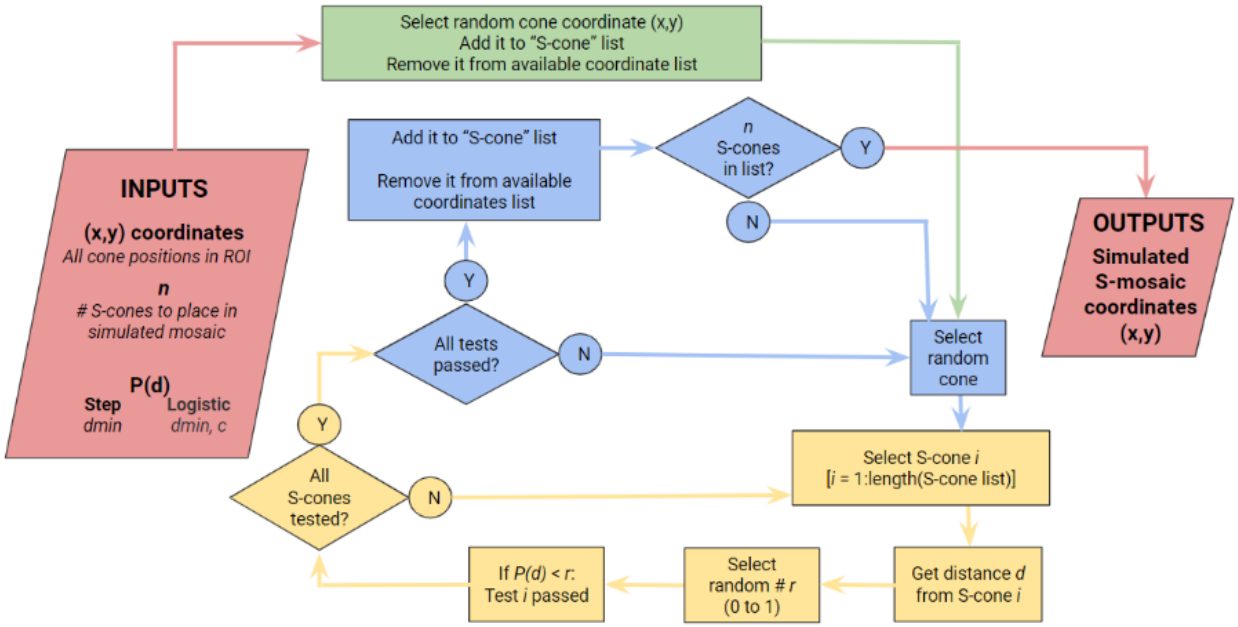

Figure 4.2 Simulating pseudo-S-cone topography with the d-min model. The procedure of generating d-min S-mosaic simulations, adapted from Galli-Resta et al 1999 is illustrated with a flowchart. Model input and outputs are shown in pink. The process begins by seeding the d-min mosaic with a randomly selected cone (green). From there, the algorithm goes through a nested-loop procedure of randomly selecting candidate cones to be added to the S-mosaic and subjecting them to probability tests based on their distance to already-added S-cones (blue and yellow loops) until the correct number of cones have been added.

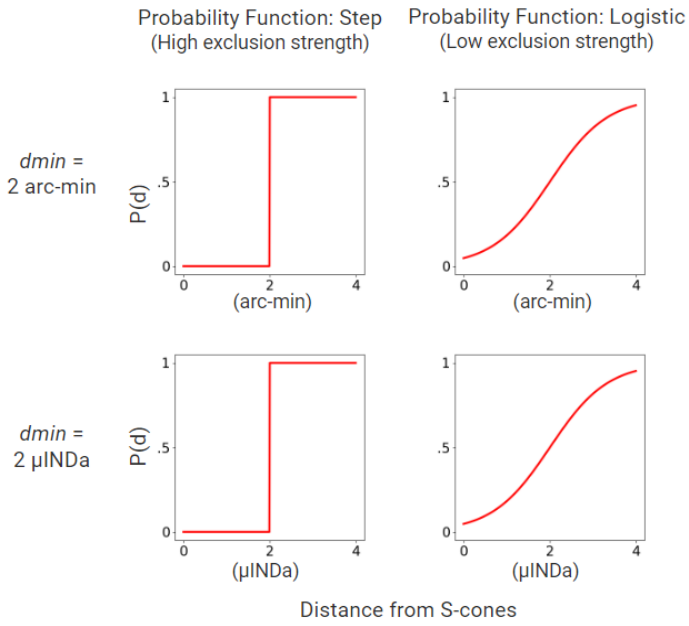

Figure 4.3 Probability functions input to the d-min model. For the Four populations of d-min S-mosaics were generated with S-exclusion zones of distinct radii and strength. Probability functions input to the d-min model *P(d)* impose the differences in S-exclusion zone characteristics across the four populations. The four probability functions applied are shown. Rows corresponding to the d-min parameter *d* input to *P(d)* and columns corresponding to the shape of the probability function. *d* is set to either 2 arc-min or 2 µINDa. The probability function is either a step or a logistic function. For the step function *P(d)*, *d* is the minimum distance between any two S-cones (high exclusion strength). The logistic function *P(d)* has an inflection point (where *P(d)* = .5) set to d. Steepness of the inflection point is set by a growth coefficient parameter, here kept constant at 0.5 such that the *P(d)* is just above 0 at *P(0)* and just below 1 at *P(2*d-min)*.

4.2.2.3 D-min S-mosaics

These simulations are adapted from the "d-min model" described in Galli-Resta et al 1999, who used it to model the semi-regular arrangement of S-cones in ground squirrel retinae. Their d-min model operates by adding a probabilistic minimum distance rule to the iterative random cone-selection algorithm that simulates random arrangements. The probability function used by Galli Resta is defined by two input parameters; a minimum distance (d-min) that defines the mean of a normal gaussian function *P(d)*, and a standard deviation. For every cone added to the d-min S-mosaic, a random number drawn from *P(d)* is assigned as that cone's "minimum distance." For a randomly selected cone to be included in the S-mosaic, it cannot be within the minimum distance of the S-cone already added.

Our application of the d-min changes the probability function step in two ways. First, we didn't define P(d) as a gaussian function, instead using either a step function or a logistic function. The step function P(d) is defined by the single parameter of d-min, such that P(d) = 0 if d < d-min and P(d) = 1 if d > d-min. The logistic function P(d) is defined by its inflection point, d-min, and a growth coefficient that

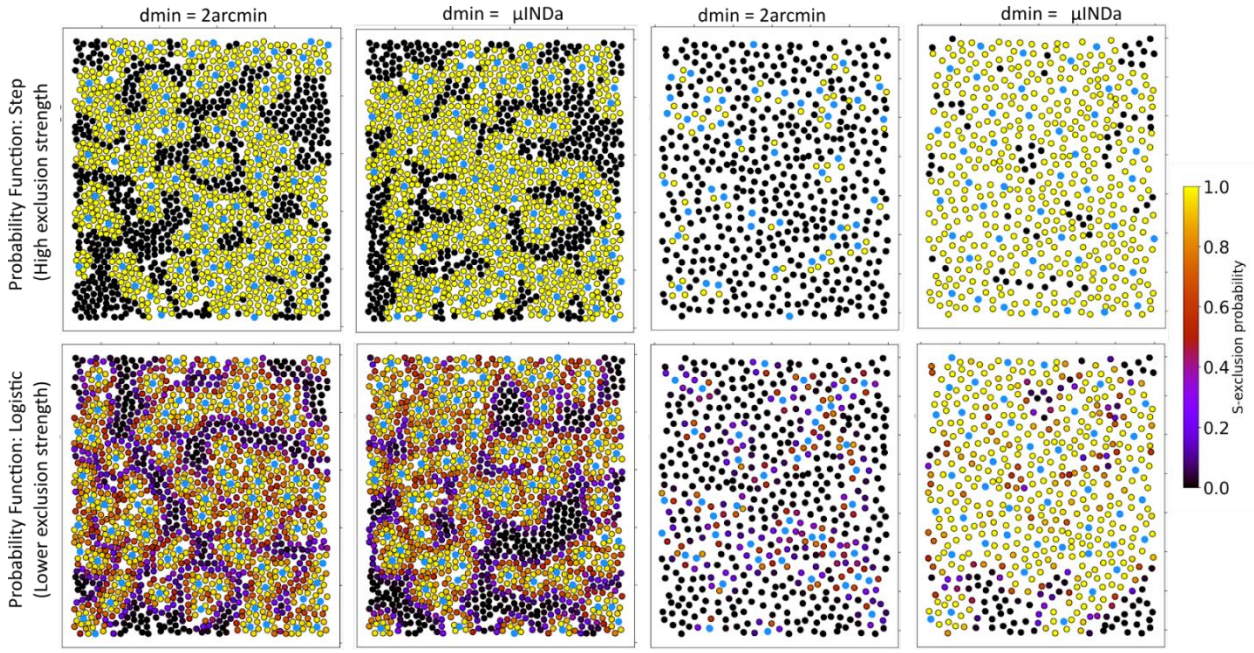

Figure 4.4 Example d-min mosaics with varying S-exclusion zone characteristics. Simulated d-min mosaics generated in the cone mosaics of S1 Temporal 1.5 (left two columns) and 10.2° (right two columns) are shown. These representations of the synthetic S-mosaics visualize the S-exclusion zone properties that shaped them. A circle is plotted at each cone position. S-cones of the synthetic mosaic s are colored blue. Every non-S cone is colored according to its distance d from the nearest S-cone, given the function P(d). The function P(d) varies for each of 6 conditions, outputting values between 0 and 1 that signify the probability that an S-cone would be located at the position, given the proximity of the nearest S-cone. In reality, the probability that a randomly selected cone is included during the d-min S-mosaic generation process is dependent on its distance from all S-cones already in the mosaic, not just the nearest. But this visual approximates the differences in the S-exclusion zones produced by each condition of d-min mosaic generation. Conditions 1, 2, 5, and 6 are the conditions 1-4 used to test 2PC results across d-min mosaic populations. Conditions 3 and 4 here are included to appreciate the contribution of the growth coefficient parameter to the logistic form of the probability function.

determines the slope at the inflection point, here set to 0.5. This allowed us to test conditions where the simulated S-exclusion zone has high exclusion strength (see Fig 3.1) with the step function, and a lower exclusion strength condition with the logistic function.

Second, we didn't set an explicit d-min for every S-cone added to the mosaic. Rather, for a randomly selected cone to be included in the S-mosaic, it had to pass a probability test against every S-cone already placed in the mosaic. The probability tests begin with drawing a random number *r* between zero and 1. *P(d)* is computed, where d is the distance of the candidate cone from the already-accepted S-cone it is being tested against. If *P(d)* < r, the candidate cone is rejected. Otherwise, it is accepted. The steps of the d-min algorithm as we've applied it are listed in 4.5.1, and illustrated with a flowchart in Figure 4.4, below.

While Galli-Resta et al and others have used the d-min model to approximate observed S-topography, we apply the simulations as controls to test analytic artifact. The probability function used is effectively setting S-exclusion zone properties, allowing us to appreciate differences in how spatial properties are captured given known S-exclusion radii when they are generated within observed cone mosaics varying in size, density, and S-cone proportion (see 4.2.4.1, below).

We created 4 conditions of d-min S-mosaics from the two types of P(d) functions by generating each type with two d-mins: 2 arc-min and 2 µINDa. These were made to simulate S-exclusion zones that are constant in size across ROIs and zones that would scale with the distance between neighboring cones.

4.2.3 Topography Analysis

Many topography analyses and simulated spatial distributions, new and old, were applied in these experiments. The pipeline of simulation generation and analysis is summarized by a flowchart in Figure 4.1. In brief: a "mosaic-set" is generated for each of the 24 observed S-mosaics, comprised of the observed S-mosaic and a suite of simulated mosaics tailored to it; The simulated mosaics per ROI include 1000 each of random and spaced S-mosaics, 100 each of four types of D-min S-mosaics, and 100,000 random uniform point distributions. Observed mosaics and all simulated S-mosaics are assessed with topography analyses calculated from Voronoi Tessellation representations of cone mosaics, and those calculated from Spatial Point Processes computed from inter-cone distances. Random uniform point distributions are only used for 2PC analysis.

4.2.3.1 Voronoi Tessellations

4.2.3.1.1 ALL-CONE VORONOI TESSELLATION (AVT) AND CONCENTRIC RING ANALYSIS (CRA)

The mosaic of all cones represented as Voronoi Tessellations (AVT, see 3.2.4.1) were generated for each ROI. Density of cones and S-cones and the average distance between neighboring cones, µINDa, are calculated from the AVT (see Appendix B 3.1). The systematic identification of neighboring cones provided by AVT is the basis for Concentric Ring Analysis (CRA, see 3.2.4.2). CRA yields the metrics ExRr (ExR measured in units of concentric-cone-rings) and ExRa (ExR measured in units of arc-min). ExF (S-mosaic regularity measured as the squared radius of ExRa to an empirical estimate of the maximum radius (eMR, see 3.2.3.2)), and ExS (regularity in terms of the probability of S-cone exclusion within the zone's radius).

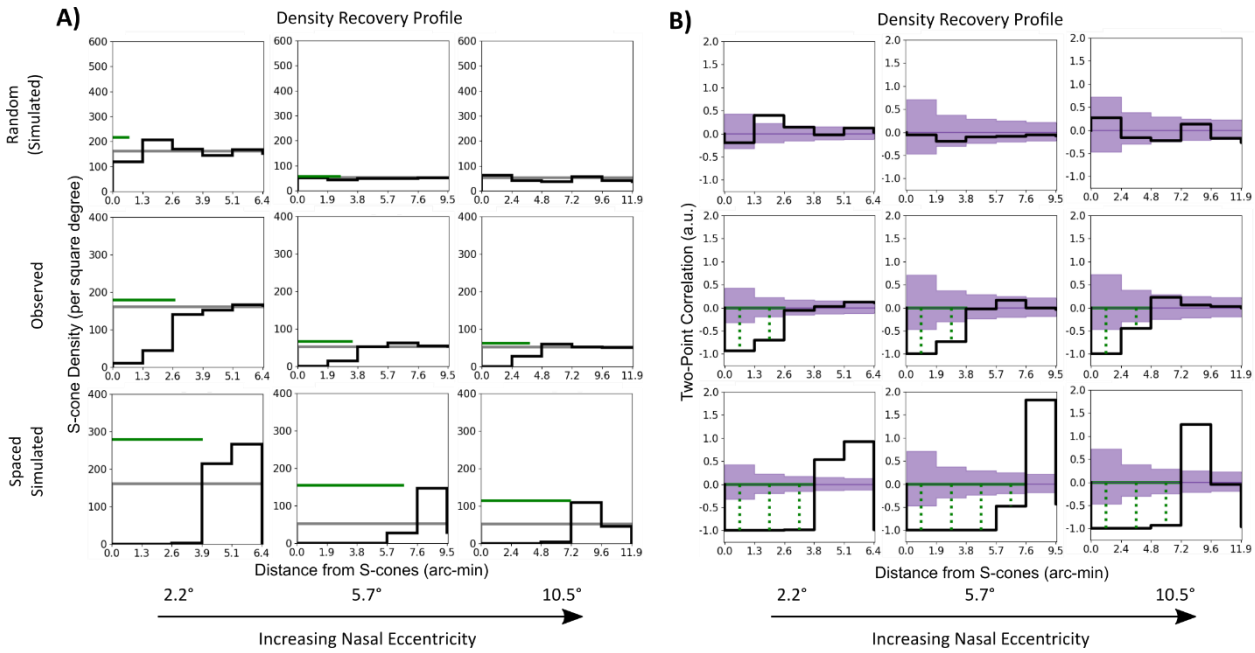

Figure 4.5. Examples of Density Recovery Profile (DRP) and Two-Point Correlation (2PC) analyses. In A and B, the middle row is analysis of observed S-mosaics, top and bottom rows are example random and spaced S-mosaics for each ROI. The three columns left to right correspond to ROIs at 2.2 °, 5.7° and 10.5° along the nasal meridian of S2. **A)** DRP plots. The density of S-cones is plotted with respect to distance from S-cones in black. The grey horizontal line marks overall density. Note the y-axis is different for the random DRP plots. The green line extending from 0 (where present) is the length of the Effective Radius (ER). **B)** 2PC plots. The similarity of the test S-mosaic inter-S-cone distances to the average inter-point distances of random uniform point distributions is plotted in black against distance from S-cones. A 2PC of 0 at any bin indicates that S-cones are equally as prevalent at that distance from other S-cones as random uniform points are at that distance from other random uniform points. A 2PC of -1 at that bin indicates no S-cones occur at that distance in the test S-mosaic. Purple shade spans the 95% confidence interval of 100,000 2PCs calculated from individual random uniform point distributions against their mean. The solid green line extending from 0 (where present) is the length of the Exclusion Radius. Hyphe Radius (ExR). Hyphenated vertical lines indicate the difference between the 2PC value of each bin within the ExR and 0. The average of the length of these hyphenated lines is the Exclusion Strength (ExS).

4.2.3.1.2 S-CONE VORONOI TESSELLATION (SVT)

We also constructed Voronoi tessellations from the positions of S-cones alone, SVTs. From these tessellations we computed a trio of metrics classically applied in cone topography analysis, Voronoi Cell Area (VCA), Number of Neighbors (NN), and Inter-Neighbor Distance (IND).[28,29,35,41,42,44,45,62–65] Distribution of VCA, NN, and IND values were calculated for each S-cone of an ROI, and from these a regularity index was calculated. The regularity index is defined as the squared ratio of the standard deviation of the metric across S-cones to its mean. The regularity indices, abbreviated VCAri, NNri, and INDri have been applied in previous studies as density independent means of describing cone

topography and determining if it is different from random distributions. While the properties of these Voronoi metrics have been explored thoroughly with regard to study of cone topography,(Cook 1996; Cooper et al. 2016; Keeley, Eglen, and Reese 2020) they have not been evaluated with respect to their representation of S-cone topography specifically.

4.2.3.2 Spatial Point Processes

4.2.3.2.1 DENSITY RECOVERY PROFILE

The Density Recovery Profile is a spatial point process that quantifies the density of a set of points in 2 or 3 dimensions as a function of distance from any given point. This is done by calculating the distance between all points, and measuring the density of points that fall within intervals of distance *bw* from each. This is computed from an interpoint distance matrix represented as a histogram with bin widths *bw*, but it is easier to understand with an autocorrelogram. An autocorrelogram shows the distance and orientation of points from each other within some radius *r*. The overlay of point positions relative to one another is broken up into concentric annuli of equal width to measure the density of points per annulus - which is equivalent to the DRP. In Figure 3.1 the autocorrelogram of example observed and random and spaced S-mosaics are shown.

The critical metrics calculated from the DRP are the Effective Radius and the Packing Factor. Effective Radius (ER) is roughly the radius of consecutive bins from $d = 0$ that are significantly low (if any), a distance referred to as DRP distance (DRPD) in Cooper 2016a. It is computed with the assumption that the exclusion zone being measured is *highly* exclusive. When this is the case, it is assumed that points falling within DRPD indicate that the exclusion zone's radius *actually* falls between (DRPD – *bw*) and DRPD. To account for this, ER is calculated as DRPD minus a factor that increases with the density of points within DRPD to avoid overestimation.

Packing Factor (PF) is calculated as the squared ratio of ER to the estimate of the maximum exclusion radius possible, MR. Rodieck 1990 calculates this as the largest radius a group of circles (or spheres, if 3D) can have to fit in a square area (or cubic volume) given the number of them per unit of space - their density.

4.2.3.2.2 TWO-POINT CORRELATION ANALYSIS (2PC)

Two-point correlation (2PC) is a spatial point process that quantifies the similarity of two distributions of inter-point distances by computing the correlation between them. This analysis was developed by astronomers[66,67] to describe the spatial characteristics of galaxy clusters, and applies generally to

analysis of spatial coordinate data. For our purposes, we applied it as an alternative to DRP to measure the S-exclusion zone.

Like DRP, 2PC is computed from the inter-S-cone distance histogram, which can be visualized as an autocorrelogram. While DRP measures the density of S-cones within intervals of distance *bw*, 2PC measures the similarity between the number of S-cones found within each distance interval and randomly arranged point distributions. These random point distributions are distinct from the random *S-mosaics*, in that the points can be localized to any point in the 2D space of the ROI rather than being constrained to the observed positions of cones.

2PC is computed as follows: For an S-mosaic of interest, the test data, the distance between all *n* S-cone coordinates is represented as a histogram with bin widths *b*, *T*(*d*), where *d* is distance. A population of 100,000 uniform-random point distributions are generated within the same rectangular area as the ROI of interest with *n* points each, and each of these is represented as a histogram with bin widths *bw*. For each bin *i*, the mean across the 100,000 uniform random interpoint distance histograms is calculated, <*R*(*d*)> - 1. The 2PC is then simply the ratio of the counts per bin of *T*(*d*) against <*R*(*d*)> minus 1. This results in 2PC values per bin that are 0 at distances where a test distribution has the same number of cones as the average uniform-random point distribution. The value is negative if there are fewer points, with a minimum of -1 indicating the test distribution has no cones distance *d* away from each other. The upper bound of the 2PC value is determined by *n*, with an upper limit of *n*^2 which would occur in the first bin if all points were within distance of d_1 from each other.

EQUATION 3.1: TWO-POINT CORRELATION (2PC)

$$C(d_i) = \frac{T(d_i)}{< R(d_i) >} - 1$$

To determine whether a test mosaic is significantly different from a random distribution, we generate 100,000 random uniform point distributions, each represented as an individual inter-cone distance histogram *R(d)*. The mean of these, <*R*(*d*)> is calculated. The 2PC of each individual *R*(*d*) is then correlated against <*R*(*d*)>, and the Poisson 95% confidence interval is computed for each bin (shown in purple shade in the 2PC plots of Figure 4.5). Where *T*(*d*) is lower than the *R(d)* confidence interval, there

are significantly fewer points than a random distribution, and vice versa. Three metrics are calculated from the 2PC: Exclusion Radius (ExR), Exclusion Factor (ExF), and Exclusion Strength (ExS).

The Exclusion Radius (ExR) is the radius from the S-cone coordinate within which the 2PC is less than the 2.5th percentile of *R(d)* 2PCs, shown by horizontal green lines in Figure 4.5. The Exclusion Factor (ExF) is calculated as the squared ratio between the ExR and the empirical maximum radius (eMR – see 3.2.3.2), given the cone density and rectangular ROI bounds. Finally, if the ExR is nonzero, the Exclusion Strength (ExS) is calculated as the absolute value of the mean 2PC between 0 and ExR. Values averaged to calculate ExS are shown as vertical hyphenated green lines in the 2PC plots of Figure 4.5.

4.2.3.2.3 CONSIDERATIONS FOR BIN WIDTHS IN DRP AND 2PC ANALYSES

Using a constant bin width for DRP and 2PC analysis would lead the resolution of the ExR metric relative to the spacing between cones to vary with cone density, which varies widely across ROIs (see 3.3.1 and Appendix B 3.1). The cone sampling across these ROIs also varies considerably. Choosing a sensible bin width proved to be a non-trivial problem. The thought process we went through is described below..

Rodieck provided an approach to select the smallest bin width that satisfies a given confidence threshold. The density of cells of interest (S-cones, in our case) and the number of them sampled are computed with a desired “reliability factor” to output a bin width. The reliability factor is in arbitrary units and becomes more conservative the higher it gets with larger bin widths. Rodieck suggested a range of 4-6 to achieve a reliable result. This method was crucial to use of DRP as Rodieck had presented it, where the ER was determined by the density of points within certain distances relative to their overall density.

Applications of DRP to analyze S-cone topography added the use of random arrangements, Monte Carlo simulations, to assess confidence in the result, citing Diggle et al 1983. Our random S-mosaics follow this convention, where cones are randomly selected from the total cone mosaic. Crucially, the random S-mosaics are subject to the same sampling constraints, edge effects, and underlying cone-mosaic geometry as the test S-mosaic. By computing the DRP for these random mosaics, we can more accurately determine whether a test S-mosaic varies from the spatial characteristics of random ones than if we simply referred to the overall S-cone density. The Monte Carlo tactic is used in all instances of DRP analysis for human and macaque S-cone topography. In these, Rodieck’s reliability factor was still applied to select bin widths (see Discussion for more detail). We argue that Rodieck’s significance level

was an appropriate precedent to follow in previous studies, but that there are complications in its use for S-cone data and comparative studies that have not been fully considered:

Complication 1. Unlike the cell mosaics that Rodieck developed DRP to study, the S-cones are only a sparse subset of the cells making up the continuous mosaic of photoreceptors. The density of S-cones is important to consider, but so is the density of cells overall. We consider the regularity of the S-cones to be the spatial characteristics that make their arrangement distinct from that of an equal number of cones selected at random. In this framework, the smallest S-exclusion radius would be one that results in S-cones being unlikely to occur next to each other. If the bin width used is larger than the distance between neighboring cones, the first bin of DRP will include cones further than the first neighbor, and this immediate-neighbor S-exclusion zone radius would be obscured or missed entirely. Because the distance between neighboring cones varies drastically across the retina with cone density, the density of all cones should be taken into consideration to decide the bin width.

Complication 2. The minimum required S-cone sampling to apply DRP has never been investigated. For any metric, there is a minimum sampling needed to be able to make a statistically significant determination. In the case of DRP and other binned analyses, the minimum sampling is influenced by the bin width. Because the first bin of the DRP represents the smallest annulus area surrounding S-cones, it will be particularly sensitive to the effects of under-sampling.

Complication 3) Packing Factor is relied upon for its density-independence, demonstrated in Rodieck et al 1990. While it is true that the metric of Packing Factor is dimensionless and in that respect is density-independent, it *is* dependent on density in the sense that it is calculated from ER, which is calculated with a bin width determined from point density. If that density-dependent bin width is too large to capture the exclusion radius of interest, the ER and downstream PF are affected.

Regarding the first complication, we decided that the distance between neighboring cones was a vital factor to consider. To do this, we measured the average distance between neighboring cones, µINDa, which increases nonlinearly with cone density (Figure 3.4). We reasoned that 1) bin widths larger than µINDa risk failure to detect an S-exclusion zone if it extends only to the radius of neighboring cones, and 2) scaling bin width by µINDa across ROIs should normalize the balance of cone sampling per annulus.

The second complication of determining a minimum sampling of S-cones for binned analyses is more difficult to solve. We reasoned that the minimum number of cones needed to reliably calculate the

exclusion zone would depend on numerous factors that vary considerably across ROIs, including: bin width, the variability distance between neighboring cones, S-cone proportion, and the unknown characteristics of the S-exclusion zone we seek to measure, namely, its radius and strength. We reasoned that given any mosaic with an S-exclusion zone, there would be bin widths too small and too large to capture the S-exclusion radius dependent on these many factors. If we can identify bin widths that satisfy this sweet spot, we can identify a reasonable choice that balances detection of the S-exclusion zone with resolution of the analysis. We describe this approach in 4.2.4.1

In these analyses, we did not calculate whether the DRP ER was significantly lower for test S-mosaics (observed, spaced, d-min) versus random S-mosaics on a bin-by-bin basis, as in the case described in the third complication. Rather we followed Rodieck et al 1990's convention for calculating the ER (by comparison to the overall density of points being measured), then tested whether the test ER was greater than the 95th percentile of the random S-mosaic ERs, as done in Martin et al 2000, Roorda et al 2001, and Cornish et al 2004a. The calculation of the 2PC *does* require a bin-by-bin statistical test to define its ExR. The test 2PC value at each bin is compared to the Poisson 95% confidence intervals of the random-uniform distribution 2PCs at that bin (the purple shade of Figure 4.5).

Finally, the issue of Packing Factor's indirect density dependence will be mitigated in our approach by appropriately considering the sensitivities and limitations of the ER calculation, as we have attempted to do in our approach.

4.2.4 Computational Experiments

4.2.4.1 Testing bin-width dependence of detection and accuracy of the 2PC ExR metric

To simplify the problem of representing all relevant factors for our specific use case of determining appropriate bin widths for our 24 ROIs, we performed a simulation experiment that tested the performance of 2PC analysis to detect and estimate the ExR of simulated semi-regular mosaics with known S-exclusion zone characteristics generated across the 24 ROIs. DRP was not included in this experiment because we had determined from preliminary analysis that 2PC was more sensitive to DRP in several instances (not shown) and chose to save computational time.

We created four such populations of simulated mosaics using an algorithm slightly modified from the "d-min model" described by Galli-Resta et al 1999 to model the semi-regular arrangement of S-cones in ground squirrel retinae. Four varieties of d-min mosaics were produced by permuting combinations of

parameters that influence the S-exclusion zone, such that there were two types with ExRs of 2 arc-min, two with ExR of 2 µINDa, two with ExS of 1, and two with Exclusion Strength < 1.

We hoped to be able to determine whether the true human S-exclusion zone is constant across the area of the retina where it is present, or whether it varies with cone density. Setting the ExR to 2 arc-min or 2 µINDa allowed us to assess how the 2PC ExR metric's results might appear in one case or the other. These imposed ExRs were chosen because these are roughly the same at the lowest eccentricity ROIs, and because we had measured 2PC ExRs of 2 µINDa for these ROIs in preliminary analyses using a bin width of µINDa.

The two levels ExS were imposed on d-min S-mosaics because we wanted to assess the sensitivity of the 2PC ExR in the condition where an S-exclusion zone of that radius should be most detectable by having a maximum ExS of 1, and how this performance might decrease in a condition with an ExS < 1.

100 each of the 4 d-min S-mosaic types were simulated within each of the 24 ROIs. Each S-mosaic produced was analyzed with 2PC analysis with bin widths spanning factors of 2 arc-min and 2 µINDa (see Figure 4.3.6) We expected that bin widths that were factors of 2 arc-min would produce more accurate results for the 2 arc-min ExR d-min mosaics, and vice versa, and wanted to understand how 2PC ExR performance is affected when the bin width is not a factor of the true ExR. A major concern for us was whether the possible error in 2PC ExR results would be too large to confidently interpret how the true ExR varies across the retina and between subjects. In addition to informing our choice of bin widths for 2PC and DRP analysis, this variable space would give us some indication of whether the ExR estimates had sufficient precision and accuracy of the ExR estimates to convey reliable information about variation in the S-exclusion zone across the retina.

2PC analysis was also performed for the 24 observed S-mosaics with the suite of tested bin widths. We knew from the preliminary analysis that at the lowest eccentricities, where µINDa is roughly 1 arc-min, the ExR measured with a bin width of µINDa is 2 µINDa for observed S-mosaics and all four d-min types. We also knew the results for the two ExR conditions of d-min mosaics (2 arc-min and 2 µINDa) ought to diverge with increasing µINDa. Then, we would be able to see whether the observed results varied more like one ExR condition than another across binning tests.

4.2.4.2 Comparing representation of the S-exclusion zone and S-mosaic regularity across methods

From the d-min simulation experiment we determined a set of bin widths that were best able to represent the different types of S-exclusion zones. We used each of these for DRP and 2PC analysis applied to all observed and spaced mosaics. SVT and CRA metrics (bin widths not applicable) were also calculated. The number of ROIs where observed and spaced S-mosaics were found to have significant S-exclusion zones were compared for DRP, 2PC, and CRA to determine relative detection-sensitivity. The S-exclusion zone properties calculated with each analysis were compared across ROIs to assess how the pattern of S-cone topography across the retina appears differently with each method (see 3.3.1).

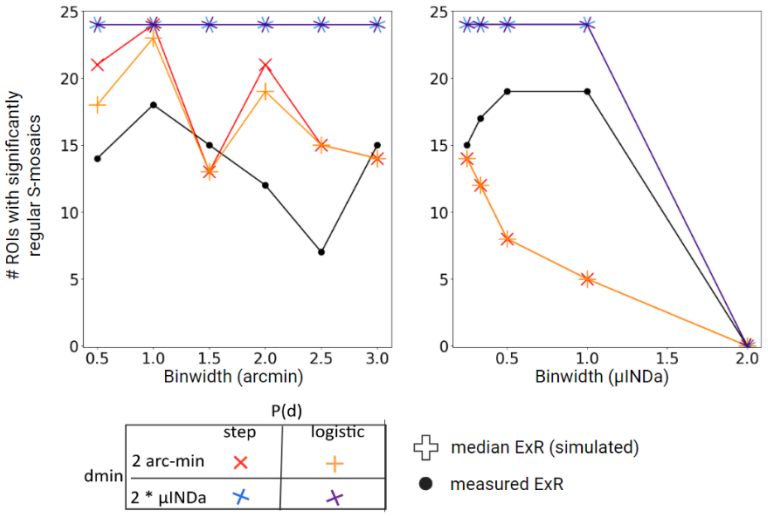

Figure 4.6. Bin width influence on 2PC. Sensitivity of the 2PC ExR to detecting the exclusion zone of simulated d-min S-mosaics and observed S-mosaic with different bin widths. For every bin width tested, the number of ROIs where >95 of the 100 simulated mosaics had a 2PC ExR significantly greater than random mosaics is reported (colored crosses), while the observed result is shown with a black dot.

SVT metrics do not describe the S-exclusion zone, but have been used to describe S-mosaic regularity many times in the past. Previous meta-analysis of cone topography metrics have thoroughly evaluated Voronoi regularity metrics applied to the total cone mosaic, but not the S-mosaic. We wanted to appreciate how the differently spaced and observed S-mosaics would be represented from random mosaics using these metrics to better contextualize previous findings.

4.3 Results

4.3.2 Identification of reasonable bin widths for DRP and 2PC analysis

Results of 2PC analysis with different bin widths performed on the 4 populations of d-min mosaics were

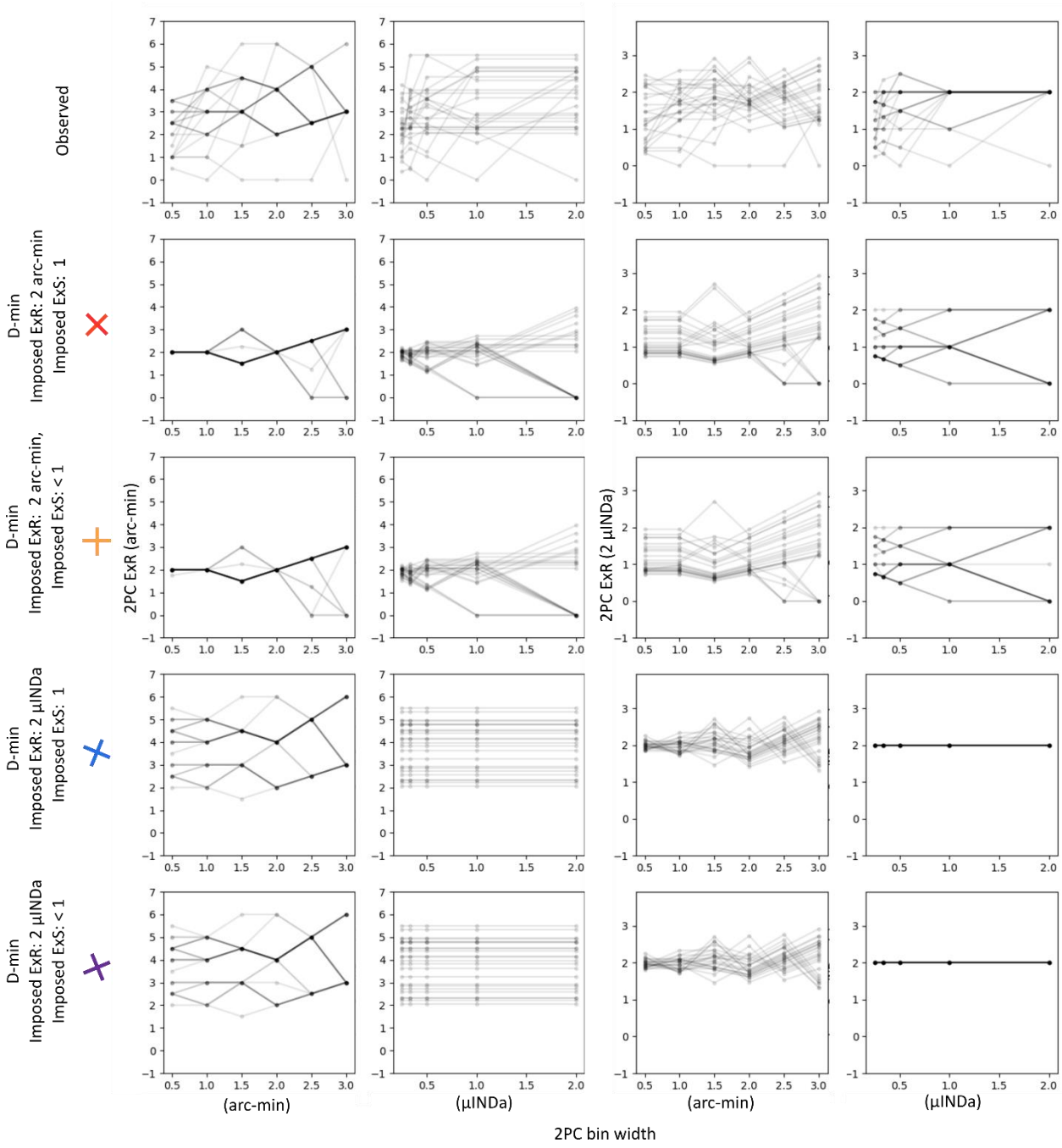

Figure 4.7 2PC ExR results for Observed and D-min mosaics across 2PC bin widths. Row 1) Results for observed S-mosaics. Row 2) d-min = 2arc-min, step function. Row 3) d-min = µINDa, step function. Row 4) d-min = 2arc-min, logistic function. Row 5) d-min = µINDa, logistic function. Bandwidths tested were 0.5, 1, 1.5, 2, 2.5, and 3 arc-min (1st & 3rd column), and 0.25, 0.33, 0.5, 1 and 2 µINDa (2nd & 4th column). The y-axis Is in units of arc-min in the 1st and 2nd column, and in terms of muINDa in the 3rd and 4th column. The median result for the 100 d-min mosaics made for each ROI using each bin width is plotted as dotted semitransparent lines across the bin widths tested.

used to determine reasonable bin widths. Figure 4.7 shows the number of observed ROIs with significant 2PC ExRs detected across d-min population types, and the number of ROIs for each d-min type where >= 95 of the d-min S-mosaics were significantly different from random. Figure 4.7 shows the observed 2PC

ExR measured across bin widths (top row), and the median 2PC ExR of the 4 d-min populations (bottom four rows).

Of bin widths tested, we found 1 arc-min, 0.5 µINDa, and µINDa to be best suited to detecting and describing the S-exclusion zones of the four d-min populations. Unsurprisingly, we found that the bin widths that were factors of 2 arc-min were best suited to capturing 2 arc-min ExRs, and likewise for bin widths in terms of µINDa and the 2 µINDa ExRs. We were disappointed to find that while we could tune the bin-width to maximize detectability of the S-exclusion zone, the variance of results even within the reasonable bin widths produced so much variance about the ExR estimate that we could not say confidently how the ExRs varied across the retina. Without a-priori knowledge as we had for the D-min experiment, we couldn't confidently choose an appropriate bin width for the observed. The finding that the bin width problem was not necessarily solvable led to the advent of CRA analysis.

4.3.3 Relative sensitivity of DRP, 2PC, and CRA to the human S-exclusion zone

We found that the observed S-exclusion radius measured with the 2PC ExR was more sensitive to the S-exclusion zone of both real and spaced mosaics than DRP ER. DRP ER results more variable than that of 2PC ExR for spaced and random mosaics within mosaic-sets, as we intuited. The dramatically more variable random mosaics and slightly lower observed DRP ERs made them less sensitive to the S-exclusion zone than the 2PC analysis.

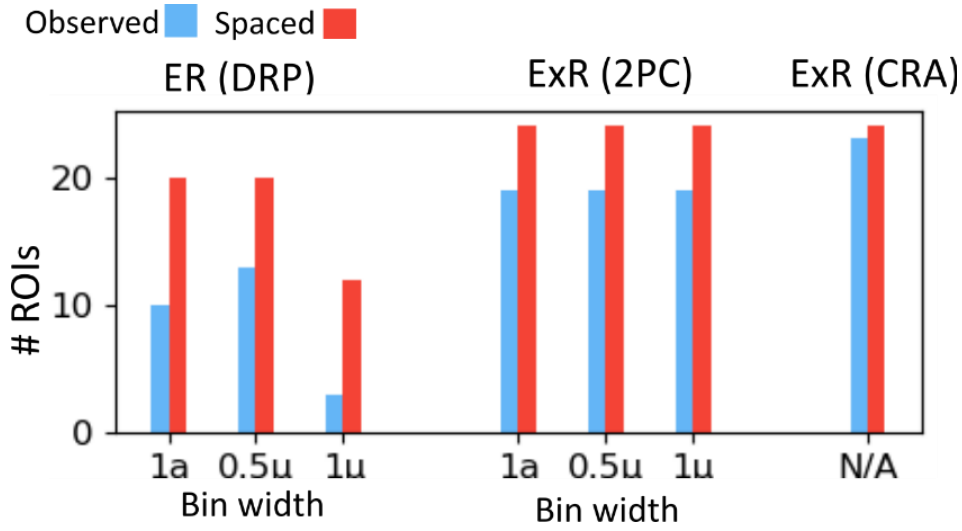

CRA's ExRr, which indicates the number of concentric rings surrounding S-cones that have significantly fewer S-cones than do random S-mosaics,

Figure 4.8 Number of ROIs with S-exclusion zone detected using DRP, 2PC, and CRA. **Observed** S-mosaics of 24 ROIs were analyzed with DRP, 2PC, and CRA analysis to determine whether an S-exclusion zone was present. DRP and 2PC analyses were performed with bin widths of 1 arc-min, 0.5 µINDa, and µINDa. The counts of number of ROIs with S-exclusion radii using each analysis are shown for observed (blue) and spaced (pink), n =24).

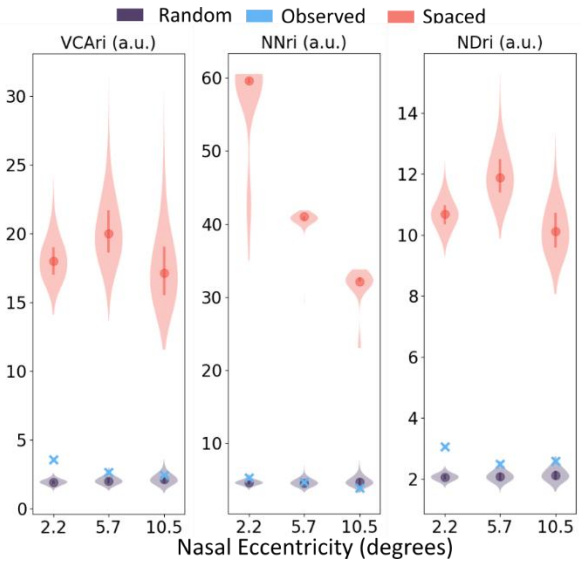

Figure 4.9 S-mosaic Voronoi Tessellation metrics. Topography metrics calculated for observed and simulated S-mosaics across the nasal meridian of S2 are shown: VCAri, NNri, and NDri. Simulated population results are shown as violin plots (n=1000, each), with dots at the median and lines spanning the 50% confidence interval.. Observed results are marked with an 'X'. Color indicates whether the S-mosaics are observed (blue), random (purple), or spaced (pink).

proved to be the most sensitive to the S-exclusion zone. 23 of 24 Observed S-mosaics had detectable S-exclusion zones in this paradigm, and all spaced S-mosaic exclusion-zones were detected.

The sensitivity of metrics to the S-exclusion zone is summarized Figure 4.8, showing the number of observed and spaced (1 per ROI) S-mosaics with S-exclusion zones detected using each method.

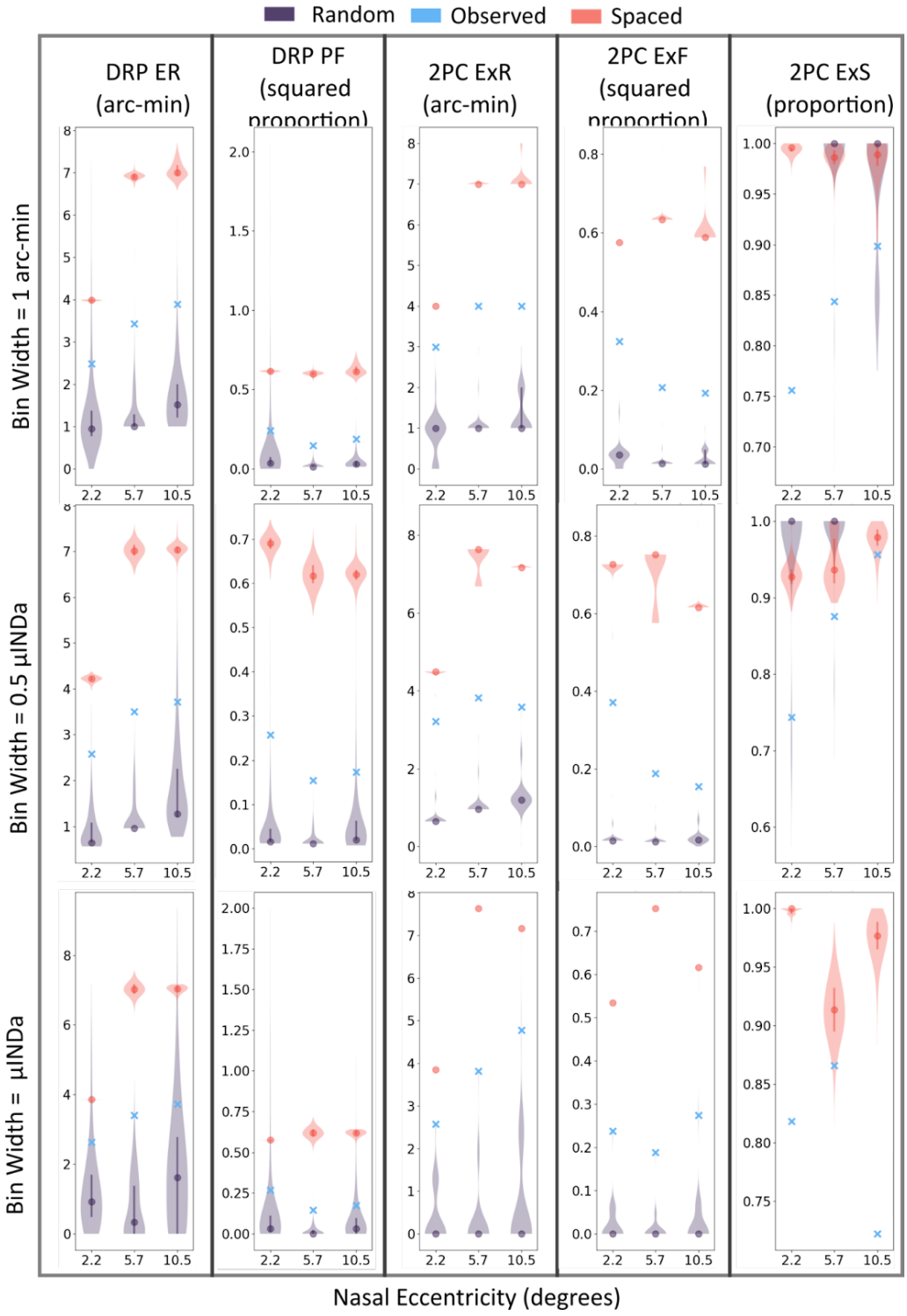

Figure 4.10 DRP and 2PC metrics. Topography metrics calculated for observed and simulated S-mosaics across the nasal meridian of S2 are shown:, ER and PF of DRP analysis, and ExR, ExF, and ExS of 2PC analysis. Simulated population results are shown as violin plots (n=1000, each), with a dot at the median and a line spanning the 50% confidence interval. Observed results are marked with an 'X'. Color indicates whether the S-mosaics are observed (blue), random (purple), or spaced (pink).

4.3.4 Differences in the representation of the S-mosaic regularity across the metric battery

SVT metrics proved poor for detecting differences from random mosaics, and instead appear to be sensitive to degradation from high regularity. Regularity indices of spaced mosaics tended to be ~10x higher than that of random distributions and highly variable, despite the uniformity of spaced mosaic spatial characteristics. Results for observed mosaics, tended to fall within the random distributions, with some exceptions, meaning there is roughly an order of magnitude's difference in regularity between observed and spaced mosaics measured by SVT metrics. Figure 4.9 demonstrates this pattern in the value ranges calculated for VCAri, NNri, and NDri for ROIs spanning the nasal meridian of S2.

2PC ExR results measured with bin widths of µINDa were most similar to the median CRA ExRa of our tests (not shown). While many of the observed DRP ER results were not statistically significant at this bin width, they did generally produce nonzero ExRs. In Figure 4.10 the DRP ER and 2PC ExR are plotted against the median CRA ExRa. Interestingly, we see that these 2PC ExR and DRP ER values tend to fall at high and low ends of the CRA ExRa measured for a given mosaic.

Generally, the non-significant DRP ER values fully obscured the presence and patterns of the S-exclusion zone described with CRA in Chapter, primarily due to their tendency to be indistinguishable from random results. 2PC results with bin widths of µINDa replicate patterns observed with CRA analysis, but

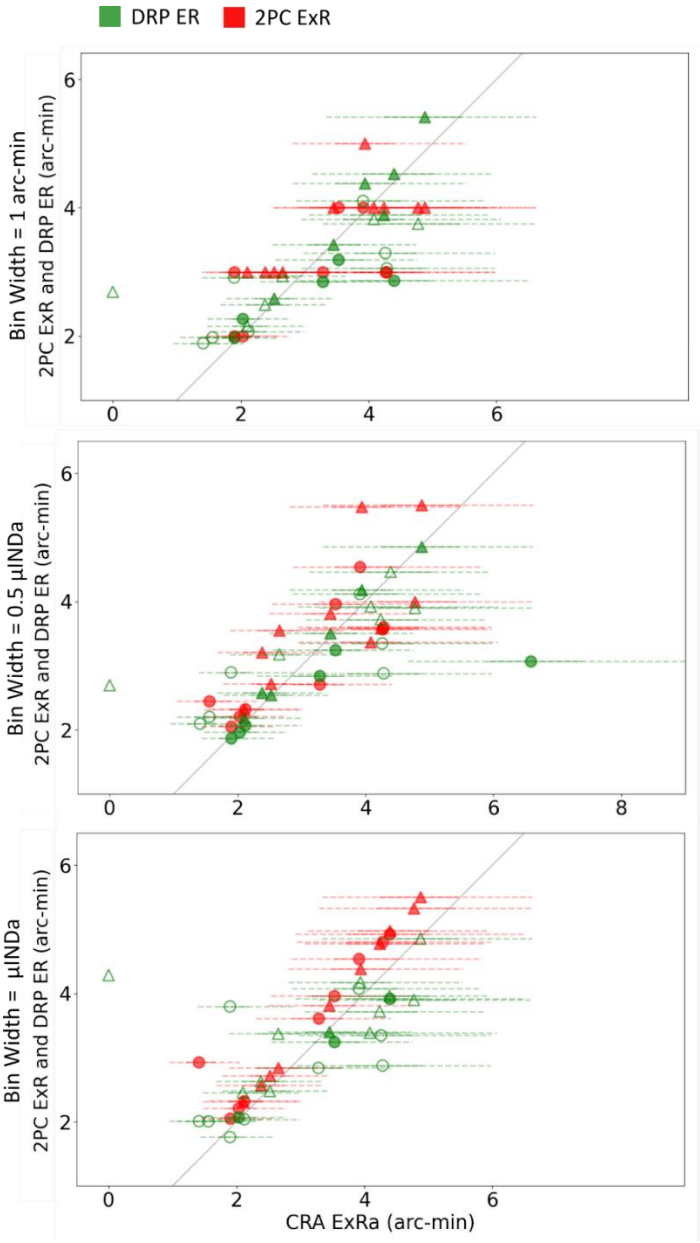

Figure 4.11 ExR represented with DRP, 2PC, and CRA. DRP's ER and 2PCs ExR (calculated with bin width of µINDa) are plotted against the ExR of CRA. Confidence intervals for the CRA ExRa are indicated by solid (25th-75th percentile) and dotted (2.5th-97.5th percentile) lines. Markers are filled where the DRP or 2PC exclusion radius was significant, otherwise unfilled. Gray line indicates unity.

without CRA analysis we wouldn't have a basis to say whether these patterns were real or artifactual due to the observed variability of results in the d-min experiment.

4.4 Discussion

We found that the application of DRP as described by Rodieck and employed in two previous S-cone topography studies was not able to reliably describe the S-exclusion zone. DRPD, the second to last step in calculating the DRP ER, would be expected to outperform ER because it lacks the factor that reduces DRPD by a factor inversely proportional to presence of S-cones within the DRPD. However, the statistical test against random uniform point distributions used in the 2PC gives the approach an additional benefit of constraining the results for 2PC analysis to lower values, which makes it more likely that non-random regularity can be detected.

While we did not find bin widths of µINDa to be sufficient to describe the S-exclusion zone with the precision we wanted, we did find the guiding principle of binning by factors of µINDa <= µINDa proved useful for capturing the 2PC ExR of S-mosaics that scale with µINDa. Others may find this strategy of balancing cone-sampling per bin in areas varying vastly in cone density useful in their applications. We also appreciate the descriptive power of the 2PC analysis, as it literally

describes the similarity of the test point distribution to a random distribution. We found this allowed for more intuitive, meaningful comparisons between ROIs that vary in density than the DRP.

Other specifics of the DRP analysis applied and data sampled may have further limited the ability to detect the zone, including 1) use of Gaussian statistics rather than Poisson and non-parametric statistics where appropriate, 2) inadequate sampling of S-cones, 3) disruptions in cone classification due to blood vessels in in-vivo imaging techniques, and 4) tendencies for false positive and false negative identification of S-cones. These possibilities were not tested exhaustively in this meta-analysis and are discussed in more detail in 3.4.

We would advise the following for those going forward with DRP analysis to assess the S-exclusion zone: 1) Use bin-widths no larger than μINDa, 2) apply Poisson statistics in bin-by-bin tests against results of random S-mosaics, 3) apply non-parametric statistics in comparisons of ER between test and random S-mosaics, and 4) consider the DRPD as a liberal alternative in addition to conservative estimate of ER.

Given the detection sensitivity results and the demonstration of CRA's descriptive power in chapter 3, we emphatically suggest that this method be considered for S-exclusion zone characterization going forward. However, the accuracy of CRA depends on the quality of cone finding in the ROI. Missing cones in the mosaic leads to inaccuracy in neighboring-cone identification that compound with increasing concentric rings around a given cone.

DRP on the other hand has been shown to be relatively insensitive to missing cones and can be a better choice where cone-finding is not reliable (see example in Appendix C). We have not tested explicitly that 2PC shares this benefit, but there is no obvious reason it would not. Future work will continue to tease out the strengths and weaknesses of each approach over the other. Importantly, none of these metrics are suited to measuring patterns that are not radially symmetric.

5: Independence of the S-mosaic

5.1 Introduction

"Independence" of the S-mosaic is the idea that S-cones follow a distinct developmental program from non-S cones in the maturation of their spatial patterning in the retina. This hypothesis is supported by several studies that assessed the spatiotemporal characteristics of photoreceptor differentiation and migration across types and the mature topography of S-cones relative to non-S-cones in the retina.[28,35,41,42,44] Under this paradigm, the mature photoreceptor topography results from mechanisms separately governing differentiation and migration of S-cones and non-S-cones. In the spatiotemporal overlap of the two developmental programs, traces of the independent processes leave traces in the spectral topography. This is distinct from a hypothetical system in which undifferentiated photoreceptors first migrate to comprise a mosaic, with that preceding topography shaping differentiation of the photoreceptor.

Previous work describing independence of the S-mosaic in humans is detailed in Chapter 1. Briefly, evidence supporting independence of the S-mosaic has been found in the mature human retina with Voronoi topography analyses. Ahnelt et al 1987 and Curcio et al 1991 reported that in the periphery, S-cones occasionally abut non-S cones while non-S-cones always had rods between each other. Ahnelt et al 1987 also found an instance where S-cones had significantly more distant neighbors than non-S-cones centrally. Hofer et al 2005 reported a significantly higher standard deviation for S-cone neighbor distances than for non-S-cones, without assessing whether it was skewed high or low. Early work reported that S-cones were more likely to have >6 neighbors, or to be one of the neighbors of a non-S-cone with >6< neighbors,[41,42,44] but S-cones have been found to have the same distribution of number-of-neighbors in studies where S-cones were classified with anti-S-opsins[35] or functional imaging.[28,29]. These marks of S-mosaic independence are thought to disrupt the more regular packing arrangements of non-S-cones.

No study has performed either number of neighbors (NN) or neighbor distance (ND) analyses on more than 3 ROIs of an individual human retina. This and differences in methodology for S-cone classification make it unclear whether disagreement between studies reflects true variability or experimental artifact. Our large dataset of spectrally classified ROIs across the central retina provided an opportunity to fill in these gaps.

We did not find that S-cones had a different distribution of number of neighbors than non-S-cones in any region sampled but one, consistent with Curcio 1991, Roorda 2001, and Hofer 2005. However we did find a stark, robust prevalence of S-cones with significantly far neighbors in the foveal slope and S-cones with significantly near neighbors more peripherally. These features are consistent with the hypothesis that the mechanisms governing the mature S-mosaic within the total photoreceptor mosaic is separate from that of non-S-cones. We hypothesize that the shift from far to near S-cone neighbors may hinge on the shift in balance between cone and rod density.

5.2 Methods

5.2.1 Subjects & Classification

In these experiments we analyzed the same spectrally classified data described in Chapter 3, S1 and S2. Data re-analyzed from previous literature in Chapter 3 is not included here. The 24 ROIs spanning the central ~1-12° of S1 and S2 are shown and detailed in Appendix A and Appendix B Table 3.1, respectively.

5.2.2 Analysis

To assess the independence of the S-cone sub-mosaic, we used the all-cone Voronoi tessellation (AVT, see 3.2.4.1) to observe the number and distance of neighboring cones surrounding S- versus non-S-cones. For both number-of-neighbors (NN) and neighbor-distance (ND) analyses, statistics were calculated with left- and right- tailed Mann-Whitney U tests to determine whether S-cone metric distributions were significantly low or high, respectively. For NN analysis, a left and right statistic was calculated for each ROI from the distributions of all neighbor types for the two groups. ND analysis, the tests were performed separately the *x*th nearest neighbors surrounding S- and non-S-cones, where $x = 1:6$.

5.3 Results

5.3.1 Number of cones neighboring S- .and Non-S- cones

Cones of each type averaged 6 neighbors in all ROIs, as expected. We generally found that the NN distribution spans 5-7 cones regardless of cone-type. A small minority have 4 or 8 neighbors, and in rare few cases 9. In one case, S2 superior 1.9, S-cones, S-cone NN was significantly high. S- and non-S- NN distributions for each ROI are shown as violin plots in Figure 5.1.

5.3.2 Distance of cones neighboring S- and Non-S- cones

We observed a split between central and peripheral ROIs such that in more central ones S-cones had significantly far neighbors and in more peripheral ones S-cones had significantly near neighbors. The division is stark when the presence of near and far neighbors is examined with respect to eccentricity, cone density, and µINDa (Figure 5.2), but not so with respect to the proportion or density of S-cones (not shown). S-cones have significantly far neighbors in all but one case more peripheral than 3°, with fewer than 2000 cones per square degree and µINDa greater than 1.5 arc-min µINDa (Fig 5.2B, top row). They have significantly near neighbors nearly all cases more central than 3°, and in all cases with > 2200 cones per square degree and µINDa less than 1.4 arc-min (Figure 5.2 B, bottom row).

ND distributions are shown in Figure 5.2 A for ROIs along the temporal meridian in S1, which exemplifies the shift in tendency for far versus near S-cone neighbors: at 1.5°all the 6 nearest neighbors are likely to be significantly near. This is the only ROI where all six are significantly near, and notably also the ROI with the highest cone density and lowest µINDa. None are significantly far at 3.8°, but the nearest two are significantly near. At 10.18 °, five of the nearest six neighbors are significantly near.

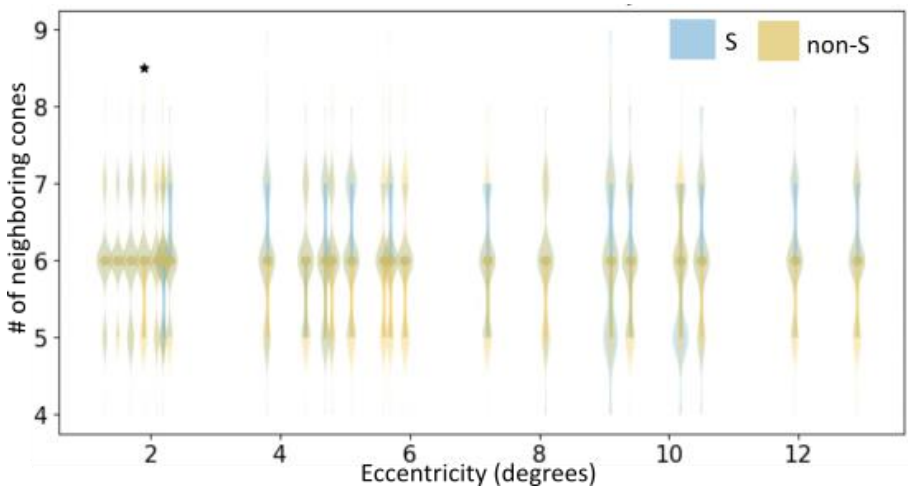

Figure 5.1 Number of Neighbors (NN) analysis. The distribution of numbers of neighbors surrounding S and LM cones are shown in blue and yellow violin plots, respectively, for each ROI with eccentricity. In 23 of 24 ROIs, the two distributions were not found to be significantly different. In one (S2 Superior 1.5 °) the S-cone distribution

5.4 Discussion

5.4.1 Independence of the S-mosaic

We found evidence that supports the S-cone mosaic's independence from the non-S mosaic; that they are more likely to have slightly further neighbors at eccentricities < 3° and to have nearer neighbors at eccentricities > 3°. This pattern has not been reported previously, and may provide some insight into the development of the mature photoreceptor-mosaic topography. We know that S-cone opsin is expressed

prior to L- and M- opsins, and S-opsin expressing cells are the first photoreceptors to populate the prenatal retina, followed by non-S-cones, then rods. This finding would suggest that the S-cones are at least somewhat locationally stable in the midst of non-S-cone and rod infiltration (though it does not preclude some degree of lateral migration of the S-cone intersections due to other cell types' migrations).

We do not know what leads to the transition from significantly far S-neighbors at lower eccentricities and significantly near ones more peripherally. The presence of rods hinging the difference is our leading hypothesis at this time. Where rods are high in density, they consistently occupy space between non-S-cones like tile grout, due to an unknown mechanism. Whatever that mechanism is, it does not seem to apply to S-cones, given the consistent observation that S-cones lie significantly near and even abut each other at higher eccentricities

If the absence of a between-cone rod-filling mechanism with respect to S-cones *is* the cause for significantly nearer S-cone neighbors in the periphery, it makes sense that the phenomenon would diminish and cease as rod density decreases to zero approaching the fovea. We have not explicitly evaluated the presence of rods across ROIs in these data (mostly due to imaging limitations), but the radius within which S-cones have significantly far neighbors, ~2-3 degrees, is consistent with the region where cones dominate the retina. Here, we hypothesize that the S-mosaic has *far* neighbors because of the S-mosaic's stability (independence) during (at least the late stages of) centripetal non-S-cone migration. In this framework, the non-S cones are packed increasingly more densely and regularly approaching the fovea as they follow their independent migration programs, and their pattern is disrupted by the non-budging S-cones.

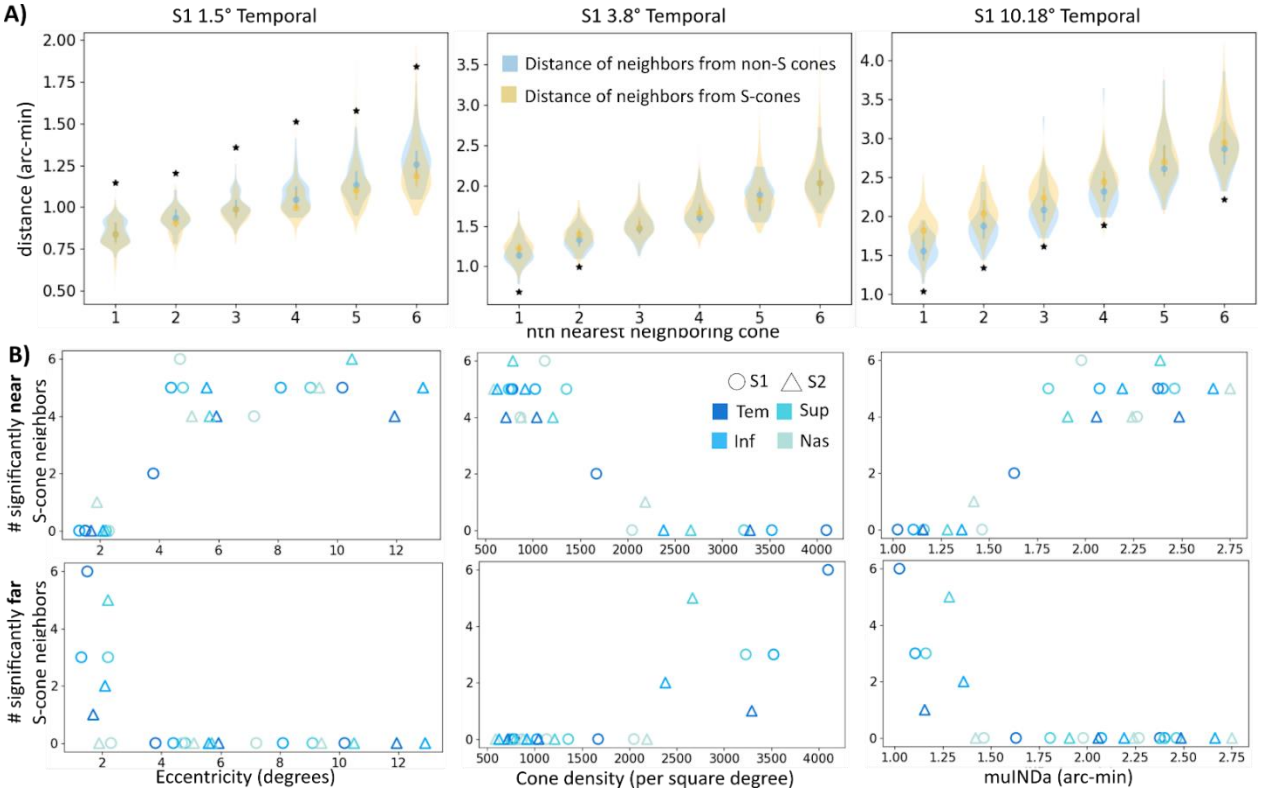

Figure 5.2. Distance of neighboring cones. A) For ROIs S1 temporal 1.5deg and 10.2deg, distributions of the distance of the 1st-6th nearest neighbors surrounding S and non-S cones are shown as blue and yellow violin plots, respectively. The medians are dotted with lines spanning the 50% confidence interval. A star below a pair of S- and non-S- cone distributions indicate the S-cone distribution is skewed significantly lower, while a star above indicates it is skewed significantly higher. In S1 1.5° Temporal, S-cones are significantly far from their 6 nearest neighbors. At 3.8° the nearest two neighbors of S-cones are significantly near, and at 10.2°all but the 5th nearest neighbors are significantly near. B) the number of significantly near and far neighbors surrounding S-cones are plotted against Eccentricity, cone density, and µINDa. Shapes indicate subject, and shades of blue indicate meridian. ROIs with significantly near S-cone neighbors are prevalent at eccentricities > 3° with cone densities greater than <1500 per square degree and µINDa > 1.5 arc-min. Conversely, ROIs with significantly far S-cone neighbors are found centrally < 3°, cone densities > 2000 per square degree, and µINDa < 1.5 arc-min.

We did not find that S-cones were more likely to have 5 or 7 cones than were LM-cones, as had been noted in macaque [Pum et al 1990] and human [Ahnelt 1987, Hofer 2005 (3 of 8 subjects)]. It is unclear whether this is due to individual differences or classification error. Ahnelt 1987 classified cones based on morphology, relying in part on the relatively large diameter of their inner segments near the inner-segment outer-segment junction (ISOS). It was later shown that morphological identification of S-cones in this manner is prone to false-positives, particularly in the central retina.

It makes sense that cones with larger inner segments would be more likely to exist at "discontinuities" of the cone mosaic and to have a higher propensity for >6 neighbors, simply because of their larger circumference. So, it's possible that identifying as S-cones influenced this finding with a circular logic. If this were the case though, it's unclear why the S-cones would also be prone to having <6 cones. Our data is not immune to false positives itself (see Chapter 2), and we would expect false positives to obscure slight differences in NN that might be meaningful.

Though we do identify evidence of the independent S-mosaic disrupting patterns of the non-S-cone mosaic, we do not know whether these discontinuities induce a "patchwork" of high-regularity tritanopic regions as speculated by Pum et al 1990. To determine this requires a separate analysis with respect to the interior angles of Voronoi cells, a tractable and promising direction next steps in this body of work.

6: Conclusion

6.1 Summary of findings

In total, this report shows that regularity of S-cone sub-mosaics extends nearer to the fovea than previously thought, details methodological limitations in measurement of the S-cone exclusion zone properties, provides novel metrics that outperform the classic approaches to characterizing the S-exclusion zone, and corroborates the independence of the S-mosaic. These results serve as an expansion in our understanding of human S-cone topography and a context for future experiments exploring retinal physiology and visual perception in these subjects.

6.1.1 S-exclusion zone characterization

This body of research characterizes the S-exclusion zone across the human central retina in two subjects, revealing a novelly described. The exclusion zone in the two subjects assessed were prominent from ~1-12°. Eccentricities as near the fovea near the fovea (~1-2°), have previously been found to be randomly arranged. We argue that rather than this discrepancy with our results necessarily reflecting variability in human retina anatomy, it could be explained by combinations of low cone-sampling, discontinuous cone-finding in classified images, deceptive bin-widths in spatial point processes, and weaknesses of the DRP approach in particular to the characteristic semi-regular pattern of S-cone topography. I found that the S-cone exclusion zone was present across the entire range of eccentricities tested, as far as ~12°, and with no differences across four cardinal meridians sampled.

Using our novel Concentric Ring Analysis (CRA), we identified an S-exclusion zone in 20 of 24 ROI. Of these, 20 had an exclusion radius of 2 concentric cone rings surrounding S-cones, and 3 had an exclusion zone of 1 ring. Re analyzed macaque and human S-mosaics from Roorda et al 2001 had the 2-ring S-exclusion radius as well.

Two novel, related approaches were used to measure the upper limits of S-cone regularity given the varying imperfect regularity of the cone mosaic across ROIs. One improved the estimate of the radius of a perfect triangular grids made up of the same density of points as an observed S-cones by taking into account the ROI aspect ratio and possible orientations of the grids. Based on the grids created to make that estimate, I was able to create simulated spaced S-mosaics that represented the upper limit of S-mosaic regularity possible given the imperfect lattice of cones the sub-mosaic exists within.

We defined a property of the S-exclusion zone that hadn't been identified previously, Exclusion Strength (ExS), which influences the regularity of an S-mosaic with an S-exclusion zone. We considered this factor in tandem with the classic regularity metric typically called Packing Factor (which we called Exclusion Factor, ExF), the squared ratio of the exclusion radius to the maximum it could be given the density of cones. Regularity in terms of the ExF increased with S-cone proportion, while ExS decreased. It is unclear without further analysis whether the ExS is truly decreasing as S-cone proportion increases, or if it is simply being underestimated at lower S-cone proportions.

In this body of work we learned the importance of cone density, the average distance between cones, and S-cone proportion are to describing and comparing semi-regular S-mosaics. Previously, S-cone density was the only other factor of cone topography that the S-exclusion zone had been related to directly. Given the result of the 2-ring S-exclusion zone in the reanalyzed macaque ROI of Roorda et al 2001, it seems macaque S-cone topography could be more similar to human than previously thought. A hypothesis we'd like to test is that S-cone proportion alone explains the difference in S-exclusion radius in terms of concentric rings.

Our results concerning the 2-ring pattern of the S-exclusion provides glues about the mechanisms governing the mature S-exclusion zone. From this we know that the ExR scales with the distance between neighboring cones which varies with cone and rod density. The result is inconsistent with the hypothesis that the S-exclusion zone is formed from an initially random arrangement of S-cones that are then separated during uniform expansion of the retina, and is more consistent with local interactions between S-cones leading to their lateral movement away from each other when they arrive in the photoreceptor layer.

From visual inspection of S-cone autocorrelograms we saw that the S-exclusion zone is not radially symmetric at the lowest eccentricities evaluated. In the ROIs where this was evident, the S-cone exclusion radius appears longer along the axis of the meridian the ROI is located along. The anisotropy is more evident along the nasal-temporal axis. The same horizontal oblong S-exclusion zone was visible in the reanalyzed macaque data of Roorda et al 2001.

This characteristic has not been reported previously, and is important to consider going forward. A Without quantitative analysis, we cannot determine whether the horizontal anisotropy is truly stronger, or whether reduced sampling or tricks of the eye obscures more peripheral and vertical-meridian

anisotropy, and the human ROI reanalyzed from Roorda et al 2001. (more detail below under “Taking S-cone topography analysis further”).

Combined, our novel approaches to analysis of the S-exclusion zone allowed thorough representation of S-exclusion zone metrics that revealed important patterns underlying semi-regular S-cone topography.

6.1.2 Independence of the S-cone mosaic

Our data corroborates previous findings S-cones disrupt the regularity of the LM-cones such that they are nearer or further from non-S cones than non-S-cones are each other. We saw a pattern to the phenomenon that has not been previously described. S-cones at eccentricities < ~ 3° were significantly likely to have non-S neighbors further than non-S-cones. Consistent with work since immunohistological and functional classification of S-cones, we did not find that S-cones are more likely to have > 6 < neighbors than non-S cones. It is unclear how the finding that S-cones disrupt in the former way reconciles with the literature which associates the medium-range disorder of the non-S-cone mosaic which was associated with large diameter cones with many or few neighbors (especially given that the wider diameter of the S-cone inner segment is well-supported in the literature and tends to be more reliable in the periphery where some of these observations were made).

While we know that S-opsin is expressed earlier than L/M opsin in immature cone cells, and that S-opsin expressing cells begin migration across the retina earlier than those expressing L/M opsin, little is known about how the factors governing their trajectories influence each other, if at all. The hypothesis of S-mosaic” independence” posits the S-cone distribution is minimally influenced by the barrage of non-S-cones infiltrating in the secondary wave of cone migration. If S-cones were nudged about as the non-S cones packed into the spaces around them, we would not expect the distance between neighboring cones to vary with cone type.

We believe that the observation of S-cones being occasionally closer to non-S cones at higher eccentricities and further at lower ones is consistent with S-cone positions relatively static with respect to migrating non-S-cones. However, it’s not clear how this approach reconciles with the tritanopic zone and the high-S-cone density ring surrounding it. It has been suggested that this could be the result of LM cones forcing S-cones out of the central retina, a point against S-cones holding static positions in the face of LM-traffic. It has also been suggested that there is a mechanism that prevents S-cones from completing their journey to the central retina, which remains unclear, too. Given our results showing

that S-cone topography is regular more centrally than previously recognized, the premise of S-cones becoming irregular (in the sense that there is no longer an S-exclusion zone metric keeping them apart) is brought in the question. We hypothesize that the transition from S-cones having significantly far to near neighbors could be related to shift in high cone to high rod density surrounding the foveal slope (see 5.4). Future topography analysis may allow us to test this.

6.2 Aspirations

6.2.1 Considerations for cone-finding and spectral classification

6.2.1.1 Cone finding

A prerequisite to classifying cones by spectral type is to locate their position in the cone-mosaic. We identify cones from images using an initial automatic cone-finding program followed by manual editing. The automatic cone-finding takes a cone-diameter as an input to create a gaussian filter that is 2D-correlated against the image. After this step, the user can add, remove, and move coordinates representing cone positions (see Chapter 2 Methods for more detail).

The automatic portion works best when image quality is high, rods are absent, and cone diameter is constant across the imaged field. In the AO-OCT-classified dataset described in this body of work, it is most difficult to automatically find cones at higher eccentricities where image quality is diminished and it is sometimes difficult to discriminate between rods and cones. While we have classified regions nearer the fovea than shown in these results, we did not include them in topography analysis because such a high proportion of cones are too small to confidently discriminate with our current resolution limits.

Missed cones in cone-finding influences topography analysis in a number of ways. Voronoi neighbors are mis-assigned, which leads to overestimation of µINDa and cascading inaccuracy for concentric-ring identification, and in turn can lead to underestimation of the exclusion radius. The regularity of the overall cone mosaic will appear lower than it is, and randomly arranged sub-mosaics will have more variable inter-cone spacing than they ought to. Sometimes, a cone appears to be multiple cones due to optical aberration, which also influences error in results. If this phenomenon occurs at the position of a single S-cone, it can lead to the unusual result of two S-cones near each other. The same is true for a rod misidentified as a cone (fairly likely if it is misidentified as a cone in cone-finding, because it will have a low response to the 660nm stimulus).

In Fig 6.1, the S1 2.2 ° nasal ROI is shown with visible putative cones left out in the cone-finding steps of our pipeline highlighted in red. There are also many dark “holes” lacking visible cones, some of which could be dysflective cones (see Chapter 2)

There are many promising avenues to overcome cone-finding limitations in AO-OCT imaging of the retina. In the Sabesan lab and others hardware and engineering advances are in the works to increase the quality and speed of both the imaging experiment and the processing pipeling leading up to spectral classification (see Chapter 2).

6.2.1.2 Cone classing

Chapter 2 describes a classification re-test experiment that provides estimates of uncertainty in our spectral classification. Mismatches in S-cone assignments across days were 1.5° and 1.6% at 4°, respectively. Given that S-cones make up 4-11% of S-cones in our data, these are non-negligible sources of error that could include false positive and negative S-cone classification. We don’t expect either to be

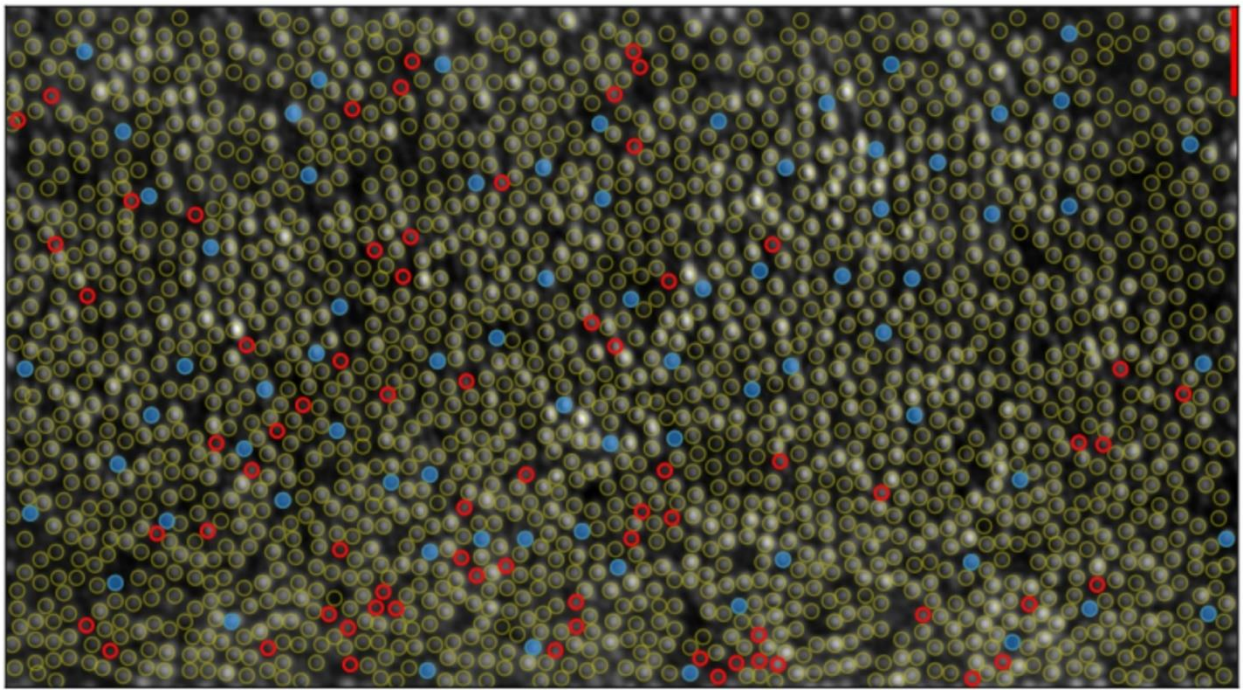

Figure 6.1 Example of putative missed cones in the S1 2.2° nasal ROI. Red line indicates 5 arc-min. Here, as in appendix A, cones classified as S are shaded in blue and cones that weren’t classified S are shaded in yellow (this includes cones that could not be reliably classified as L or M, either). In red, I’ve marked several areas that may be a cone missed in the pipeline of automatic and manual cone-finding. Rods are present but relatively few at this eccentricity and are not clearly visible. In other cases, it can be extremely difficult to distinguish between rods and cones by appearance.

spatially biased, though we don't know much about the spatial-temporal distribution of outer-disk shedding in the cone mosaic, if there are other factors influencing M or L cones to be mis-classed as S-type, or if torsion distortion in images bias misclassification to ROI edges. If false positives are not spatially biased, we would expect them to disrupt S-exclusion zones at random, which could decrease the ExR or make it undetectable. False negatives pose the same risk if S-cone sampling is low. There are several ways we can seek to increase confidence in the S-cone classification with AO-OCT.

1) Re-performing the ORG classification on a different day is a good way to build confidence, but is costly in terms of experiment time, data storage, and computation time. Furthermore, re-tests will not rescue misclassification of a non-functioning cone as S-type with a 660nm stimulus light.

2) One possibility is to have a positive-response test for the S-classification, such as what has been shown in Zhang et al 2019. Preliminary experiments have been performed by Vimal Pandiyan toward this goal, using a 420nm stimulus in place of 660nm. So far, it's proven difficult to separate S- and M-cones using this method in our apparatus. Although S-cones are more sensitive to the stimulus wavelength than M-cones, their delta-OPL response magnitudes to the S-selective stimulus overlap and cannot be reliably distinguished. This may have something to do with differences in S-cone morphology from L and M cones. L and M cones are extremely similar to each other, and the difference in their response to a stimulus reflects their difference in quantal catch, dependent on their spectral sensitivity. However, the S-cone ORG bleach-response profile has not been well characterized. From the preliminary results we S-cones seem to have a lower and slower delta-OPL response per quantal catch, both factors complicating differentiation from M cones. While this precludes spectral classification when performed in isolation, it may be more advantageous coupled with the 660nm test than a re-test of the 660nm test would be for classification validation. Cones identified as S-type with 660nm test should have a response in the 420nm test. Those that do not can be labeled as lacking signal. Furthermore, the L-cone response should decrease more than the M-cone responses in the 420nm condition, which could assist in reducing error in L vs M assignment.

3) An option for increasing classification confidence that would not double the amount of time and data collected would be to combine the two experiments. The stimulus interval of the 660nm condition could be modified to have a 500ms extension where the light is switched to a 420nm stimulus, during which the L-cone delta-OPL should decrease and S-cone delta-OPL should increase.

4) Another option would be to test the putative S-cones psychophysically. The Sabesan lab can perform single-cone-targeted experiments capable of affirming a cone's short-wavelength sensitivity with a retina-fixed detection test.[18–20]

5) Finally, there are several manual steps in the cone classification process that allow for some user-error. Automating these steps and/or having multiple classifiers and inter-classifier reliability tests may slightly increase accuracy.

6.2.2 Taking S-cone topography analysis further

6.2.2.1 Clarifying the exclusion zone properties

All analyses used to assess S-exclusion zones are insensitive to, and disrupted by, anisotropic patterning. Analysis of the interior angles of Voronoi cells have been used in the past to measure anisotropic topography patterns, and could easily be applied to Concentric Ring Analysis. The downside to this approach is that S-cone sampling already tends to be low, and dividing the inter-S-cone distance information across angles will exacerbate artifact due to under-sampling.

If angle is taken into consideration, the alignment of the image and its orientation from the fovea should be double checked against an AOSLO montage. For example ROIs we collected along each meridian were not strictly along these axes. Also, when subjects sit into the AO-OCT bite-bar, there can be slight variability in the orientation of the head, so the meridional axes may not line up with the dimensions of the ROI imaged, and we did not correct for this.

6.2.2.2 Taking data-collection limitations into account

All experiments performed to assess S-cone topography used the native mosaic of the subjects tested. While this approach was advantageous for our models of random and spaced topography, it limited our ability to assess sampling limitations and how they variously influence topography metrics. To investigate this properly, I would model arbitrarily large mosaics cone mosaics with S-mosaic of known qualities (a la Chapter 4), expose them to false negatives and positives in cone finding and cone classification, and record how these perturbations influenced metric fidelity to known topography characteristics. A means to quickly check whether sampling is sufficient for a particular analysis would be very helpful for future researchers who want to quickly apply their analysis without roaming deep into the statistical woods.

6.2.3 Modeling the S-cone mosaic

The approach we've taken to model S-mosaics with known exclusion zone properties proved essential in clarifying the results measured from human subjects. These models can be very useful for testing intuitions and detecting analytic artifacts, as demonstrated in Chapter 4. Our optimized fit data provides a means for others to model S-mosaics like what we've observed. They also provide a sort of metric in of itself, with the fit inflection point and growth coefficient of the probability function used to generate them relating to the exclusion zone properties.

Consistent with the Concentric Ring Analysis being best suited of metrics tested so far to describing the S-exclusion zone, it shows promise for improving approaches to modeling pseudo-S-cone topography, too. Currently the ISETbio biophysical modeling framework[68–70] takes a strict minimum distance parameter to model the S-cone mosaic. This is suitable for many scenarios where the nuances of S-cone topography are not of concern and the oversimplified case suffices. However, applying our findings to improve accuracy of simulated S-mosaics could be valuable to computational oriented to spectral-spatial limits in short-wavelength sampling.

6.2.4 LMS topography

S-cone topography dominated my dissertation research, but the topography of L and M -mosaics are immediately available. Imminently we will have results for the CRA of the non-S mosaics, which will provide insight on whether there is any slight tendency for like-type clumping.

7: Acknowledgements

My dissertation work was supported by several funding sources and educational support programs, including:
NIH grants U01EY025501, EY027941, EY029710, P30EY001730, 5T32EY007031-42, 5T32CA206089-02
Research to Prevent Blindness Career Development Award
Burroughs Welcome Fund Careers at the Scientific Interfaces
Unrestricted grant from the Research to Prevent Blindness
DOD Air Force Office of Scientific Research
The Knights Templar Eye Foundation
UW eScience Institute Incubator Program Winter 2022
CSHL Vision: A Platform for Linking Circuits, Behavior & Perception 2023

Vimal Prabu Pandiyan performed spectral-classification experiments and performed the processing and manual steps of cone-classification. Sierra Schleufer coded and performed topography analyses, and contributed to experimental design in spectral topography experiments. Sierra developed the 2PC approach and novel simulated S-cone mosaics with Bryna Hazelton and Daniel R. Coates. Ram Sabesan provided substantial guidance throughout the process and revisions to these reports.

Additional thanks to Geoff Boynton, and Greg Horwitz for their guidance and feedback on statistical approaches. Thank you to Emily Slezak, Ben Wendel, Palash Bharadwaj, Teng Lieu, Jenna Huey, and Connor Weiss of the Sabesan lab, as well as Fred Rieke, Greg Horwitz, Sepeadeh Radpour, Kristen Drummey, and Nick Hendryxfor feedback on drafted materials. And thank you to the not-already-recognized members of my dissertation committee, Ione Fine and Mike Manookin.

Ram, thank you for making me your first grad student. I will always be grateful for the opportunities you've given me and lessons you've taught me.

To the many friends and family who supported me through this: the thank you cards might be coming the rest of your life. But not here, because I've run out of time writing this dissertation. I love you so, so much, and you know exactly who you are.

Dedicated to my Grandpa Bob

(Bob S.)

8: Citations

1. Ağaoğlu, M. N., Sheehy, C. K., Tiruveedhula, P., Roorda, A. & Chung, S. T. L. Suboptimal eye movements for seeing fine details. *J. Vis.* **18**, 8–8 (2018).

2. Anderson, A. G., Ratnam, K., Roorda, A. & Olshausen, B. A. High-acuity vision from retinal image motion. *J. Vis.* **20**, 34 (2020).

3. Bowers, N. R., Gautier, J., Lin, S. & Roorda, A. *Fixational Eye Movements Depend on Task and Target*. http://biorxiv.org/lookup/doi/10.1101/2021.04.14.439841 (2021) doi:10.1101/2021.04.14.439841.

4. Intoy, J. & Rucci, M. Finely tuned eye movements enhance visual acuity. *Nat. Commun.* **11**, (2020).

5. Rucci, M., Iovin, R., Poletti, M. & Santini, F. Miniature eye movements enhance fine spatial detail. *Nature* **447**, 852–855 (2007).

6. Conway, B. R. Spatial structure of cone inputs to color cells in alert macaque primary visual cortex (v-1). *J. Neurosci.* **21**, 2768–2783 (2001).

7. Conway, B. R. Color vision, cones, and color-coding in the cortex. *Neuroscientist* **15**, 274–290 (2009).

8. Conway, B. R. Color signals through dorsal and ventral visual pathways. *Vis. Neurosci.* **31**, 197–209 (2014).

9. De Valois, R. L., De Valois, K. K. & Mahon, L. E. Contribution of S opponent cells to color appearance. *Proc. Natl. Acad. Sci.* **97**, 512–517 (2000).

10. Kim, Y. J. *et al.* Comparative connectomics reveals noncanonical wiring for color vision in human foveal retina. *Proc. Natl. Acad. Sci.* **120**, e2300545120 (2023).

11. Marshak, D. W., Stafford, D., Jacoby, R. & Kouyama, N. Blue cone bipolar cells of the macaque retina. in *Colour Vision Deficiencies XII: Proceedings of the twelfth Symposium of the International Research Group on Colour Vision Deficiencies, held in Tübingen, Germany July 18–22, 1993* (eds. Drum, B. et al.) 277–283 (Springer Netherlands, Dordrecht, 1995). doi:10.1007/978-94-011-0507-1_33.

12. Neitz, J. & Neitz, M. Evolution of the circuitry for conscious color vision in primates. *Eye* **31**, 286–300 (2017).

13. Packer, O. S., Verweij, J., Li, P. H., Schnapf, J. L. & Dacey, D. M. Blue-Yellow Opponency in Primate S Cone Photoreceptors. **30**, 568–572 (2010).

14. Patterson, S. S. *et al.* An S-cone circuit for edge detection in the primate retina. *Sci. Rep.* **9**, 1–11 (2019).

15. Thoreson, W. B. & Dacey, D. M. Diverse Cell Types, Circuits, and Mechanisms for Color Vision in the Vertebrate Retina. *Physiol. Rev.* **99**, 1527–1573 (2019).

16. Hofer, H., Singer, B. & Williams, D. R. Different sensations from cones with the same photopigment. 444–454 (2005) doi:10.1167/5.5.5.

17. Neitz, A. *et al.* Effect of cone spectral topography on chromatic detection sensitivity. *J. Opt. Soc. Am. A* **37**, A244–A244 (2020).

18. Sabesan, R., Schmidt, B. P., Tuten, W. S. & Roorda, A. The elementary representation of spatial and color vision in the human retina. (2016).

19. Schmidt, B. P., Boehm, A. E., Foote, K. G. & Roorda, A. The spectral identity of foveal cones is preserved in hue perception. *J. Vis.* **18**, 19 (2018).

20. Schmidt, B. P., Sabesan, R., Tuten, W. S., Neitz, J. & Roorda, A. Sensations from a single M-cone depend on the activity of surrounding S-cones. *Sci. Rep.* **8**, 8561 (2018).

21. Tuten, X. W. S., Harmening, X. W. M., Sabesan, R., Roorda, X. A. & Sincich, L. C. Spatiochromatic Interactions between Individual Cone Photoreceptors in the Human Retina. **37**, 9498–9509 (2017).

22. Williams, D. R. & Macleod, J. I. A. FovealTritanopia(DavidRWilliams1981). (1981).

23. Williams, D. R., MacLeod, D. I. A. & Hayhoe, M. M. Punctate sensitivity of the blue-sensitive mechanism. *Vision Res.* **21**, 1357–1375 (1981).

24. Billock, V. A. Neural Mechanisms That Hide Individual Behavioral Differences: Evidence from Psychophysics and Neuroscience. *Comput. Brain Behav.* **3**, 102–125 (2020).

25. Yamauchi, Y. *et al.* What determines unique yellow , L / M cone ratio or visual experience ? (2002) doi:10.1117/12.464667.

26. Deeb, S. S. Genetics of variation in human color vision and the retinal cone mosaic. **28**, 301–307 (2006).

27. Neitz, J. & Neitz, M. The genetics of normal and defective color vision. *Vison Res* **23**, 1–7 (2013).

28. Hofer, H., Carroll, J., Neitz, J., Neitz, M. & Williams, D. R. Organization of the human trichromatic cone mosaic. *J. Neurosci.* **25**, 9669–9679 (2005).

29. Roorda, Metha, Lenie, Williams. Packing arangement of the three cone classes in primate retina. (2001) doi:10.1016/S0042-6989(01)00043-8.

30. Roorda, A. & Williams, D. R. The arrangement of the three cone classes in the living human eye. *Nature* **397**, 520–522 (1999).

31. Sabesan, R., Hofer, H. & Roorda, A. Characterizing the Human Cone Photoreceptor Mosaic via Dynamic Photopigment Densitometry. *PLoS ONE* **10**, (2015).

32. Stockman, A. & Sharpe, L. T. The spectral sensitivities of the middle- and long-wavelength-sensitive cones derived from measurements in observers of known genotype. *Vision Res.* **40**, 1711–1737 (2000).

33. Hunt, D. M. & Peichl, L. S cones: Evolution, retinal distribution, development, and spectral sensitivity. *Vis. Neurosci.* **31**, 115–138 (2014).

34. Peichl, L. Diversity of mammalian photoreceptor properties: Adaptations to habitat and lifestyle? *Anat. Rec. A. Discov. Mol. Cell. Evol. Biol.* **287A**, 1001–1012 (2005).

35. Curcio, C. A. *et al.* Distribution and morphology of human cone photoreceptors stained with anti-blue opsin. *J. Comp. Neurol.* **312**, 610–624 (1991).

36. Pandiyan, V. *et al.* The Optoretinogram reveals the primary steps of phototransduction in the living human eye. (2020).

37. Zhang, F., Kurokawa, K., Lassoued, A., Crowell, J. A. & Miller, D. T. Cone photoreceptor classification in the living human eye from photostimulation-induced phase dynamics. *Proc. Natl. Acad. Sci.* **116**, 7951–7956 (2019).

38. Williams, D. R. & Collier, R. Consequences of Spatial Sampling by a Human Photoreceptor Mosaic. *Science* **221**, 385–387 (1983).

39. Williams, D. R., Sekiguchi, N., Haake, W., Brainard, D. & Packer, O. The Cost of Trichromacy for Spatial Vision (from From Pigment to Perception). in (1991).

40. Martin, P. R., Grünert, U., Chan, T. L. & Bumsted, K. Spatial order in short-wavelength-sensitive cone photoreceptors: a comparative study of the primate retina. *J. Opt. Soc. Am. A* **17**, 557 (2000).

41. Pum, D., Ahnelt, P. K. & Grasl, M. Iso-orientation areas in the foveal cone mosaic. *Vis. Neurosci.* **5**, 511–523 (1990).

42. Nork, T. M., McCormick, S. A., Chao, G. M. & Odom, J. V. Distribution of carbonic anhydrase among human photoreceptors. *Invest. Ophthalmol. Vis. Sci.* **31**, 1451–1458 (1990).

43. Yellott, J. I. Spectral Consequences of Photoreceptor Sampling in the Rhesus Retina. *Science* **221**, 382–385 (1983).

44. Ahnelt, P. K., Kolb, H. & Pflug, R. Identification of a subtype of cone photoreceptor, likely to be blue sensitive, in the human retina. *J. Comp. Neurol.* **255**, 18–34 (1987).

45. Bumsted, K. & Hendrickson, A. Distribution and development of short-wavelength cones differ between Macaca monkey and human fovea. *J. Comp. Neurol.* **403**, 502–516 (1999).

46. Bumsted, K., Jasoni, C., Szél, A. & Hendrickson, A. Spatial and temporal expression of cone opsins during monkey retinal development. *J. Comp. Neurol.* **378**, 117–134 (1997).

47. Xiao, M. & Hendrickson, A. Spatial and temporal expression of short, long/medium, or both opsins in human fetal cones. *J. Comp. Neurol.* **425**, 545–559 (2000).

48. Cornish, Hendrickson, A. & Provis. Distribution of short-wavelength-sensitive cones in human fetal and postnatal retina: early development of spatial order and density profiles. (2004) doi:10.1016/j.visres.2004.03.030.

49. Hussey, K. A., Hadyniak, S. E. & Johnston, R. J. Patterning and Development of Photoreceptors in the Human Retina. *Front. Cell Dev. Biol.* **10**, (2022).

50. de Monasterio, F. M., Schein, S. J. & McCrane, E. P. Staining of blue-sensitive cones of the macaque retina by a fluorescent dye. *Science* **213**, 1278–1281 (1981).

51. Shapiro, M. B., Schein, S. J. & de Monasterio, F. M. Regularity and Structure of the Spatial Pattern of Blue Cones of Macaque Retina. *J. Am. Stat. Assoc.* **80**, 803–812 (1985).

52. Pandiyan, V. P. *et al.* Characterizing cone spectral classification by optoretinography. *Biomed. Opt. Express* **13**, 6574 (2022).

53. Ahnelt, P. K. *et al.* S–cone topography in Old World Primates: Human pattern resembles that of arboreal/forestal rather than (semi–) terrestrial species. *Invest. Ophthalmol. Vis. Sci.* **45**, 42 (2004).

54. Ahnelt, P. K., Schubert, C., Kübber-Heiss, A., Schiviz, A. & Anger, E. Independent variation of retinal S and M cone photoreceptor topographies: A survey of four families of mammals. *Vis. Neurosci.* **23**, 429–435 (2006).

55. Eldred, K. *et al.* Thyroid hormone signaling specifies cone subtypes in human retinal organoids. *Science* **362**, eaau6348 (2018).

56. Hadyniak, S. E. *et al. Temporal Regulation of Green and Red Cone Specification in Human Retinas and Retinal Organoids*. http://biorxiv.org/lookup/doi/10.1101/2021.03.30.437763 (2021) doi:10.1101/2021.03.30.437763.

57. Roberts, M. R., Hendrickson, A., McGuire, C. R. & Reh, T. A. Retinoid X Receptor γ Is Necessary to Establish the S-opsin Gradient in Cone Photoreceptors of the Developing Mouse Retina. *Invest. Ophthalmol. Vis. Sci.* **46**, 2897–2904 (2005).

58. Kouyama, N. & Marshak, D. W. The topographical relationship between two neuronal mosaics in the short wavelength-sensitive system of the primate retina. *Vis. Neurosci.* **14**, 159–167 (1997).

59. Roorda, A. & Williams, D. R. The arrangement of the three cone classes in the living human eye. *Nature* **397**, 520–522 (1999).

60. Rodieck, R. W. The density recovery profile: a method for the analysis of points in the plane applicable to retinal studies. *Vis. Neurosci.* **6**, 95–111 (1991).

61. Diggle, P. J. *Statistical Analysis of Spatial Point Patterns*. vol. Vol. 2 (Academic-Press, London, New York, 1983).

62. Cook, J. E. Spatial properties of retinal mosaics: An empirical evaluation of some existing measures. *Vis. Neurosci.* **13**, 15–30 (1996).

63. Cooper, R., Wilk, M., Tarima, S. & Carroll, J. Evaluating Descriptive Metrics of the Human Cone Mosaic. *Investig. Opthalmology Vis. Sci.* **57**, 2992 (2016).

64. Galli-Resta, L., Novelli, E., Kryger, Z., Jacobs, G. H. & Reese, B. E. curcio. *Eur. J. Neurosci.* **11**, 1461–1469 (1999).

65. Keeley, P. W., Eglen, S. J. & Reese, B. E. From random to regular: Variation in the patterning of retinal mosaics*. *J. Comp. Neurol.* **528**, 2135–2160 (2020).

66. Ester, M., Kriegel, H.-P. & Xu, X. A Density-Based Algorithm for Discovering Clusters in Large Spatial Databases with Noise. 6.

67. Peebles, P. J. E. *The Large-Scale Structure of the Universe*. *Large-Scale Structure of the Universe by Phillip James Edwin Peebles. Princeton University Press* (1980).

68. Cottaris, N. P., Jiang, H., Ding, X., Wandell, B. A. & Brainard, D. H. A computational-observer model of spatial contrast sensitivity: Effects of wave-front-based optics, cone-mosaic structure, and inference engine. *J. Vis.* **19**, 8–8 (2019).

69. Cottaris, N. P., Wandell, B. A., Rieke, F. & Brainard, D. H. A computational observer model of spatial contrast sensitivity: Effects of photocurrent encoding, fixational eye movements, and inference engine. *J. Vis.* **20**, 17 (2020).

70. Zhang, L.-Q., Cottaris, N. P. & Brainard, D. H. An Image Reconstruction Framework for Characterizing Early Vision. 43.

9: Appendix A: Classified Mosaics

Temporal Meridian

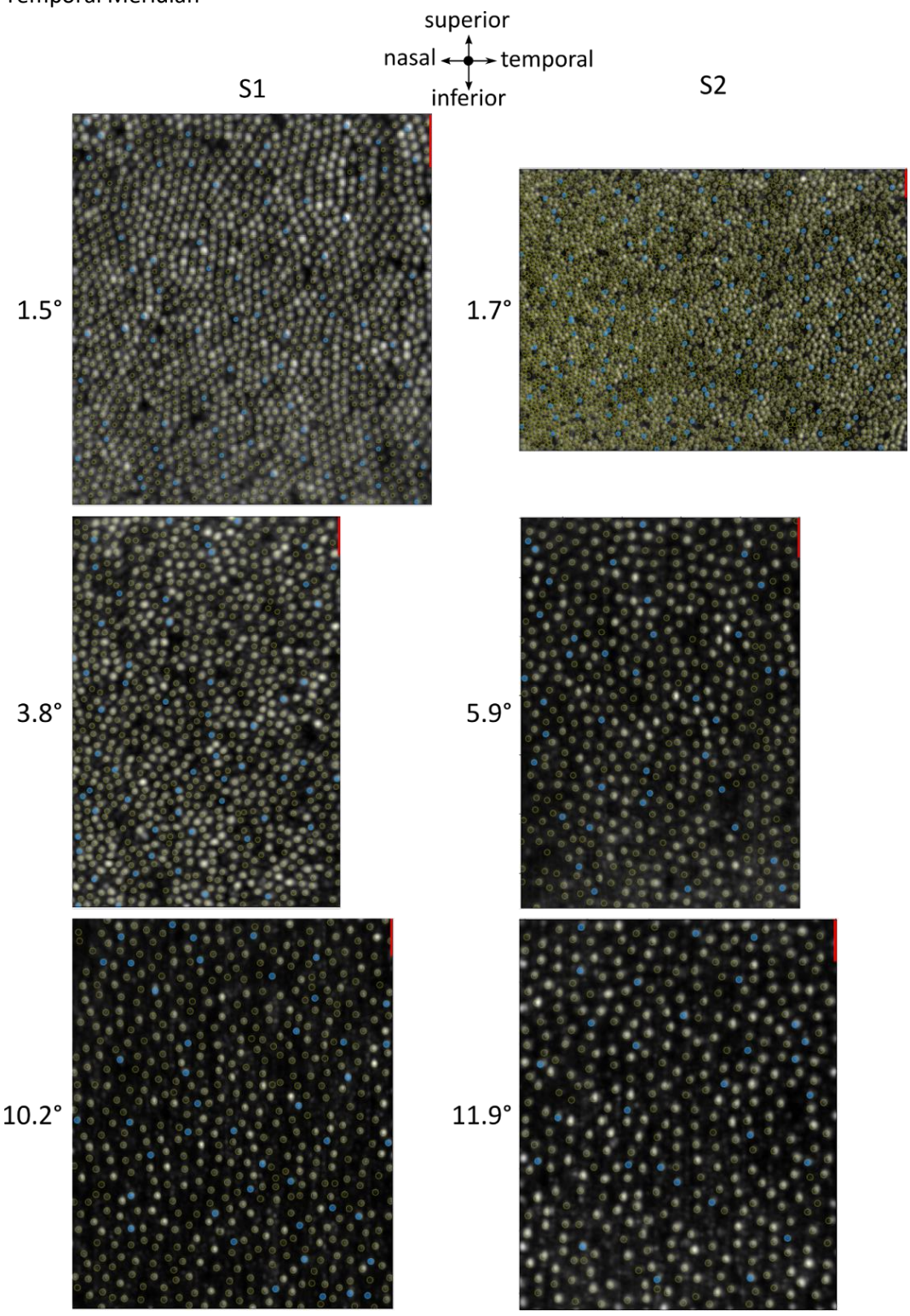

Nasal Meridian

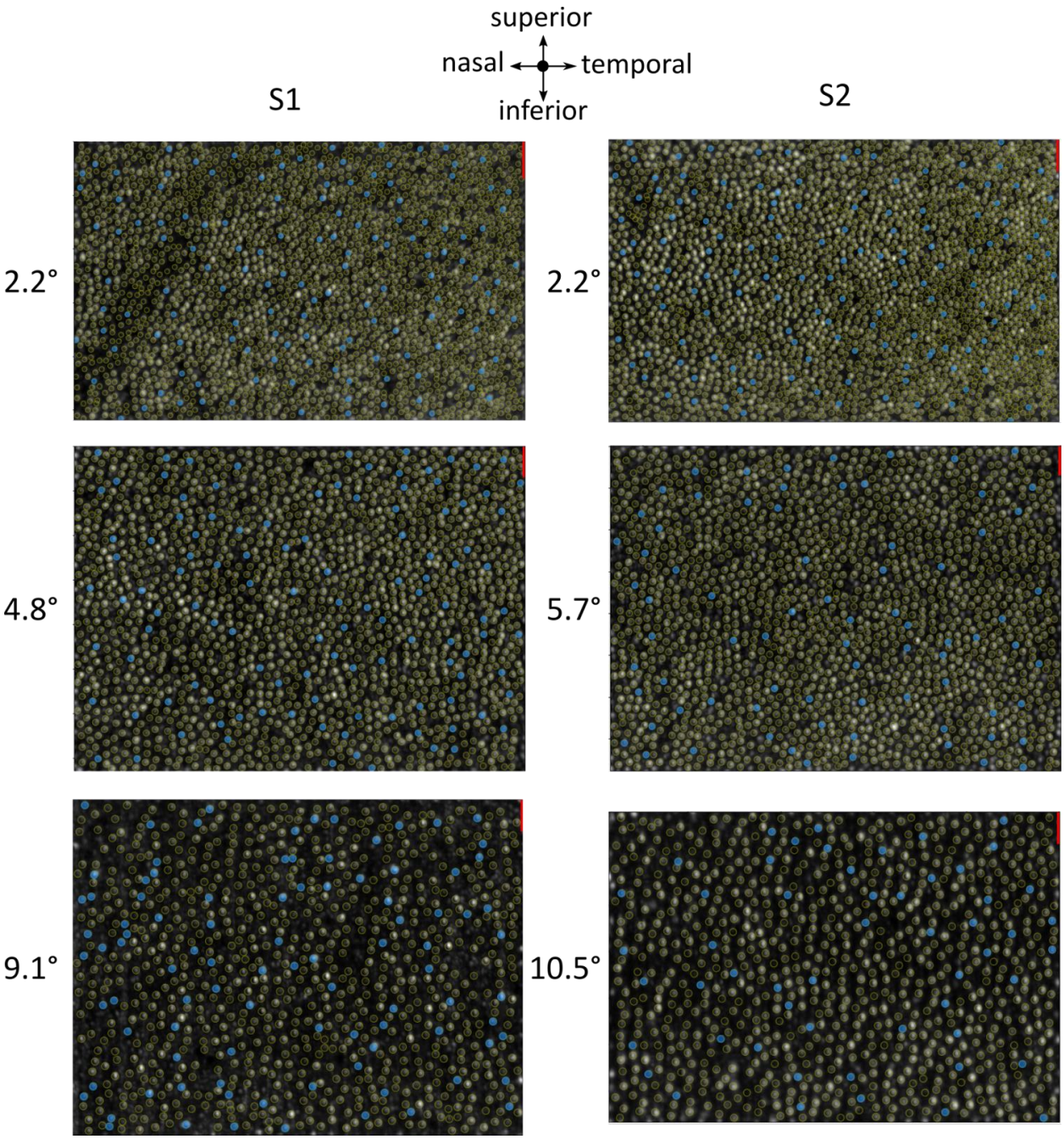

Superior Meridian

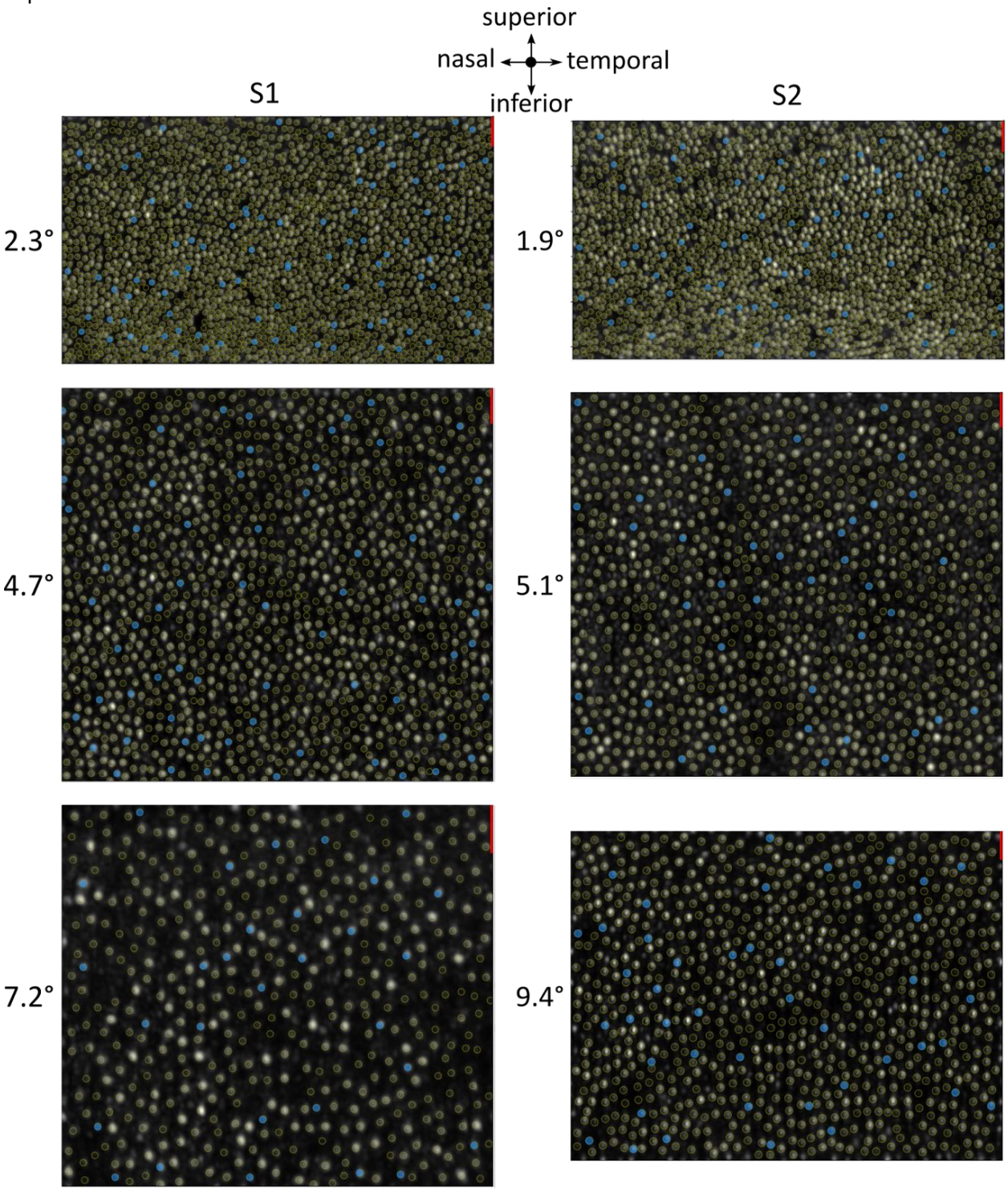

Inferior Meridian

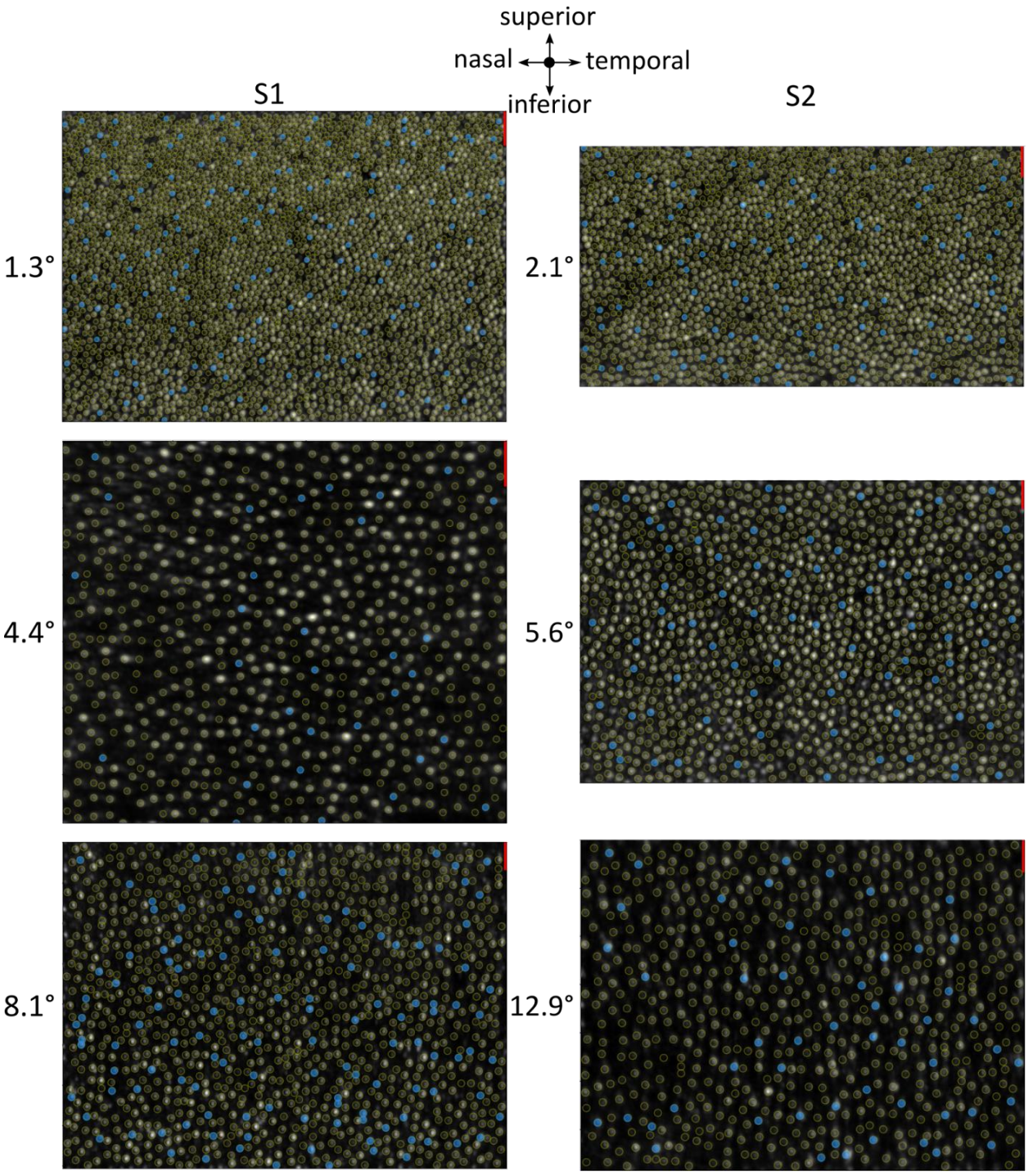

10: Appendix B: Tables

Additional Tables can be found in the published manuscript copied into Chapter 2.

Lit ROI ID	publication	subject	meridian	eccentricity (mm)	eccentricity (°)	#cones	#S cones	density S cones (per mm)	density S cones (per °)	proportion S cones
Cu 1a	Curcio 1991	1	NR	0.4	1.2	NR	38	1700	153	NR
Cu 1b	Curcio 1991	1	NR	0.4	1.2	NR	167	2224	200.16	NR
Cu 1c	Curcio 1991	1	NR	3.0	9.1	NR	184	711	63.99	NR
Co 1a	Cornish 2004a	1	NR	0.5	1.6	NR	1057	2740.9	246.681	NR
Co 1b	Cornish 2004a	1	NR	1.6	5.4	NR	428	1109.8	99.882	NR
Ma 1*	Martin 2000	macaque	NR	2.2	6.7	NR	333	1119	100.71	NR
Ro JWN	Roorda 2001	JW	nasal	0.3	1.0	650	30	NR	NR	4.6
Ro JWT	Roorda 2001	JW	temporal	0.3	1.0	811	31	NR	NR	3.8
Ro ANN	Roorda 2001	AN	nasal	0.3	1.0	522	27	NR	NR	5.2
Ro M5T*	Roorda 2001	M5	temporal	0.4	1.4	904	78	NR	NR	8.6
Ro M3N*	Roorda 2001	M3	nasal	0.3	1.0	507	39	NR	NR	7.7
Ro M6N*	Roorda 2001	M6	nasal	0.3	1.0	625	41	NR	NR	6.6
Ro M7N*	Roorda 2001	M7	nasal	0.3	1.0	583	37	NR	NR	6.3
Ho HS	Hofer 2005	HS	nasal	0.3	1.0	375	24	NR	NR	6.4

Ho YY	Hofer 2005	YY	nasal-superior	0.3	1.0	1000	64	NR	NR	6.4
Ho AP	Hofer 2005	AP	nasal	0.4	1.3	1003	56.168	NR	NR	5.6
Ho AP	Hofer 2005	AP	temporal	0.3	1.0	1000	66	NR	NR	6.6
Ho MD	Hofer 2005	MD	nasal	0.4	1.3	897	52.026	NR	NR	5.8
Ho JP	Hofer 2005	JP	temporal	0.3	1.0	812	38.164	NR	NR	4.7
Ho JC	Hofer 2005	JC	temporal	0.4	1.3	645	35.475	NR	NR	5.5
Ho RS	Hofer 2005	RS	nasal	0.4	1.3	897	41.262	NR	NR	4.6
Ho BS	Hofer 2005	BS	nasal	0.375	1.25	734	40.37	NR	NR	5.5

Table 1.1 S-mosaics assessed for the presence of an S-exclusion zone. All human cases where the presence of and human S-exclusion zone is investigated with spatial point processes, and select macaque data (noted with asterisks), are detailed. NR = Not Recorded.

Lit ROI ID	ER (μm)	ER (arcmin)	PF	Bin width (μm)	Bin width (arc-min)
Cu 1b	9.5	1.71	0.18	2	0.4
Cu 1c	20.8	3.744	0.27	4	0.8
Ma 1*	18.7	3.74	0.34	5	1
Ro JWN	0	0	n/a	15	3
Ro JWT	0	0	n/a	15	3
Ro ANN	0	0	n/a	15	3
Ro M5T*	0.9	3	NR	15	3
Ro M3N*	0.9	3	NR	15	3
Ro M6N*	0.9	3	NR	15	3
Co 1a	8.9	1.602	0.19	1.8	0.36

Co 1b	12.3	2.214	0.15	8	1.6

Table 1.2 S-exclusion zone radii measured with DRP analysis. All human cases where an S-exclusion zone was detected and its radius was reported, and select macaque data (noted with asterisks), are detailed. NR = Not Recorded.

ROI #	ROI ID	% S-cones	S-cone density	Cone density	μINDa	eMR	# S-cones	# cones
1	S1 1.5° T	5.44	220.38	4098.68	1.03	4.37	80	1470
2	S1 3.8° T	6.61	107.38	1669.92	1.63	6.18	59	892
3	S1 10.18° T	8.03	66.09	785.52	2.38	8.08	44	548
4	S1 2.2° N	5.94	196.4	3229.37	1.16	4.7	138	2323
5	S1 4.8° N	6.95	97.4	1354.43	1.81	6.71	115	1655
6	S1 9.1° N	10.89	79.74	743.72	2.46	7.31	95	872
7	S1 2.3° S	4.94	110.37	2047.05	1.46	6.45	97	1965
8	S1 4.7° S	5.68	54.71	1125.25	1.98	8.15	69	1215
9	S1 7.2° S	6.71	64.52	867.96	2.27	8.46	30	447
10	S1 1.3° I	5.27	189.06	3523.05	1.11	4.77	171	3246
11	S1 4.4° I	4.88	62.79	1024.32	2.07	9.06	32	656
12	S1 8.1° I	11.36	93.26	769.35	2.4	6.99	126	1109
13	S2 1.7° T	4.71	166.18	3292.6	1.16	5.22	167	3545
14	S2 5.93° T	7.02	75.54	1040.75	2.06	7.54	38	541
15	S2 11.94° T	7.73	58.57	716.22	2.49	8.67	29	375
16	S2 2.2° N	5.67	161.19	2667.27	1.28	5.27	144	2538
17	S2 5.7° N	4.66	52.14	1211.69	1.91	8.79	77	1653
18	S2 10.5° N	6.49	51.98	788.11	2.39	9.12	54	832
19	S2 1.9° S	4.09	105.34	2186.51	1.42	6.88	74	1809

20	S2 5.1° S	4.38	42.19	876.13	2.24	10.43	41	937
21	S2 9.4° S	5.61	33.69	586.9	2.75	11.39	44	785
22	S2 2.1° I	5.21	124.23	2380.51	1.36	5.83	109	2092
23	S2 5.6° I	7.04	66.53	917.8	2.19	8.14	80	1137
24	S2 12.9° I	8.66	62.44	623.57	2.66	8.91	55	635

Table 3.1 Basic topography metrics. Metadata and simple topography metrics calculated for the 24 spectrally classified ROIs assessed in this study.

11: Appendix C: Cone topography analysis in subjects with inherited retinal disease

C.1 Preamble

DRP analysis was applied to assess the explore spatial characteristics of low-functioning cells in early stages of retinal degeneration due to a variety of inherited retinal diseases. We chose DRP in this instance because it is not sensitive to missing cones, which increases with disease progression as the photoreceptor mosaic integrity deteriorates. 2PC would have been appropriate, too, but was left out because the method hasn't yet been published.

Relevant excerpts are provided below from the manuscript accepted for publication by IOVS March 2024.

Journal: Investigative Ophthalmology & Visual Science (IOVS)

MS #: IOVS-24-40053

Article title: Cone dysfunction precedes deficits in visual sensitivity and cone density in Retinitis Pigmentosa

Authors: Benjamin Wendel, Vimal Pandiyan, Teng Liu, Xiaoyun Jiang, Ayoub Lassoued, Emily Slezak, Sierra Schleufer, Palash Bharadwaj, William Tuten, Debarshi Mustafi, Jennifer Chao, and Ramkumar Sabesan

C.2 Relevant excerpts of manuscript

C.2.1 Introduction (complete)

Retinitis pigmentosa (RP) refers to a group of clinically similar phenotypes with genetically heterogeneous causes. The discovery of the first causative gene in 1990[1] and subsequent discovery of over 80 causative genes for RP[2] have provided further insight into pathophysiology of disease. RP is broadly characterized by a gradual loss of rods resulting in night-vision impairment and progressive peripheral visual field loss followed by secondary cone degeneration, which leads to severe visual impairment and central vision loss. The clinical diagnosis of RP currently relies on structural and

functional measures of retinal integrity, including clinical ophthalmoscopy, optical coherence tomography (OCT), visual perimetry, and electroretinography (ERG). One of the central findings in RP is disruption to the reflective bands on OCT emanating from the photoreceptors. As visualized by OCT, the disease transition zone (TZ) is the region of active photoreceptor degradation that separates a "central island" of relatively healthy appearing retina from the more severely diseased peripheral retina. While the principal biomarkers of RP in the clinic signal broader regional changes in the retina, we still lack a detailed understanding of disease status and photoreceptor function at a cellular level.

The use of adaptive optics (AO) has enabled us to probe the structural features at the cellular level in RP patients and those afflicted with other retinal diseases[3]. AO-scanning laser ophthalmoscopy (AOSLO) images of RP subjects have shown a variety of structural phenotypes depending on disease severity, ranging from normal-appearing cone mosaic in the central macula, cones with abnormal waveguiding in the TZ that appear dysflective[4-6], to severely disrupted mosaics that extend beyond the TZ. For the cone mosaic that remains intact, it has been established that cone density decreases, and cell diameter increases in the TZ of RP subjects[4]. Moreover, even when cone density is reduced by up to 62% below normal controls near the fovea, visual acuity and sensitivity detected by current clinical measures remained within normal limits[7]. Thus, despite the advances in our ability to discern cones at a structural level, we lack readily available tools with the sensitivity and resolution to assess cone function at a cellular scale in humans.

Cellular scale measures of cone dysfunction in RP have been limited in comparison to the AO based structural metrics. AO-microperimetry (AOMP) corrects for eye movements in real time by actively tracking the retinal image, enabling the delivery of visual stimuli to specific cellular targets, and thereby overcoming the limited spatial specificity of conventional microperimetry[8]. In RP, for example, the use of AOMP has shown that there is a decrease in visual sensitivity in patients with mutations in the RPGR gene, but not in those with patients with a RHO mutation. Clearly, the specific mutation in RP affects the mechanisms by which disease manifests in cone structure and function[9].

While all perimetric techniques, including AOMP, depend on subjective feedback, the gold standard for objective functional assessment is ERG. Though a full field ERG is a widely used functional test for the diagnosis of RP, its use is restrictive in monitoring disease progression because of the lack of spatial resolution. Even multifocal ERGs (mfERG) have relatively coarse spatial resolution compared to other functional assays such as macular visual field sensitivity and microperimetry[10]. ERGs measure the

composite response of large numbers of cones (~1.5° of retina in mfERG, e.g.) and are not measurable in advanced stages of disease. ERGs lack the sensitivity to identify local variation in retinal response, let alone probe retinal function at the level of individual cells. Moreover, ERG is an invasive process that requires subject cooperation with electrode placement and can be challenging in the pediatric population.

There is a need for non-invasive retinal imaging that would provide cellular scale resolution to assess the structural and functional state of the retina. Recent advances in the use of AO-OCT to generate optoretinograms (ORGs) have made it possible to quantify light-evoked responses in the retina in an objective manner, and at the level of single cells with exquisite spatiotemporal resolution[11-16]. This can lead to a sensitive and comprehensive assay of cone viability in RP. The technology is still relatively nascent in its application to retinal diseases and has shown promising early results. Lassoued *et al*[17] reported ORG responses were reduced in RP, even in areas of apparently normal cone mosaics, indicating that ORGs can detect dysfunction that may remain undetectable with other measures. To what extent deficits observed in ORG are correlated with extant measures of cellular structure and function remains uncharacterized. Our objective was to combine the cellular-scale imaging tools of AOSLO, AOMP, and ORG in the same individual RP subjects, and to evaluate the degree of correlation and covariance in these biomarkers. Correlating the measures enables the assessment of the sensitivity of these different metrics to disease and addresses the inherent sources of limitations within each. In combination, these biomarkers that are all acquired via safe and non-invasive tools will enable creation of a disease severity score that can be used for assessing disease progression and the efficacy of new targeted therapies in the future.

C.2.2 Methods

To determine whether cells with low ΔOPL were distributed randomly within an ROI, we employed Density Recovery Profile (DRP)[22] and Monte Carlo simulations as previously described to measure structure in S-cone sub-mosaics[23]. The DRP measures the average density of a sub-mosaic of interest as a function of distance from the points within that sub-mosaic and plots the result as a histogram. Monte Carlo simulations are mosaics with the same overall cone positions as the sub-mosaic population, but randomly distributed. By comparing the measured DRP to the statistics of Monte Carlo DRPs, bin-by-bin in a histogram, it is possible to determine whether the measured distribution is significantly different from random. At close distances, a significantly low density of the DRP indicates that the cones in the sub-mosaic are spaced apart, whereas a significantly high value indicates clumping. We generated 100

Monte Carlo simulated variants for every ROI to assess differences from a random arrangement. DRPs were computed with a bin width equal to the average nearest-neighbor distance of the local cone mosaic, such that the bins reflect average density of cones approximately 'x' number of cones away from one another. This enables capturing the degree of structure in the sub-mosaic as it varies between individuals and eccentricity, unlike the case where bin widths are expressed in units of angular distance. A z-score >= .95 at any bin was used to gauge whether the measured DRP was significantly different from random.

C.2.3 Results

Spatial analysis of low ΔOPL cones

To assess whether cones with degraded ORGs are arranged randomly in the mosaic or tend to neighbor one another, we calculated DRP statistics (see *methods*) on low ΔOPL cones in each RP mosaic. In RP025, RP039, and RP040, the spatial distribution of low ΔOPL cones was not significantly different from random as assessed by comparing their DRP to Monte Carlo simulations, suggesting that low ΔOPL cones did not tend to cluster in the mosaic. However, ROIs at 1° and 2° in RP062 were significantly different (p<0.05) from random, indicating a higher likelihood for cells with degraded ORG to be clumped within 1 or 2 cones of each other at 1° and within a 1-cone radius at 2° (Fig. 9). In comparison, normal controls exhibited a semi-regular arrangement of the low ΔOPL cones, i.e. S-cones, where they were unlikely to be situated within a radius twice the average distance between cones in that mosaic.

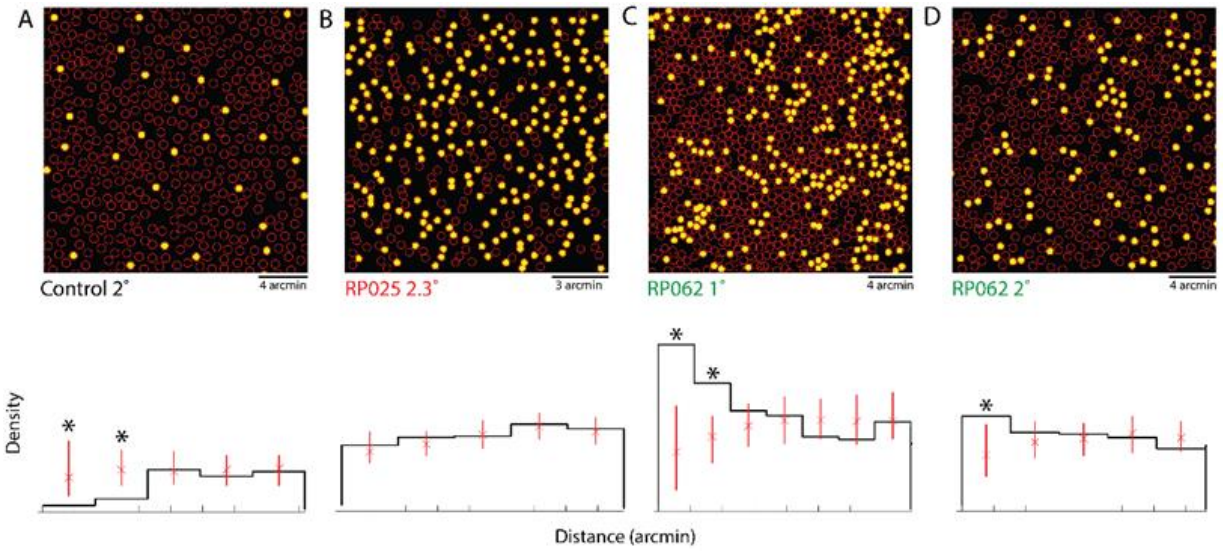

Figure C.1 (Figure 9 of Wendel et al 2024). Spatial analysis of cones with reduced ΔOPL shows spatial clustering in RP062. Top row: RP cone mosaics showing spatial distribution of low ΔOPL cells (yellow). Left to right, low ΔOPL cells n=31/435 <338nm; n=222/400 <338nm; n=255/930 <348nm; n=122/589 <338nm. Bottom row: histogram for each mosaic compared to 100 randomly shuffled Monte Carlo simulations (error bars = 95% confidence interval) to test whether low ΔOPL (yellow) cells are distributed randomly in the mosaic. Bin width set as the average inter-cone spacing for all cones in each mosaic (for A=1.8, B=1.8, C=1.2, and D=1.6 arcmin). (*) indicates bins that are either significantly lower (A) or higher (C, D) than the 95% confidence interval of the randomly shuffled mosaic. Results of the simulation indicate that low ΔOPL cells in RP062, shown in panels C) and D), exhibit have significant clustering but RP025's are not distinguishable from random (B). Control mosaic low ΔOPL cones in A) are arranged in a semi-crystalline manner, i.e. significantly spaced apart, consistent with the expected S-cone sub-mosaic.

C.2.4 Discussion

RP062 (SNRNP200) presents a distinct phenotype compared to the other RP subjects. The ORG responses for RP062 were distributed in 3 discrete clusters of ΔOPL, and cones with a reduced response were more likely than random to be spatially adjacent. However, deficits in visual sensitivity were found in retinal regions with normal cone density at 1º and 2° eccentricity. SNRNP200 mutations belong to a class of non-syndromic autosomal dominant RP (adRP) cases that are caused by ubiquitously expressed splice factors, which only affect the retina. SNRNP200 encodes the hBrr2 protein, a critical component of the tri-snRNP complex that is required for proofreading of pre-mRNA transcripts[37]. It remains unknown why SNRNP200 pathogenicity is specific to the retina, but it has been proposed that either the mutation could cause impaired fidelity of retinal gene expression that leads to an accumulation of transcript errors that are toxic to the retina, or that the retina is more susceptible to defects in pre-mRNA splicing because of the metabolic demands of the continual renewal of the photoreceptor outer segment, and/or that SNRNP200 may serve additional functions in the retina that have yet to be described[38]. In the case of RP062, it is possible that the spatial clustering of discrete populations of dysfunctional cones could be driven by factors in the microenvironment that pre-dispose sensitivity to the mutation, such as susceptibility to splicing errors and/or metabolic stress.